Mathematical approaches to the study of cellular heterogeneity, treatment design, and immune response in cancer

by

Moriah Jane Pellowe

A thesis presented to the University of Waterloo
in fulfillment of the thesis requirement for the degree of
Doctor of Philosophy
in
Applied Mathematics

Waterloo, Ontario, Canada, 2020

Examining Committee Membership

The following served on the Examining Committee for this thesis. The decision of the Examining Committee is by majority vote.

External Examiner: Katrin Rohlf
Professor, Dept. of Mathematics, Ryerson University

Supervisor(s): Mohammad Kohandel
Associate Professor, Dept. of Applied Math, University of Waterloo

Internal Member(s): Sivabal Sivaloganathan
Professor, Dept. of Applied Math, University of Waterloo

Brian Ingalls
Associate Professor, Dept. of Applied Math, University of Waterloo

Internal-External Member: Andrea Edginton
Associate Professor, School of Pharmacy, University of Waterloo

This thesis consists of material all of which I authored or co-authored: see Statement of Contributions included in the thesis. This is a true copy of the thesis, including any required final revisions, as accepted by my examiners.

I understand that my thesis may be made electronically available to the public.

Statement of Contributions

Chapter 1: I am the sole author.

Chapter 2: I completed all the model development and mathematical analysis for this project. Dr. Ting Luo and Dr. Homeyra Pourmohammadali were the lab technicians from the Mathematical Medicine Laboratory who collaborated on this project. Dr. Ting Luo completed the *in vitro* experiments, and they both assisted in writing the descriptions of the biological experiments.

Chapter 3: I completed all the model development and mathematical analysis for this project. Dr. Ting Luo and Dr. Homeyra Pourmohammadali were the lab technicians from the Mathematical Medicine Laboratory who collaborated on this project. Dr. Ting Luo completed the *in vitro* experiments, and Dr. Homeyra Pourmohammadali assisted in organizing the *in vitro* results for analysis and in writing the descriptions of the biological experiments.

Chapter 4: I completed all the model development and mathematical analysis for this project. Our collaborators, Dr. Aaron Goldman and his team, provided the *in vitro* protein expression data used in fitting the mathematical models.

Chapter 5: This project was done in collaboration with Dr. Michelle Przedborski and Dr. Aaron Goldman and his team. I completed the research on the biological background involved in constructing the model. Dr. Michelle Przedborski and I jointly wrote the code for parameter estimation. I wrote the code for the local sensitivity analysis, and they wrote the code for the global sensitivity analysis. The discussion of the results was done by me in this thesis. Dr. Aaron Goldman and his team provided the *ex vivo* data (cytokine assays and flow cytometry) used in fitting the model.

Chapter 6: I am the sole author.

Abstract

One of the complicating factors in treating cancer patients is the different levels of heterogeneity involved. In this thesis, we use a combination of mathematical methods (*in silico* experiments) and experimental data (*in vitro* and *ex vivo* experiments) to study cellular heterogeneity, treatment design, and immune response in cancer. This thesis demonstrates the importance and value of interdisciplinary communication and collaboration.

In Chapter 2, we develop a framework that uses *in vitro* and *in silico* experiments to characterize cancer cell lines and investigate the cellular dynamics during early cancer development for specific cancer cell lines. We demonstrate this process with the breast cancer cell line, MCF-7, and present evidence that progenitor cells are the significant cancer subpopulation during early cancer development for MCF-7 cells. In Chapter 3, we modify and build on the agent-based model of Chapter 2 to characterize the effect of pressure on mammosphere formation with and without the presence of a chemotherapy drug. Our results suggest that pressure induces phenotypic plasticity.

In Chapter 4, we identify the Hsp90 protein network as a means by which drug resistance can be overcome in a DTC. We construct a minimal *in silico* model of this network to design a treatment schedule for docetaxel and radicicol. *In silico* experiments are used to show that radicicol can overcome the development of drug resistance to docetaxel with the proper treatment sequence, which can be accomplished with a nanoparticle formulation. We present evidence that the intake rate and the decay rate of radicicol are drug formulation properties that will have the greatest impact on increasing the efficacy of the docetaxel-radicicol treatment sequence.

In Chapter 5, we investigate the variability in immune system response to anti-PD-1 immunotherapy. In this work, we construct a systems biology model and use sensitivity analysis to identify potential biomarkers for a positive response to anti-PD-1 immunotherapy. We present evidence of the importance of two interaction networks with regards to response to anti-PD-1 immunotherapy: 1) the interaction between cancer cells and $CD8^+$ cytotoxic Tc cells, and 2) the balance between $CD4^+$ Th1 and Th2 helper cells.

In each of the chapters, we investigate heterogeneity at a different level: cellular heterogeneity with and without the cell microenvironment, variability in protein expression, and variability in immune system response. By developing an *in silico* model to describe the biological phenomena, we can investigate the underlying mechanisms at work and provide potential biomarkers and potential improvements that can be tested further.

Acknowledgements

I would like to thank my supervisor, Dr. Mohammad Kohandel, for his teaching and guidance throughout my studies. I would like to thank my committee members Dr. Sivabal Sivaloganathan, Dr. Brian Ingalls, Dr. Andrea Edginton, and Dr. Katrin Rohlf for serving on my committee and for their comments and suggestions.

I would like to thank my collaborators Dr. Aaron Goldman and his team, Dr. Ting Luo, Dr. Homeyra Pourmohammadali, and Dr. Michelle Przedborski for the privilege of working alongside them on various projects. I would like to thank the NSERC for providing funding during my graduate studies. I would like to thank current and past members of the Biomedical Research Group, especially my office mate, Dr. Farinaz Forouzannia, for their encouragement and for interesting scientific discussions, and Dr. Michelle Przedboski, who provided very helpful comments when I was preparing this thesis.

I would like to thank my family (immediate and extended) for their encouragement throughout my studies. Your words of encouragement and practical acts of service lifted my spirits when things were hard. I would like to especially thank my husband, Harley. You are an abounding source of encouragement, support, and joy.

Finally, I want to thank God for bringing me places I never thought possible and for the future that He has in store for me. You work all things out for good in my life (Rom 8:28) and so regardless of any challenge or obstacle, it is well with my soul (Ps 46).

Dedication

This is dedicated to God, who made all of this possible, and to Harley, my best friend, with whom I have the honour and joy of doing life.

Table of Contents

List of Tables

List of Figures

Chapter 1

Background

1.1 Introduction

In this chapter, we cover the biological background and the mathematical background for the following chapters. We first discuss the complexity of cancer and the need for individualized treatment. We then discuss the different levels of heterogeneity involved in cancer. In particular, we discuss two frameworks of cellular heterogeneity: clonal evolution and cancer stem cells. Cancer stem cells have been identified in several different types of cancer, and they play an important role in tumour growth.

In addition to the complex interactions within a tumour, cancer cells interact with and respond to the tumour microenvironment. We discuss cancer stem cell niches, which are locations within a tumour that promote the cancer stem cell phenotype. We then discuss the role that cancer stem cells play in creating their own favourable microenvironment. Finally, we discuss interstitial fluid pressure as a microenvironmental stressor for cancer cells.

In the mathematical background section, we discuss the rationale for using mathematical methods in studying cancer heterogeneity and present the different types of models that we consider in this thesis: the hierarchy model for the cancer stem cell hypothesis, the two-compartment model for the cancer stem cell hypothesis, agent-based models for a spatial framework, and systems biology models for protein and signalling networks. We also discuss two methods that we apply throughout subsequent chapters: parameter estimation and sensitivity analysis. Finally, we conclude with a thesis outline.

1.2 Biological background

1.2.1 Cancer

Normal tissues have regulatory mechanisms that maintain homeostasis. In other words, the body has various ways of checking and ensuring that cells are behaving in a way that is beneficial for the entire cell population. For example, both growth factors (e.g. EGF [1,2]) and growth suppressors (e.g. RB and TP53 proteins [3]) are regulated to ensure that cells are dividing in a controlled manner so that the number of cells in a tissue is maintained. If a cell exhibits abnormal behaviour due to irreparable cell damage, either extracellular signals (e.g. Fas ligand [3]) or intracellular signals (e.g. proapoptotic triggering proteins Bax and Bak [3]) are sent to activate apoptosis to keep the tissue healthy [3].

In normal tissue function, DNA mutations can occur during cell division, specifically during DNA replication. A mutation may result in a competitive advantage, a competitive disadvantage, or it may not affect the cell's fitness at all. Cancer arises when a cell has acquired a series of advantageous mutations that allow the cell(s) to overcome and/or avoid the tissue's regulatory mechanisms as well as dominate in the local tissue environment [3].

Cancer includes a variety of diseases that share certain key characteristics, known as the hallmarks of cancer. These characteristics include (1) evading growth suppressors, (2) avoiding immune destruction, (3) enabling replicative immortality, (4) tumour-promoting inflammation, (5) activating invasion and metastasis, (6) inducing angiogenesis, (7) genome instability and mutation, (8) resisting cell death, (9) deregulating cellular energetics, and (10) sustaining proliferative signaling as seen in Figure 1.1 [3].

When treating cancer, clinicians use a variety of different therapies including surgery, chemotherapy, radiotherapy, and immunotherapy [4, 5]. Although clinicians have different strategies at their disposal, treatment design can become complex due to the unique condition of each patient as well as the complexity of the disease. Cancer involves many different factors and pathways, which are intricately connected in a complex network of cells, proteins, enzymes, etc. Each of the previously mentioned hallmarks of cancer (as shown in Figure 1.1) is regulated by redundant signaling pathways, which all need to be targeted in order to shut down a given aspect of cancer cell functionality. Otherwise, the selective pressure of targeting a single pathway may result in the adaptation of the cancerous cells. Cancer cells may also adapt so that they depend less on a given hallmark of cancer and more on another, adjusting to the microenvironment or to the administered

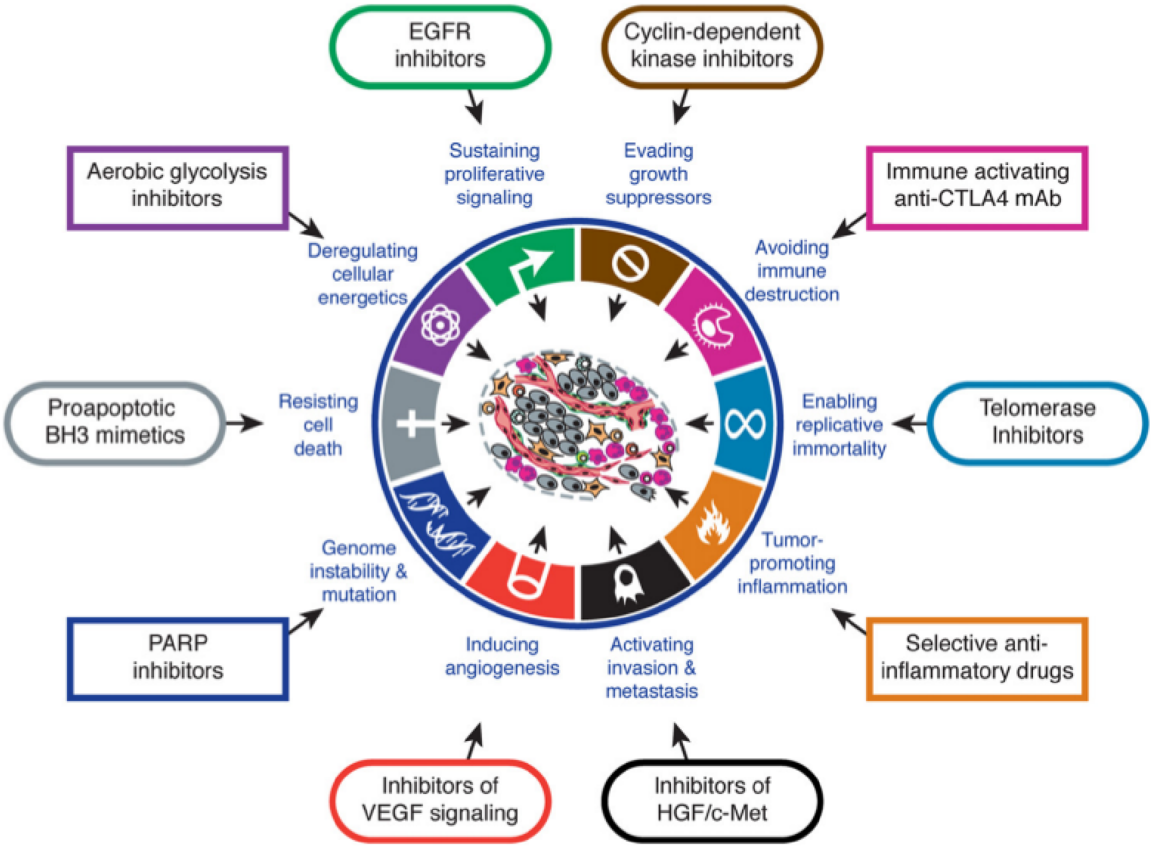

Figure 1.1: Hallmarks of cancer, Figure 6 taken from Hanahan & Weinberg [3]. Shown are the hallmarks of cancer as well as examples of therapies that target those specific hallmarks.

treatment. Thus, an effective cancer treatment strategy should target various (if not all) of the different aspects of cancerous behaviour [3].

1.2.2 Heterogeneity in Cancer

In general, cancer treatment should be individualized since there are several levels of heterogeneity to consider: cancer types are unique enough that they should be treated as different diseases; each patient responds differently to treatment [3]; and every tumour responds to treatment differently due to its unique makeup of cells and its unique microenvironment. At the level of cells, there are different cell phenotypes which may be due to genetic or epigenetic differences. Each phenotype has its own set of characteristics with respect to cell behaviour, such as proliferation and death rate, and may react differently to a given microenvironment (e.g. acidity [6], hypoxia [7], etc.) [8]. Different phenotypes within a cell population can play different roles to ensure population growth. Ideally, all levels of heterogeneity should be considered when designing a model of tumour growth and its response to treatment.

Inter-patient variability in immune system response

There is considerable inter-patient variability in response to treatment due to a multitude of factors such as age, gender, body weight, health, etc. [9]. In Chapter 5, we explore inter-patient variability in the immune system's response to nivolumab, an anti-PD-1 antibody used as immunotherapy. The variability is due to the complex interaction between the immune system and cancer cells as cancer cells attempt to avoid immune destruction. Cancer cells have been shown to secrete immunosuppressive factors, such as TGF-β, and can recruit immunosuppressive cells, e.g. regulatory T cells [3]. Immune escape is also accomplished through decreased antigen presentation, as observed in cancer patients [10]. Decreased antigen presentation results in less activation of antigen-presenting cells, such as dendritic cells, which leads to less activation of cytotoxic T cells, which are responsible for cell-mediated immunity [11]. Overall, these interactions need to be considered in analyzing the immune response of cancer patients to nivolumab.

Cellular heterogeneity

In this section, we present two prominent theories to explain tumour heterogeneity: clonal evolution [12] and the cancer stem cell hypothesis [13]. In the traditional view of cancer, known as clonal evolution, tumour heterogeneity is the result of genetic heterogeneity within the tumour as shown in Figure 1.2. Cancer is initiated by an advantageous genetic mutation. As the cancerous cell divides and a mass begins to form, additional advantageous mutations allow the cancerous cells to become increasingly abnormal and to develop additional growth advantages over normal cells [12]. The incidence of mutations can also be increased by genomic instability [3]. The large variety of genes allows the tumour to adapt quickly to the microenvironment to ensure continued survival and proliferation. In this theory, mutations and natural selection are the driving forces behind tumour heterogeneity and tumour growth [8].

A more recent view of tumour heterogeneity is known as the cancer stem cell hypothesis as shown in Figure 1.3, which assumes that cancer cells are hierarchically organized. At the top of the hierarchy, cancer stem cells exclusively have tumourigenic potential [13]. Since cancer stem cells play an important role in tumour initiation, there may be a larger proportion of them during tumour initiation. In later stages of tumour development, the fraction of cancer stem cells may decrease since less cancer stem cells are needed [14]. In the cancer stem cell hypothesis, tumour heterogeneity is the result of the differentiation of cancer stem cells [13].

Cancer stem cells

In normal tissue, stem cells are unique in that they have the ability to differentiate into different kinds of cells [13]. They are at the top of a differentiation hierarchy where a cell's progeny is more differentiated than its parent cell. The cells become more differentiated through division until they are highly specialized. Unlike differentiated cells, stem cells are immortal, i.e. they can divide an infinite (or very large) number of times, and they exhibit self-renewal, i.e. they can divide symmetrically or asymmetrically to retain their stem cell phenotype [15].

Cancer stem cells can be the result of cancerous transformation of normal stem cells or of progenitor cells that have acquired self-renewing properties [15]. In general, they retain many of the traits of ordinary stem cells. For example, cancer stem cells initiate a hierarchy of cancer cells [13]. These cells also have infinite (or very large) proliferative potential due

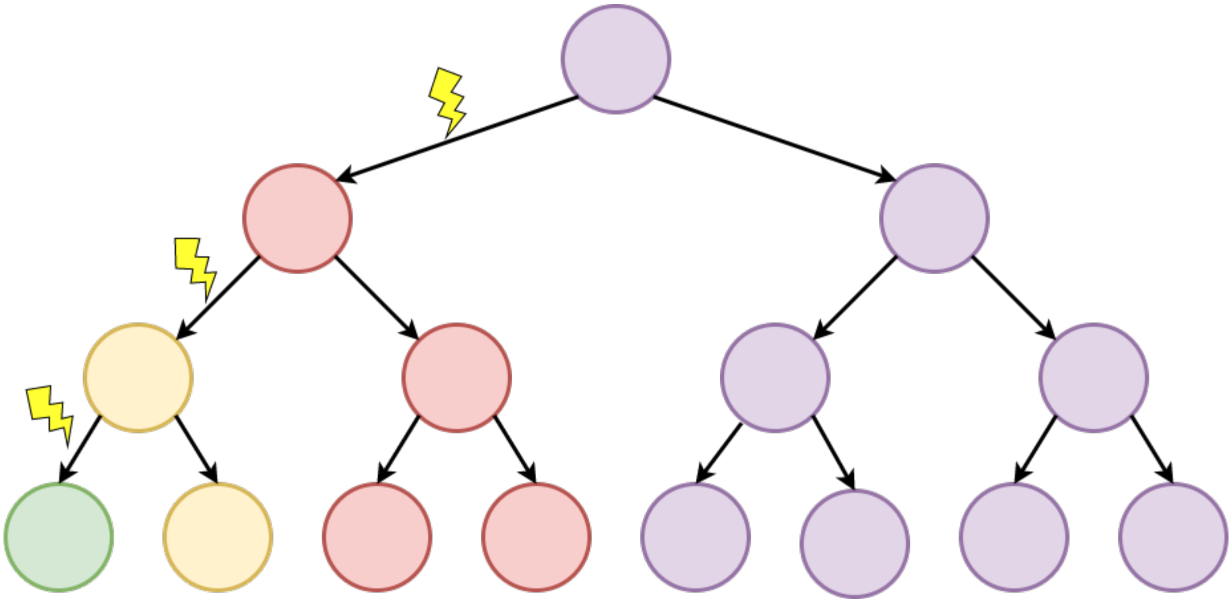

Figure 1.2: Clonal evolution. According to clonal evolution [12], a cancer clone can divide and spontaneously acquire mutations that result in different subclones. These resulting subclones may have mutations that are advantageous, disadvantageous, or neutral. The figure above demonstrates how a cancer cell divides and may undergo mutations that result in new cancer cell lines (shown as different colours). Some of these subclones will eventually die out while others will persist and continue to acquire additional mutations. As genetic instability increases in these subclones, mutations become a more common occurrence, resulting in increased clonal diversity in the resulting tumour.

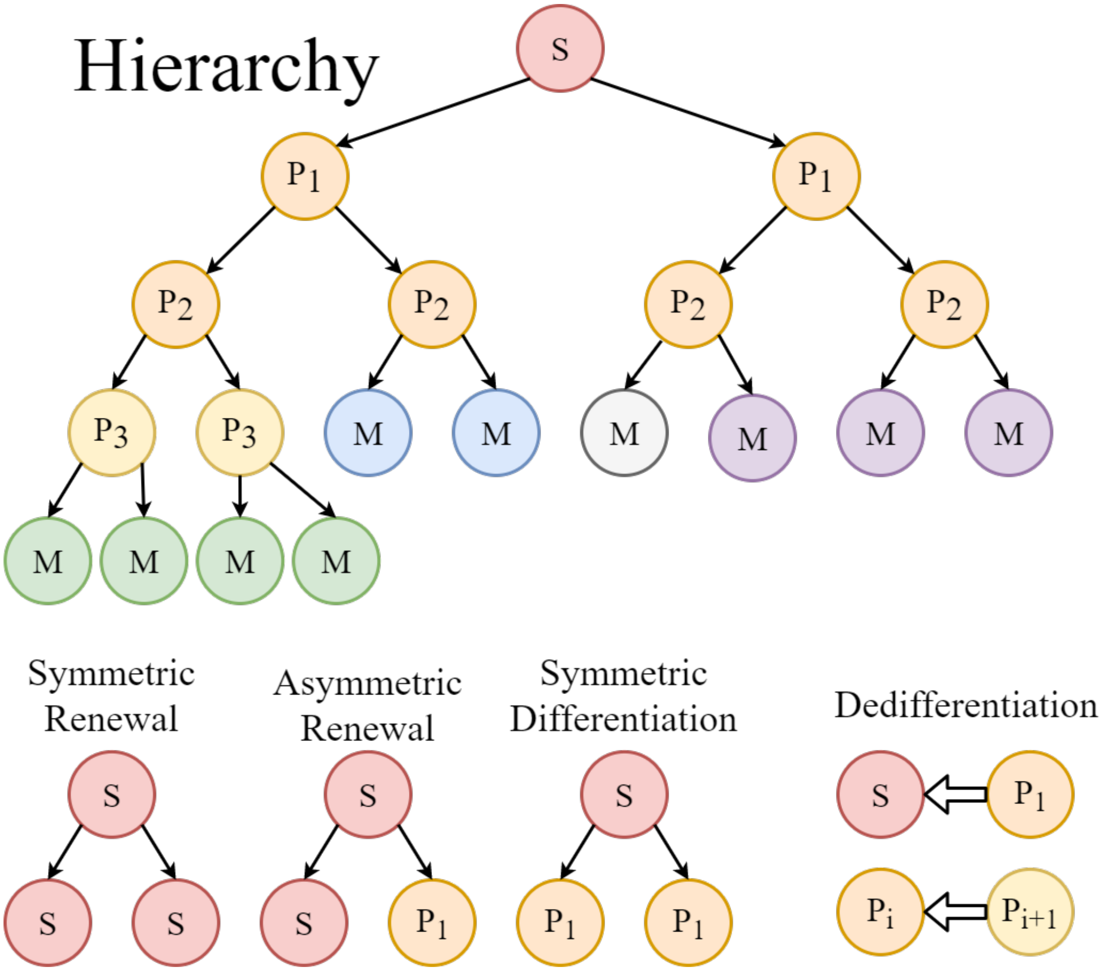

Figure 1.3: Cancer stem cell hypothesis. In the cancer stem cell hypothesis [13], there are two cancer subpopulations: cancer stem cells (CSCs) (marked S, in pink) and non-CSCs, a.k.a. progenitor cells (marked P). Models may include all or some of the following phenomena: a hierarchy of cells beginning with CSCs and ending with fully mature cells (top of figure), progenitor symmetric division into two progenitor cells (shown within hierarchy), CSC symmetric renewal into two CSCs (bottom left of figure), CSC asymmetric renewal into one CSC and one progenitor cell (bottom of figure), CSC symmetric differentiation into two progenitor cells (bottom of figure), and cell death for all or certain types of cells (not shown here), and cell plasticity between one or both subpopulations (bottom right of figure).

to their ability to avoid or prolong telomere shortening and their ability to self-renew [3]. One characteristic of cancer stem cells that has important therapeutic implications is increased resistance [16], especially of quiescent cancer stem cells [17]. Cancer stem cells have more efficient repair mechanisms, including more effective activation of DNA damage checkpoints [17]. Cancer stem cells also exhibit more drug resistant genes and more "inhibitor of apoptosis" proteins than non-stem cancer cells [16].

Due to their self-renewal and unlimited proliferation potential, cancer stem cells play an important role in driving tumour growth [18] and in ensuring that the tumour has the right phenotypes in play to allow for tumour growth [3]. It has been observed that tumours with a higher fraction of cancer stem cells (f_{CSC}) are correlated with a more aggressive tumour [19]. They are key players in tumour initiation (also known as mammosphere formation), tumour resistance, and tumour recurrence [3]. As mentioned above, cancer stem cells are resistant to treatment due to better repair mechanisms and a higher prevalence of drug resistant genes [16]. So although a radiotherapy or chemotherapy session may result in reduction of tumour mass, surviving cancer stem cells may cause the tumour to return [3].

The cancer stem cell hypothesis has been established in certain types of cancers such as leukemia [20], but also in solid tumours such as breast cancer [21] and brain cancer [19, 22]. Cancer stem cells can make up the majority of the tumour, or as little as one percent, but in any case, they are a possible target for cancer treatment [17]. Therapies have been developed to target these important cells in the tumour, e.g. targeting LGR5+ in human colon cancer stem cells. Unfortunately, these therapies are hindered by cell plasticity in cancer cells [23].

Plasticity refers to the ability of cells to change their phenotype, which may be due to stochastically acquired genetic or epigenetic changes governing the CSC state. Cell plasticity can also be viewed as a mechanism that permits cells to modify their roles and characteristics in order to adapt to their microenvironment [8]. One explanation for cell plasticity is the EMT, which refers to a cell's shift from an epithelial phenotype to a mesenchymal phenotype. Epithelial cells are polarized and need to adhere to other cells in order to survive. On the other hand, mesenchymal cells are less polarized, are more invasive, and exhibit stem-like characteristics [24, 25]. More recently, it has been suggested that non-stem cancer cells may undergo a partial or hybrid epithelial-mesenchymal transition and still exhibit stem-like characteristics [26]. Epithelial-mesenchymal transition has been identified as an important mechanism during the process of cancer metastasis, where a primary tumour sends cells to another part of the body to initiate another tumour [3].

Cell plasticity has a large impact on treatment strategy. If there is no cell plasticity, then clinicians can target cancer stem cells to prevent further growth of the tumour. If there is some or little cell plasticity, then clinicians can decrease the number of cancer stem cells, but they can never completely eradicate them. Finally, if there is a large amount of cell plasticity, then targeting cancer stem cells is ineffective since cell plasticity allows them to be restored [27]. Unfortunately, the degree of plasticity is not easily measured and may change during the course of cancer growth. As stated earlier, cancer stem cells are more important during tumour initiation, so they make up a larger proportion of the tumour during early cancer development. In later stages of tumour progression, the fraction of cancer stem cells decreases since less cancer stem cells are needed to sustain growth [14]. These changes may be brought about by changes in plasticity as the cancer progresses.

Protein expression in resistant phenotypes

One way in which cancer cells exhibit resistance is through a change in the normal signaling circuitry. Cancer cells have been shown to lose the function of tumour suppressor genes, increase anti-apoptotic regulators (e.g. Bcl-2, Bcl-xL), increase survival signals (e.g. Igf1/2), downregulate proapoptotic factors (e.g. Bax, Bim, Puma), and interrupt the extrinsic ligand-induced death pathway [3]. These changes in signal and protein expression results in resistance to cell death but also resistance to chemotherapeutic drugs such as docetaxel as discussed in chapter 4. However, with proper treatment sequencing, the use of protein activators or inhibitors can help to manage abnormal protein expression, resensitizing the cancer cells to chemotherapeutic drugs.

1.2.3 Tumour microenvironment

Normal stem cells are maintained and regulated by stem cell niches, which are locations within normal tissue that maintain stem cell self-renewal and multipotency [28]. Normal stem cell niches may also promote the development of cancer stem cells since hypoxic regions that support normal stem cells also promote adaptive gene expression. In the literature, there has been evidence of cancer stem cell niches, which are areas where cancer stem cells are supported by the tumour microenvironment through hypoxia [14, 28]. Cancer stem cells communicate with the normal cells in the surrounding stroma to create a microenvironment that both fosters the cancer stem cell phenotype and protects them from harm, e.g. increasing angiogenesis and hypoxia [29]. Understanding the underlying mechanisms and conditions that promote the cancer stem cell phenotype can aid in designing more efficient cancer treatment strategies.

Some characteristics of the cancer stem cell niche are angiogenesis, necrosis, and increased hemorrhage in the tumour, which leads to increased hypoxia and angiogenesis. Cancer stem cells have been observed to be a source of pro-angiogenic growth factors (AGFs) [30]. Additionally, the hypoxic environment results in uncontrolled angiogenesis and subsequently in abnormal vasculature. This environment protects cancer stem cells from harm, adding to the inherent resistance of cancer stem cells. Since cancer stem cells promote and thrive in these microenvironments, these regions are distributed throughout the tumour to maintain the cancer stem cell phenotype [31].

Interstitial fluid pressure

Another factor in the tumour microenvironment (for solid tumours) is high IFP, which has been correlated with poor prognosis. This is an important barrier to treatment since it prevents the efficient delivery of chemotherapy and immunotherapy drugs. High interstitial fluid pressure in the tumour is related to abnormal angiogenesis since abnormal blood vessels are leaky, increasing the amount of fluid in the interstitium. Additionally, tumours lack lymph vessels to drain out the interstitial fluid. The ineffective blood and lymph vessels as well as the many cells that congregate in the tumour microenvironment results in higher interstitial fluid pressure. As a side note, the use of anti-angiogenic treatment, e.g. VEGF inhibitors, has been shown to normalize vasculature and decrease the interstitial fluid pressure within a tumour [32].

1.3 Mathematical background

1.3.1 Rationale for mathematical modelling of cancer

In this thesis, we develop mathematical models to better understand tumour heterogeneity, the tumour microenvironment, and the effect of treatment on cell death and cancer progression (or regression). Mathematical models can provide valuable insight into the interplay between different cell phenotypes, proteins, and molecules. It can also help us understand the effect of microenvironmental stresses like pressure and drug. Finally, it can help us test and design effective treatment strategies and schedules based on our results and assumptions about cancer growth, heterogeneity, and the tumour microenvironment. Overall, mathematical modelling brings us one step closer to individualized treatment.

1.3.2 Mathematical frameworks for tumour heterogeneity

There are a variety of mathematical models to choose from, e.g. ordinary differential equations (ODEs), partial differential equations (PDEs), CA models, etc. Each of these models has strengths and weaknesses, and each of these models is better suited to different stages or situations of cancer development.

Hierarchy model

Kohandel and Turner [33] developed a hierarchy model for the cancer stem cell hypothesis [13]. As in the cancer stem cell hypohtesis, their model assumes that there exists a hierarchy of differentiation initiated by cancer stem cells. Cancer stem cells have three types of divisions: symmetric renewal (resulting in two cancer stem cells), asymmetric renewal (resulting in one cancer stem cell and one non-stem cancer cell), and symmetric differentiation (resulting in two non-stem cancer cells). Non-stem cancer cells can only proliferate to produce two non-stem cancer cells in the next stage of differentiation. This hierarchy then ends with mature cells which do not divide and eventually die. Cells may also dedifferentiate and move back in the hierarchy due to plasticity. Finally, non-cancer stem cells can also "spontaneously" die. See Figure 1.3 for a schematic of the hierarchy model as well as Table 2.1 for a mathematical description of our modified hierarchy model.

This hierarchical model was used to explore two different scenarios for the link between cancers stem cells and the epithelial-mesenchymal transition [33]. They used mammosphere formation assay data to fit the model and completed different computational experiments to show that the epithelial-mesenchymal transition may be a mechanism for dedifferentiation.

Two-compartment model

When identifying cancer stem cells and non-stem cancer cells experimentally, cell surface biomarkers such as CD44, CD24, or CD133 are used to divide the cells into different subpopulations [17]. A cancer stem cell is then defined as any cell that falls within the region of high or low fluorescence with respect to the biomarker profile expected of cancer stem cells (e.g. $CD44^{+}CD24^{-}$ in breast cancer [21]). In other words, we characterize cells in a binary fashion, separating cells into cancer stem cells and non-stem cancer cells. Note that biomarker fluorescence is a spectrum, i.e. some cells have more biomarker receptors than others. This implies that there are cells that are more stem-like or less stem-like as opposed to a strict binary categorization of stem and non-stem cells.

The two-compartment model is a simplification of the hierarchy model that mimics the *in vitro* characterization of cells (see Table 3.1) [34]. The model considers two compartments of cells representing the positive cells and the negative cells with respect to the given biomarker profile. Due to the ambiguity of cell biomarkers, the positive compartment represents cells that are more stem-like and in the upper half of the cancer stem cell hierarchy, while the negative compartment represents cells that are less stem-like and in the bottom half of the cancer stem cell hierarchy. We assume that the cells in each compartment share the same phenotype so that we only consider two phenotypes. We assume the same phenomena as in the hierarchy model, but with only two compartments representing the two groups of cells. We include the additional assumption that positive cells may die since the positive compartment includes cells that are stem-like but not at the top of the cancer stem cell hierarchy. See Table 3.1 for more details.

In a previous study [34], the two-compartment model was used to study cancer cell plasticity, the stochastic effects on cell dynamics, and its effect on mammosphere formation. They calibrated the model to experimental data [35] to study the dynamics of cancer cells in the limits of large and small population sizes and to study the effect of cell death and initial conditions on mammosphere formation efficiency. They found that stochastic effects play an important role in tumour cell behaviour in small populations.

1.3.3 Agent-based models

Agent-based models are spatial models that simulate the interactions of autonomous individuals within a complex system by prescribing a set of rules dictating the actions of each individual agent [36]. This class of models is important because they capture the spatial, stochastic nature of tumour growth with a small number of cells. These models can be useful in studying both genotypic and phenotypic heterogeneity.

Poleszczuk and Enderling [37] presented an agent-based model for tumour growth based on the hierarchy model [33]. In the model, cells are governed by probabilistic rules that decide the cell's internal state and its interactions with the cell's dynamic local environment. Given its probabilistic nature, it can account for the stochastic nature of single cell kinetics, which is especially important when considering a small collection of cells as we would observe in early cancer development. Their model [37] includes dynamically growing domains, which provides a computationally efficient framework for *in silico* simulations of cellular dynamics and phenotypic heterogeneity in the context of tumour growth.

As in the hierarchy model by Kohandel and Turner [33], two types of cancer cells are considered: cancer stem cells and non-stem cancer (or progenitor) cells. Each cancer cell occupies a single grid point on a two-dimensional square lattice. At each time step (one hour), each cell is updated according to a probability distribution that describes the possible actions for that particular cell. In addition to the assumptions of the hierarchy model [33], cells can undergo "spontaneous" cell death and migration. Spontaneous cell death refers to cell death that is not due to lack of proliferation potential but due to other factors.

Given the spatial nature of these models, additional assumptions are made with respect to the local neighbourhood of a cell. In the agent-based model [37], we consider a Moore neighbourhood for cells, which is the region composed of a central cell and the eight cells which surround it on a two-dimensional square lattice. We assume that cells that are completely surrounded by other cells become quiescent in the sense that they can no longer move, dedifferentiate, or proliferate. It is unclear as to whether cells actively disperse away during early cancer development within the body, so the migration of cells may be due to either the physical dispersion of invasive, cancerous cells or due to the pushing of neighboring proliferating cells.

1.3.4 Systems biology models

The next type of model that we consider are systems biology models. This approach first involves constructing a network representing the system of interest. The network includes the relevant interactions between the biological species of interest, e.g. cells, proteins, or molecules. We then assume that the system is well-mixed, i.e. all species are equally distributed in the system space. Rate laws are then used to convert the network into a system of ordinary differential equations. This ordinary differential equation system can then be used to simulate how the entire system changes with time [38].

Systems biology models are especially important in modelling protein or signalling networks. In Chapters 4 and 5, we construct systems biology models for two different contexts: the Hsp90 protein network within a DTC and the immune system's response to anti-PD-1 immunotherapy.

1.3.5 Parameter estimation

When modelling disease, model parameters may not be available since we are modelling the *in vivo* behaviour of these cells, proteins, and molecules. Often, most of the model parameters are unknown *a priori* due to a lack of direct *in vivo* or *in vitro* measurements to quantify the phenomena at hand. We can apply parameter estimation methods to minimize an objective function representing the error between model predictions and experimental observations of more readily measured metrics. These methods identify plausible parameter values that are consistent with the experimental observations.

When estimating the model parameters, there are two classes of methods at our disposal: global and local. Global methods explore the entire parameter space but can be computationally expensive. Local methods are generally faster than global methods, but the resulting set of parameters may only optimize for a region of the parameter space instead of optimizing across the entire parameter space. There are also hybrid methods that try to combine the best aspects of global and local methods. A hybrid method starts with a global method to find promising regions for the minimum then uses a local optimizer on these regions to find the minimum. The method that we focus on in this thesis is a global method known as the genetic algorithm, ga() in MATLAB, which is a type of evolutionary algorithm. We use this method since evolutionary algorithms are generally applicable and are especially efficient with large parameter spaces. It does not guarantee a global minimum, but it generally works well with a sufficiently large population size [39].

Evolutionary algorithms

Evolutionary algorithms are methods in which each possible parameter set is treated as a distinct individual within a population. The fitness of these individuals is measured by considering the objective function, i.e. a parameter set with a small error will be treated as an individual with a higher fitness [39].

New parameter sets are considered through the selection step, where fit individuals are chosen to undergo recombination. Selection can happen in different ways: truncation, roulette-wheel, or tournament. Truncation means that the top k individuals (according to their fitness) are selected and reproduced until the pool is filled. The roulette-wheel randomly chooses an individual with greater probability for those with higher fitness, and those individuals are reproduced until the pool is filled. Finally, tournament involves taking K individuals and having them participate in tournaments to decide the winner. Each tournament results in an individual that can be used to produce new parameters [39].

The next step is to decide how two parent parameter sets will be combined to create a new individual, i.e. a new parameter set, mimicking the process of sexual reproduction. Given two parent parameter sets in the parameter space, we can set the recombination to choose a parameter set along the line between the two parent parameter sets. This can be a predetermined value, or it can be chosen stochastically. Alternatively, the parameter set can be chosen anywhere along the line connecting the two parent parameter sets with the probability decreasing as the distance from the parent parameter sets increases [39].

Finally, there is a small probability of mutation in an individual. Usually, this is chosen so that the probability of mutation is inversely proportional to the dimension of the problem. All individuals (old and new) then compete to be in the next generation [39].

1.3.6 Sensitivity analysis

Once we have developed a model framework, we can apply sensitivity analysis. Sensitivity analysis is the study of how uncertainty in the output of a model can be explained as a result of uncertainty in the model input. Sensitivity analysis can be used for different reasons such as factor fixing, factor prioritization, and factor mapping. Factor fixing reduces the number of parameters in a system by identifying factors that can be fixed arbitrarily with minimal effect on the output of the system. Inversely, factor prioritization identifies the factors with the most influence on a given output. In other words, it identifies the factors that, when fixed, will reduce the variance of the output most. Finally, factor mapping identifies critical or interesting regions in the parameter space [40]. In this thesis, we utilize sensitivity analysis to identify the key phenomena of a given model, i.e. factor prioritization, since we are primarily interested in identifying opportunities for improved treatment efficacy.

Sensitivity analysis can be differentiated into two types: local and global. Local sensitivities describe the effect of a single small change in an input parameter around a fixed nominal value for a given output. Global sensitivities, on the other hand, describe the effect of simultaneous large variations of all parameters on the outputs. Global sensitivity analysis gives a more comprehensive analysis since it explores more of the parameter space, but it is more computationally expensive than local sensitivity analysis [41].

Local sensitivity analysis

For local sensitivity analysis, we start with our nominal parameter set. The absolute local sensitivity of a given parameter x_i for a given output y around a nominal parameter set $\vec{x}$ is defined in Equation 1.1.

$$S_{\text{absolute}} = \frac{\partial y(\vec{x})}{\partial x_i} = \lim_{\Delta x_i \to 0} \frac{y(\vec{x} + \Delta x_i \vec{e_i}) - y(\vec{x})}{\Delta x_i} \tag{1.1}$$

We can then approximate the absolute local sensitivity using a first-order forward finite difference as shown in Equation 1.2,

$$S_{\text{absolute}} \approx \frac{y(\vec{x} + \Delta x_i \vec{e_i}) - y(\vec{x})}{\Delta x_i} \tag{1.2}$$

where Δx_i is a small perturbation applied to x_i in the nominal parameter set $\vec{x}$. In other words, Equation 1.1 is the difference in output due to the perturbation divided by the magnitude of the perturbation. The relative (or normalized) local sensitivity is then calculated as in Equation 1.3,

$$S_{\text{relative}} = \frac{y(\vec{x} + \Delta x_i \vec{e_i}) - y(\vec{x})}{y(\vec{x})} \times \frac{x_i^*}{\Delta x_i} = S_{\text{absolute}} \times \frac{x_i^*}{y(\vec{x})} \tag{1.3}$$

where x_i^* is the nominal value for x_i. In other words, Equation 1.3 is the absolute local sensitivity scaled by the default parameter and the default output value. The disadvantage of looking at the local sensitivity is that it only characterizes the parametric sensitivities at a specific point in the parameter space. If we want to know how the parameter behaves in the model within the entire parameter space, we need global sensitivity analysis methods [41].

Global sensitivity analysis

One method of global sensitivity analysis is Monte Carlo analysis. We assume that the parameters are independent with normal distributions. We sample N parameter sets to produce N output values. We then plot these output values with respect to each of our parameters and analyze the linearity of the scatterplots [40]. An example from Saltelli et al. [40] is shown in Figure 1.4.

These scatterplots can be quantified by taking the average output values for each parameter value and seeing how much the average varies over the parameter space. This

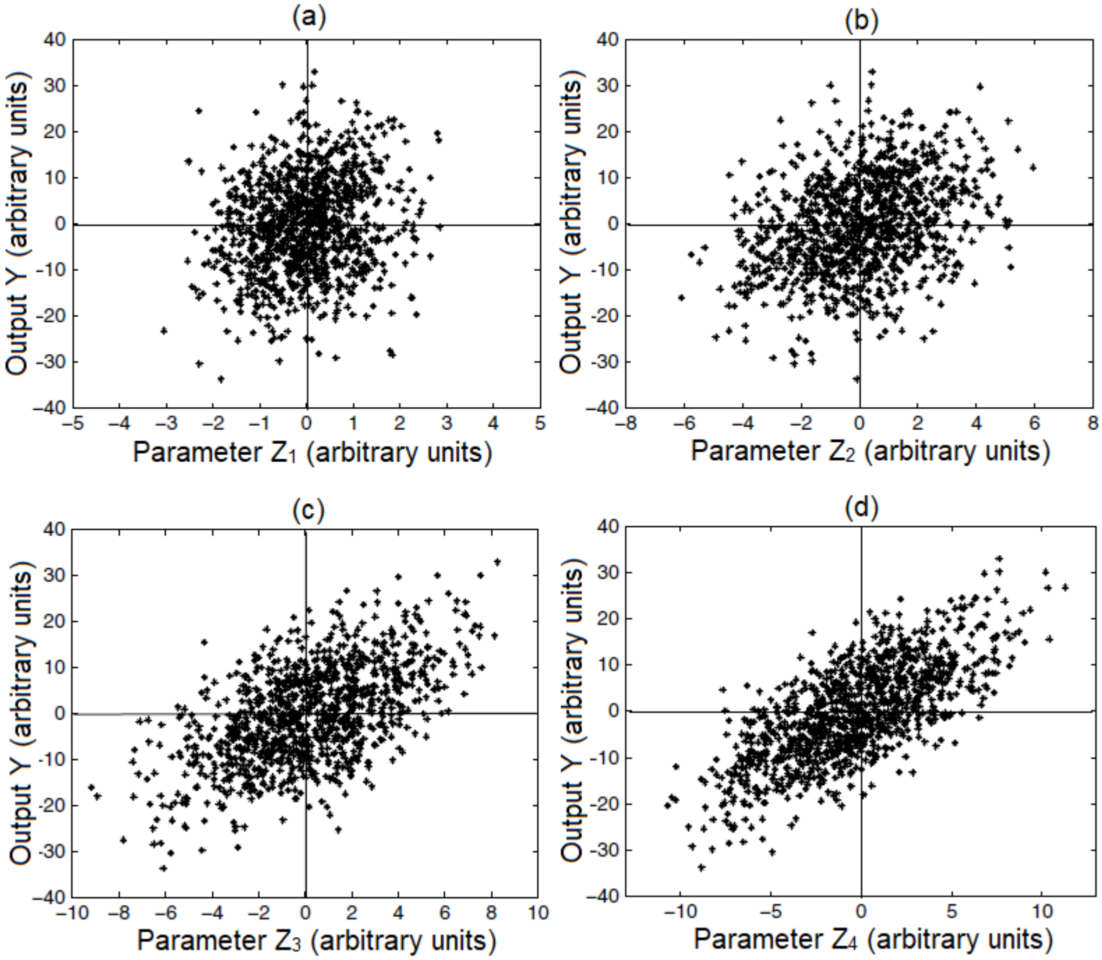

Figure 1.4: Global sensitivity analysis: scatterplots, Figure 1.6 from [40]. If the scatterplot reveals a correlation between the output and the parameter (e.g. a linear pattern), the corresponding parameter has influence over the output. As the variance due to the parameter increases (e.g. a steeper slope), the more influential the corresponding parameter is. The four scatterplots, (a) to (d), are ordered from least influential to most influential.

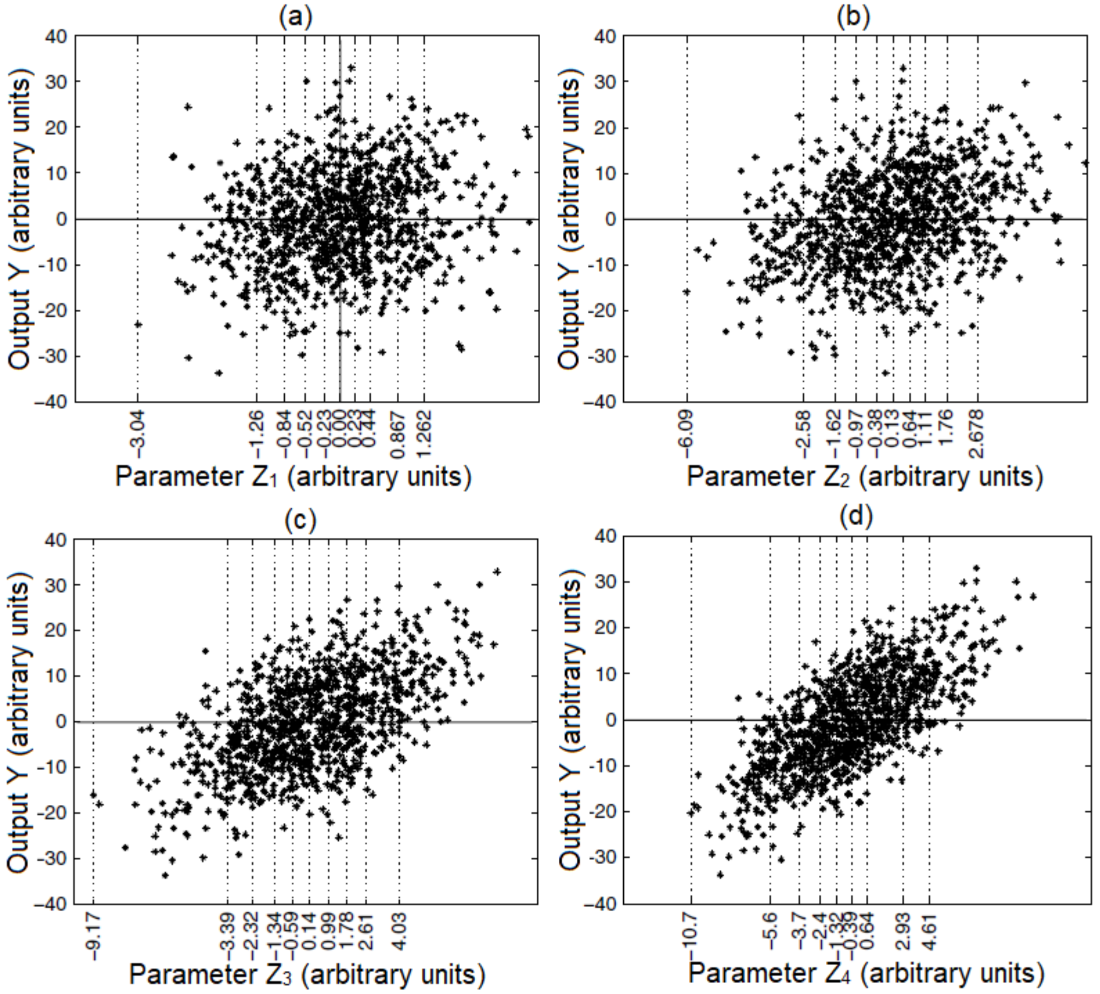

Figure 1.5: Global sensitivity analysis: scatterplots with slices, Figure 1.7 from [40]. Shown is the data from Figure 1.4 with slices where the average of the output data has been taken. The four scatterplots, (a) to (d), are ordered from least influential to most influential.

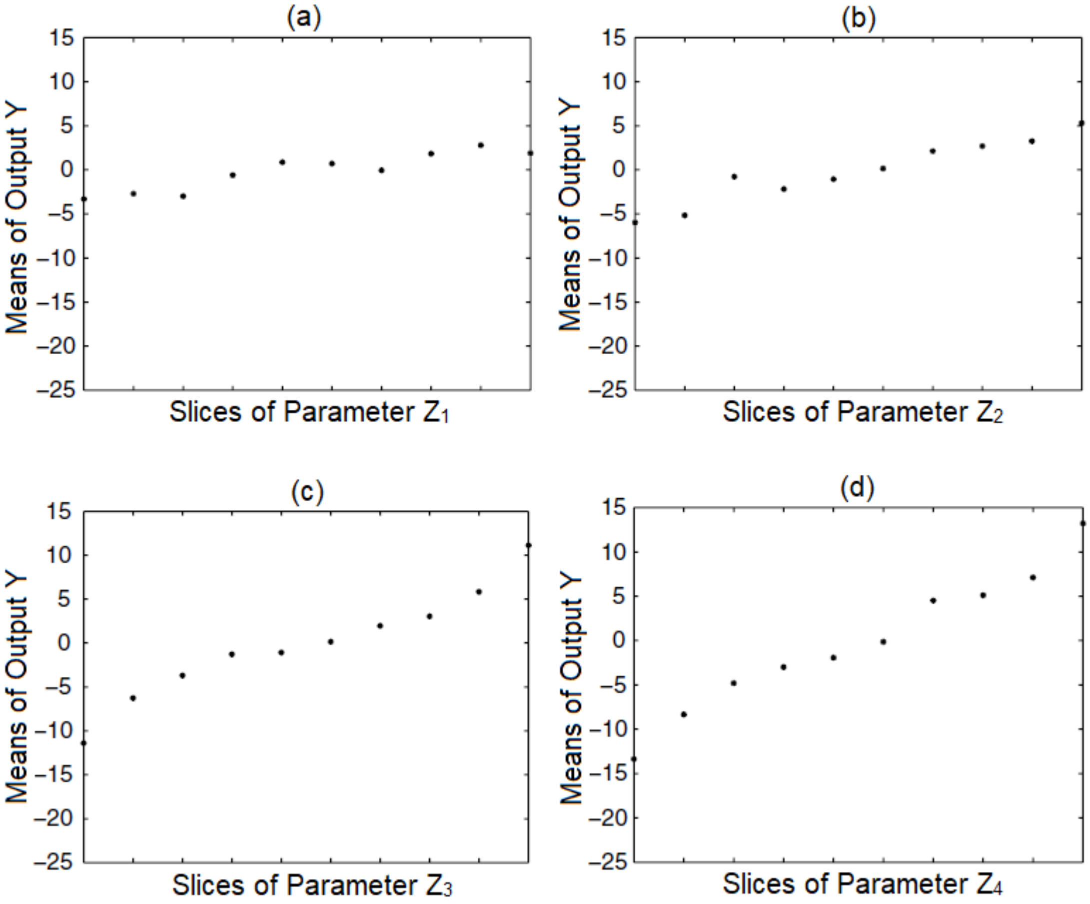

Figure 1.6: Global sensitivity analysis: average of slices, Figure 1.8 from [40]. Shown are the averages of the slices taken in Figure 1.5. If the pattern is more linear than uniformly scattered, then the corresponding parameter is more influential for that output. The four scatterplots, (a) to (d), are ordered from least influential to most influential.

procedure is shown graphically in Figures 1.4 to 1.6. Mathematically, this is described as the variance of the expected value of our output at fixed parameter value as shown in Equation 1.4.

$$V_{X_i}\left(E_{X_{\sim i}}\left(Y|X_i\right)\right) \tag{1.4}$$

Equation 1.4 is known as the first-order effect of X_i (our parameter) on our output. We then define the first-order sensitivity index of X_i on Y as the first-order effect divided by the total variance of our output as shown in Equation 1.5.

$$S_i = \frac{V_{X_i}\left(E_{X_{\sim i}}(Y|X_i)\right)}{V(Y)} \tag{1.5}$$

These definitions as well as higher-order sensitivity indices can be used for factor fixing or factor prioritization [40].

Sampling techniques

We can improve the global sensitivity analysis by improving our sampling technique so that it more comprehensively covers the parameter space. A one-dimensional example of this is shown in Figure 1.7. Different sampling methods include one-at-a-time sampling, full factorial sampling, fractional factorial sampling, Latin hypercube sampling, and combined sampling schemes. In this thesis, we utilize Latin hypercube sampling [40]. As discussed in more detail below, Latin hypercube sampling ensures that we sample each subinterval (e.g. in Figure 1.7) the same number of times, providing more comprehensive coverage of the parameter space.

Latin hypercube sampling works by first splitting up each parameter domain into multiple levels or intervals. We then randomize the order in which we sample those intervals for each model parameter. Then, for n intervals, this process designs kn simulations ($k \in \mathbb{Z}$) where every interval of the parameter domain is sampled k times. We can also additionally ensure that for every n simulations, every interval is sampled. Within each level, we can either choose a specific point such as the midpoint (e.g. line four in Figure 1.7) or we can stochastically choose a point within the interval (line three of Figure 1.7). With these sampling schemes, we can better cover the parameter domain when calculating the sensitivity indices for each of our parameters [40]. An example of a Latin hypercube sampling scheme in two dimensions is presented in Figure 1.8 [40].

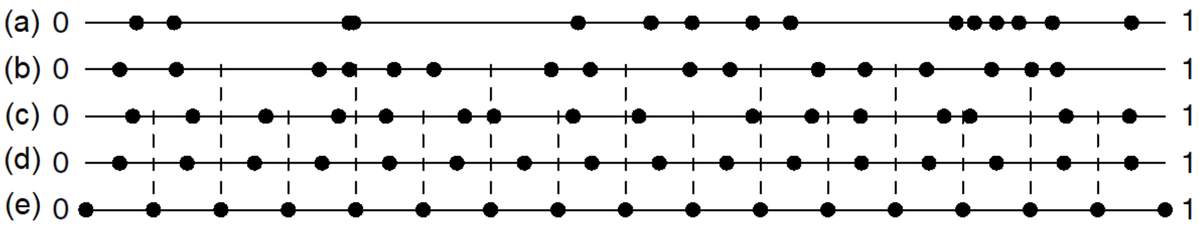

Figure 1.7: Sampling techniques, Figure 2.2 from [40]. This figure shows several ways that a parameter domain from zero to one can be sampled to give a more comprehensive description of the parameter space: (a) sixteen random points are chosen over the entire domain, (b) the domain is divided into eight subintervals and two points are chosen randomly within each interval, (c) the domain is divided into sixteen subintervals and one point is chosen randomly within each interval, (d) the domain is divided into sixteen subintervals and the midpoint is used for each interval, and (e) the domain is divided into sixteen subintervals and the endpoints of all the intervals are used, resulting in seventeen points.

1.4 Thesis outline

In Chapter 2, we develop and demonstrate a framework that uses *in vitro* and *in silico* experiments to characterize cancer cell lines and identify the cellular dynamics during early cancer development. The resulting model can then be subjected to sensitivity analysis to identify the key cellular behaviours to consider when treating specific cancer cell lines. Additionally, we justified the use of a spatial framework in studying mammosphere growth. To our knowledge, this model is the first use of an agent-based model (of the hierarchy model) to study the early cancer stage of mammosphere formation [42].

We demonstrate this process with the breast cancer cell line, MCF-7, and show how the resulting characterization was used to give evidence that progenitor cells are the significant cancer subpopulation during early cancer development for MCF-7 cells. This framework could be used to objectively compare different cell lines and could be used to translate the *in vitro* response to drugs to biopsies from patients.

In Chapter 3, we modify and build on the agent-based model of Chapter 2 to characterize the effect of pressure on mammosphere formation with and without the presence of a chemotherapy drug. To our knowledge, this is the first study to look at the effect of pressure (with and without a chemotherapy drug) on mammosphere formation. We hypothesized that pressure would induce a change in the cellular phenotype from non-resistant ($CD44^{-}$)

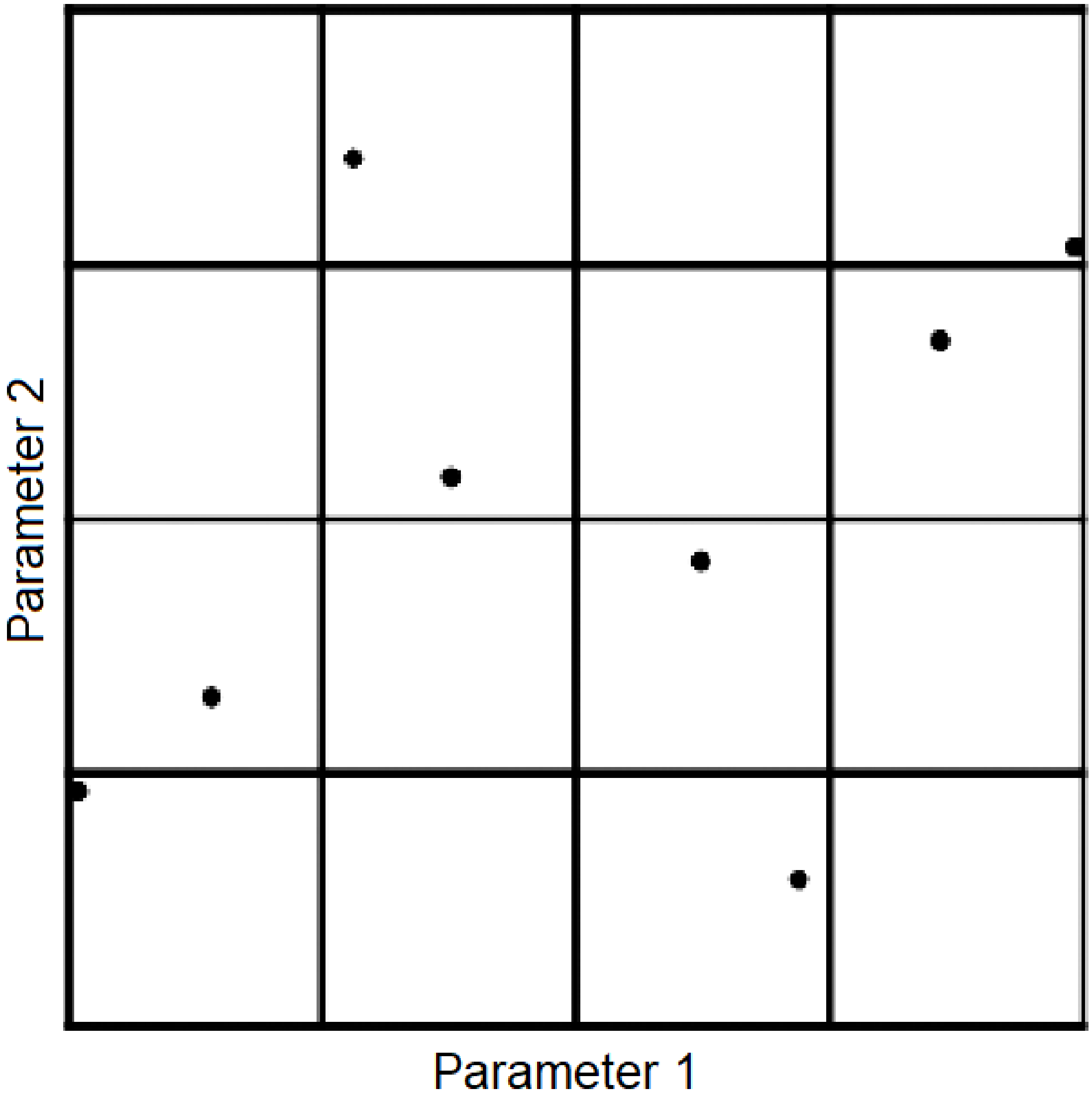

Figure 1.8: Latin hypercube sampling scheme in two dimensions, part of Figure 2.7 from [40]. This figure shows a two-dimensional parameter space where the horizontal direction represents one parameter domain and the vertical direction represents the other parameter domain. Latin hypercube sampling has been used to ensure that each row and each column is sampled the same number of times, which more efficiently covers the parameter space.

to a resistant phenotype ($CD44^+$) since we generally expect adverse conditions to either result in cell death or result in increased resistance to cell death.

Our results from the *in vitro* experiments show that pressure did increase apoptosis but that it did not change the uptake of drug into the cell. Thus, cells in the presence of pressure are fully capable of taking in drug. The results of our *in silico* experiments suggest that pressure more generally increases bidirectional plasticity.

In Chapter 4, we identify the Hsp90 protein network as a means by which drug resistance to the chemotherapy drug docetaxel can be overcome in a DTC. Since Hsp90 expression is increased in cancer cells that are resistant to docetaxel, we hypothesized that an Hsp90-inhibitor, such as radicicol, could be used to overcome the acquired drug resistance to docetaxel. To test this hypothesis, we develop a minimal systems biology model of this network to test our hypothesis and design a treatment schedule for docetaxel and radicicol. To our knowledge, this is the first model to analyze the Hsp90 protein network in a drug-tolerant cancer cell and design a treatment schedule to overcome its drug resistance. Additionally, we hypothesized that a nanoparticle administration would be a more effective drug vehicle compared to a free drug administration due to the different timescales in which drug would be released into the tumour microenvironment. Finally, we use the *in silico* model to identify the most effective improvements that could be made to the drugs in order to improve the efficacy of the treatment sequence.

The *in silico* experiments demonstrate that radicicol can overcome the development of drug resistance in drug-tolerant cancer cells from docetaxel if the treatment sequence takes advantage of the synergy between the two drugs. We also presented evidence that using a nanoparticle formulation of the drugs takes better advantage of the synergy between docetaxel and radicicol compared to the simultaneous release of free drug into the tumour microenvironment. Finally, we identify the intake rate and the decay rate of radicicol as drug formulation properties that would have the greatest impact on increasing the docetaxel-radicicol treatment sequence.

In Chapter 5, we develop a systems biology model to investigate the variability in immune system response to anti-PD-1 immunotherapy. PD-1 (programmed cell death protein 1) is a cell surface molecule that is exhibited on cancer cells and activated T cells. Immune cells that are expressing PD-1 are inhibited when PD-1 is engaged by its ligands (e.g. PD-L1). Anti-PD1 immunotherapy such as nivolumab has been investigated to prevent the inhibition of immune cells by PD-1 ligation. Thus, we would expect nivolumab to result in increased activation of T cells and subsequent cancer regression [43]. However, anti-PD-1 immuno-therapy treatment has shown both positive and negative results in its ability to inhibit tumour growth. We hypothesized that Th1 and Th2 cells determine the immune response [44]. In this study, we develop a systems biology model and utilize sensitivity analysis to identify potential biomarkers for a positive immune response as well as potential networks of interactions that could be investigated further for improved anti-PD-1 immunotherapy response.

We identified two important interaction networks with regards to response to anti-PD-1 immunotherapy: 1) the interaction between cancer cells and CD8$^+$ cytotoxic Tc cells, and 2) the balance between CD4$^+$ Th1 and Th2 helper cells. The latter network is worthy of further research since these factors may be responsive to immunotherapy, given that these cells and cytokines have been studied and modified in other contexts, e.g. autoimmune diseases [45].

In each of the chapters, we investigate heterogeneity at a different level: cellular heterogeneity with and without the effect of the cell microenvironment, variability in protein expression, and variability in immune system response. By developing an *in silico* model to describe the biological phenomena, we can identify the underlying mechanisms at work and provide potential biomarkers and potential improvements that could be tested further.

Chapter 2

An agent-based framework of tumour heterogeneity

In this chapter, we demonstrate a framework that uses *in vitro* and *in silico* experiments to characterize cancer cell lines and identify the cellular dynamics during early cancer development. We demonstrate this process with the breast cancer cell line, MCF-7, and give evidence that progenitor cells play an important role in early cancer development of MCF-7. This framework could also be used to objectively compare different cell lines and could be used to translate the *in vitro* response to drugs to biopsies from patients. Additionally, we justified the use of a spatial framework in studying mammosphere growth.

Dr. Ting Luo was the lab technician of the Mathematical Medicine Laboratory who collaborated on this project. They completed the *in vitro* experiments and wrote the description of the biological experiments. To our knowledge, this model is the first example of an agent-based model (of the hierarchy model) to study the early cancer stage of mammosphere formation. The work presented in this chapter is published [42].

2.1 *In vitro* experiments

All *in vitro* experiments were completed using the breast cancer cell line, MCF-7. These cells were given as a kind gift from Dr. Aaron Goldman at Harvard Medical School.

2.1.1 Cell culture

The human breast cancer cell lines MCF-7, MDA-MB-231, and SK-BR-3 were obtained from ATCC and cultured in DMEM with 4.5 g/L Glucose and L-Glutamine, without Sodium pyruvate (VWR) supplemented with 10% FBS, Certirfied, US Origin, Standard (Sterile-Filtered) (Gibco). The cell culture was kept at 37 °C in an incubator at 5% CO_2.

2.1.2 Mammosphere formation assays

Exponentially growing MCF-7 cells were plated in each well of six-well plates at densities of 100, 200 and 300 cells/cm^2. Plates were kept for 10 to 22 days (see Figure 2.3) in an incubator to allow for the formation of clearly visible clones, which were then fixed with 4% paraformaldehyde in PBS (1x) (w/o Ca++ and Mg++) (VWR) and stained with 0.5% (w/v) crystal violet, pure, indicator (AROS Organics) in dH_2O. The imaging software ImageJ [46] was used to count the number of clones and analyze their sizes. These two measurements corresponded to a cell line's MFE and AMS (see Section 2.3.1).

2.1.3 Flow cytometry

Exponentially growing MCF-7, MDA-MB-231, and SK-BR-3 cells from ATCC were fixed with 4% paraformaldehyde in PBS ((1x) (w/o Ca++ and Mg++) (VWR)) for 30 minutes at room temperature and blocked in 10% goat serum (v/v). Following PBS washes, cells were incubated with CD24-PE and CD44-APC (BD Biosciences, Mississauga, ON, Canada) overnight at 4 °C and analyzed by using an Amnis® brand ImageStream® MkII (EMD Millipore) imaging flow cytometer equipped with 488 nm and 642 nm excitation lasers. Each laser was used to excite a separate fluorescent biomarker. Samples were acquired at 40× magnification. The software INSPIRE® (EMD Millipore) was used for data collection. Image analysis was completed using image-based algorithms in the ImageStream Data Exploration and Analysis Software (IDEAS® v6.1, EMD Millipore).

2.2 *In silico* experiments

2.2.1 Model

In addition to the hierarchy model described in Chapter 1, two assumptions were made when developing this model. First, cells may experience spontaneous death. And second, progenitor cells may exhibit phenotypic plasticity by reverting to a previous cell differentiation state, i.e. one stage backwards in the differentiation hierarchy. Note that both these phenomena are assumed to happen with the same probability for both progenitor and mature cells.

The model summary and parameters are given in Table 2.1 where S represents CSCs, P represents progenitor cells, and M represents mature cells. The rates of division or proliferation are given by ρ_S for cancer stem cells and ρ_P for progenitor cells and mature cells. We assume that progenitor cells of all stages of differentiation have the same probability of proliferation. We assume that mature cells have the same probability of division as progenitor cells but that the result of the attempted division is cell death since mature cells lack the proliferative potential to divide. Given that a cancer stem cell has divided, the rates r_1, r_2, and r_3 represent the probabilities of choosing symmetric self-renewal, asymmetric self-renewal, and symmetric differentiation respectively. We also require that $r_1 + r_2 + r_3 = 1$. Finally, α is the rate of spontaneous death and γ is the rate of dedifferentiation.

As discussed in the section on agent-based models (Section 1.3.3), it is ideal to develop an agent-based model framework to study mammosphere formation since the probabilistic nature of the model can capture the stochastic single-cell kinetics. We thus modified the agent-based framework [37, 47] described in Chapter 1 to study mammosphere formation by simulating mammosphere formation (starting from an initial cell) and by generating outputs that are relevant to mammosphere formation assays, i.e. mammosphere formation efficiency, fraction of cancer stem cells, and average mammosphere size.

To summarize the section on agent-based models (Section 1.3.3), cells are treated as individual agents that are governed by probabilistic rules that decide the cell's internal state and its interactions with the cell's dynamic local environment. Previous work [37] with this model framework considered two types of cancer cells: cancer stem cells and non-stem cancer (or progenitor) cells. These cells are placed on a two-dimensional square lattice, and at each time step (which corresponds to one simulation hour), each cell's action is chosen based on probabilities for all possible actions (e.g. proliferation, spontaneous cell

Model element	Description
CSC hierarchy	$S \to P_1 \to P_2 \to \ldots \to P_n \to M \to \emptyset$
CSC symmetric self-renewal	$S \to S + S$
CSC asymmetric self-renewal	$S \to S + P_1$
CSC symmetric differentiation	$S \to P_1 + P_1$
Progenitor division	$P_i \to P_{i+1} + P_{i+1}, \quad P_n \to M + M$
Progenitor dedifferentiation	$P_i \to P_{i-1}, \quad P_1 \to S, \quad M \to P_n$
Cell death	$S \to \emptyset, P_i \to \emptyset, M \to \emptyset$
Migration Rate	-

Model element	Rate (h^{-1})	Parameter Fit	Reference
CSC hierarchy	-	$n = 12$	[34]
CSC symmetric self-renewal	$\rho_S r_1$	(0.01)(0.014)	fit, [34]
CSC asymmetric self-renewal	$\rho_S r_2$	(0.01)(0.071)	fit, [34]
CSC symmetric differentiation	$\rho_S r_3$	(0.01)(0.914)	fit, [34]
Progenitor division	ρ_P	0.025	fit
Cell death	α	0.01	[37]
Progenitor dedifferentiation	γ	0.042	[34]
Mature cell death	ρ_P	0.025	fit
Migration Rate	ρ_{mig}	0.417	[37]

Table 2.1: Hierarchy model, as presented by Kohandel and Turner [33] with the addition of migration [47]. S represents CSCs, P represents progenitor cells, and M represents mature cells. Parameter values are rounded to three decimal places. ρ_S and ρ_P were the two parameters that we varied to fit the experimental data. For each of the CSC divisions, the parameter fit is shown as the product of the two parameters used.

death, etc.). One additional assumption for the spatial framework is the potential for migration.

Given the spatial nature of these models, additional assumptions are made with respect to the local Moore neighbourhood of a cell. As in previous work [37], we assume that cells that are completely surrounded by other cells become quiescent in the sense that they can no longer move, dedifferentiate, or proliferate. It is unclear as to whether cells actively disperse away during early cancer development within the body, so the migration of cells may be due to either the physical dispersion of invasive, cancerous cells or due to the pushing of neighboring proliferating cells. A flowchart of the agent-based model algorithm is shown in Figure 2.1.

2.2.2 Model parameters

Our full model thus has the following parameters: (1) number of differentiation stages ($N + 1$), (2) probability of proliferation for cancer stem cells (ρ_S), (3) probability of proliferation for non-stem cells (ρ_P), (4) probability of spontaneous death (α), (5) probability of symmetric division (r_1), (6) probability of migration (ρ_{mig}), (7) probability of full (symmetric) differentiation (r_3), and (8) probability of dedifferentiation (γ). r_2 is not included as a model parameter since we calculate r_2 using $r_2 = 1 - r_1 - r_3$.

Our initial test parameters were taken from previous work: Madani's temporal model [34] and Poleszczuk's agent-based model framework [37]. After testing the effect of changing each of the parameters, we chose to modify the proliferation parameters (ρ_S and ρ_P) since they had the most influence on the metrics of mammosphere formation efficiency, fraction of cancer stem cells, and average mammosphere size. Both parameters were manually modified over a range of values to match the experimental data of mammosphere formation efficiency and fraction of cancer stem cells for the breast cancer cell line MCF-7. The parameter fitting process produced a good (but not necessarily unique) fit for the data, which is presented in Table 2.1.

The resulting values for the proliferation parameters were $\rho_S = 0.01$ and $\rho_P = 0.025$. These values correspond to the cell division rate per hour. The corresponding cell doubling times are approximately 69 hours and 28 hours respectively. These values fell within the range of experimental values found in the literature, ranging from cell doubling times for MCF-7 as short as 24 hours [48] and as long as 72 hours [49].

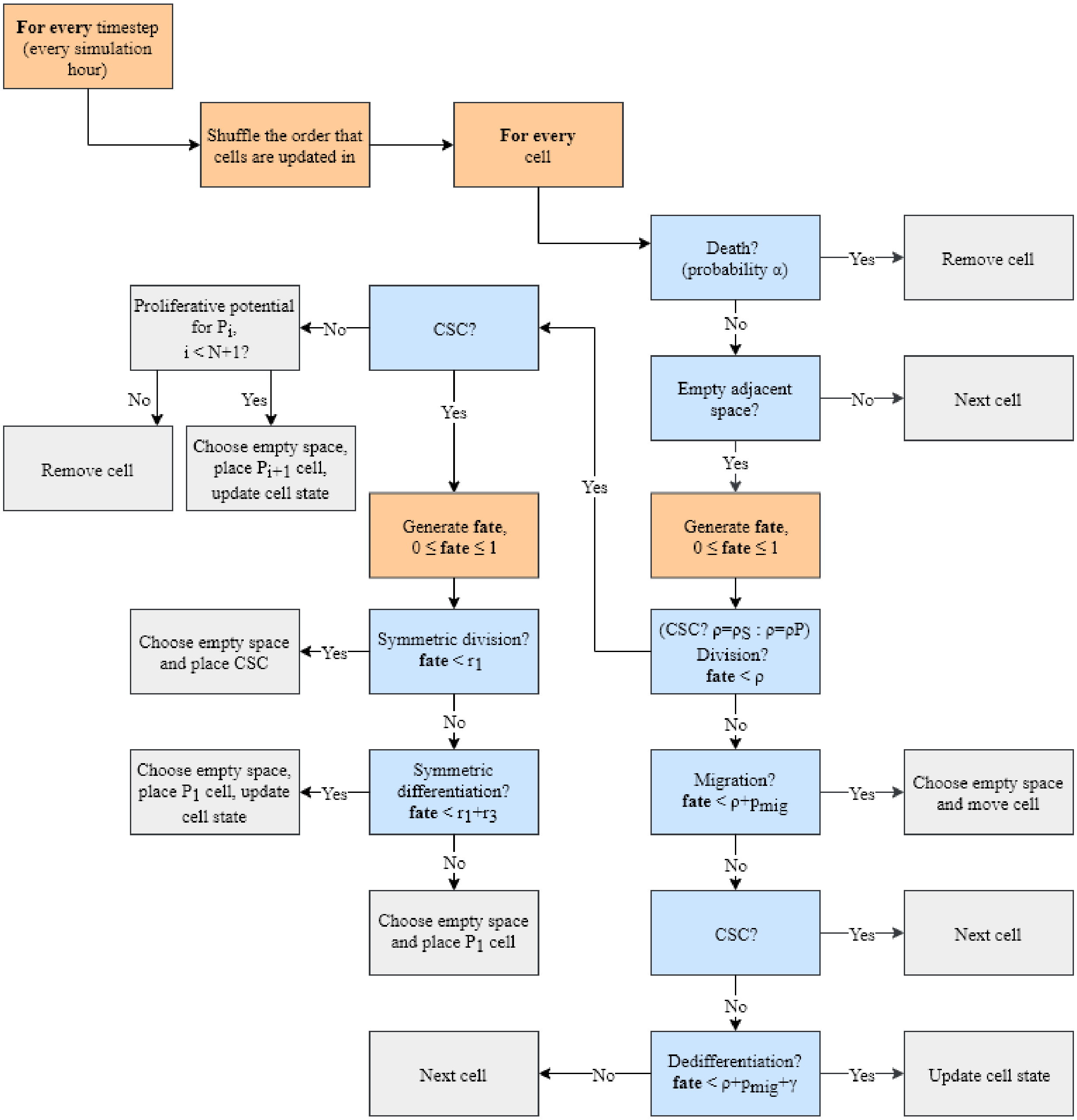

Figure 2.1: Agent-based model flowchart for hierarchy model.

2.2.3 Definitions

In order to compare our *in silico* experiments with our *in vitro* experiments, we defined mammosphere, mammosphere formation efficiency, fraction of cancer stem cells, and average mammosphere size within *in silico* context.

We defined a mammosphere as a colony of cells (of all types) that reached 25 cells before (or at) the day of measurement, which was 12 days. Each simulation represented a single seeded cell in a mammosphere formation assay. The mammosphere formation efficiency was then calculated as the number of mammospheres divided by the total number of simulations run for that experiment. This value captured how efficiently the cells (for a given a parameter set) produced a mammosphere. Each potential parameter set was run with an ensemble size of 10,000 simulations. Each single simulation ran on the order of seconds, so the entire ensemble could take several minutes (in the case of a high rate of spontaneous death) or a few hours (in the case where the cell population is thriving and producing a large mammosphere with many cells).

We defined the fraction of cancer stem cells as the number of cancer stem cells in a mammosphere divided by the total number of cells in the mammosphere. In the literature, sorted subpopulations of the breast cancer cell lines SUM159 and SUM149 return to equilibrium proportions after six days of growth in culture [35]. However, our simulations started with a single cell as opposed to a colony of tens of thousands of cells. Thus, our simulations would most likely take more than six days to reach phenotypic equilibrium. Since our simulations ran for 30 days and reached thousands of cells on average, we assumed that the resulting colonies had run for a sufficient length of time and had a sufficient number of cells for the colony's subpopulation proportions to reach phenotypic equilibrium. We considered the average steady state fraction of cancer stem cells over all successful mammospheres in the mammosphere formation assay as the characteristic fraction of cancer stem cell for that cell line or parameter set. Similarly, the average mammosphere size was calculated as the average number of cells in a simulation.

2.3 Results

2.3.1 Mammosphere formation assays

As described in the Methods section, mammosphere formation assays were completed in the Mathematical Medicine Laboratory at the University of Waterloo run by Dr. Kohandel, as seen in Figure 2.2. The experimental data from these experiments was then used to fit our simulation parameters. To simulate the mammosphere formation assay experiments, we started with a single cancer stem cell and simulated its growth until either the cell count went to zero (i.e. mammosphere eradication) or the prescribed time had passed. We used 30 days for MFE and $f_{\mathrm{CSC}}$to extend the time to steady state and 20 days for AMS and one-at-a-time sampling to more closely match the mammospheres formed in the *in vitro* experiments. An ensemble was thus generated by performing 10,000 simulations. Each single simulation ran on the order of seconds, so the entire ensemble could take several minutes (in the case where many of the cells are dying out) or a few hours (in the case where the cell population is thriving and producing a large mammosphere with many cells).

As described in Section 2.1.2, *in vitro* mammosphere formation efficiency was calculated as the number of mammospheres divided by the number of cells seeded on the dish. The number of mammospheres was counted by using images processed by ImageJ [46]. The ImageJ program scanned for the stained cells by identifying darker pixels within the image and outlining these dark areas within the image. Each outlined dark area corresponded to a single mammosphere. The number of cells was calculated based on the seeding cell density and the surface area of the cell dish used. *In silico*, mammosphere formation efficiency was calculated as the number of successful mammospheres divided by the number of total simulations run (10,000 for these experiments). A successful mammosphere was defined as reaching 25 cells before (or at) the day of measurement, which was 12 days. Note that the length of time before mammosphere counting varies depending on the cell line and the size of the mammospheres [50]. This calculation of mammosphere formation efficiency required computational time ranging from a few seconds to a few minutes.

The simulation was run for 30 days with the set of parameters given in Table 2.1, and as seen in Figure 2.3, the simulation results agree with the experimental data collected for mammosphere formation efficiency for the cancer cell line MCF-7. The mammosphere formation efficiency saturates at about 30%, implying that even with infinite time, only 30% of the seeded cells will produce a mammosphere. These results are based on an ensemble of 10,000 simulations, which gave us sufficiently smooth results to compare with the experimental data.

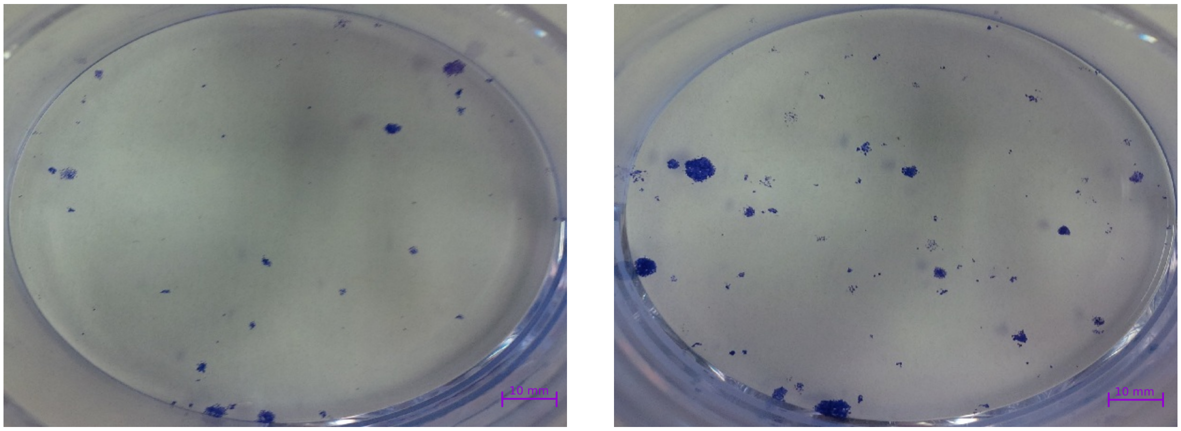

(a) seeding density = 100 cells/cm^2

(b) seeding density = 200 cells/cm^2

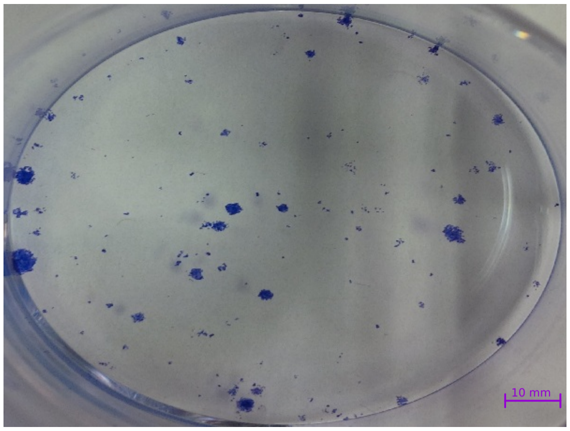

(c) seeding density = 300 cells/cm^2

Figure 2.2: MCF-7 mammosphere formation assays. Each figure shows a mammosphere formation assay after 18 days of growth for a given seeding density. Cells have been stained blue and each group of cells represents one mammosphere. We can see that higher seeding density results in more mammospheres. A scale of 10mm is given.

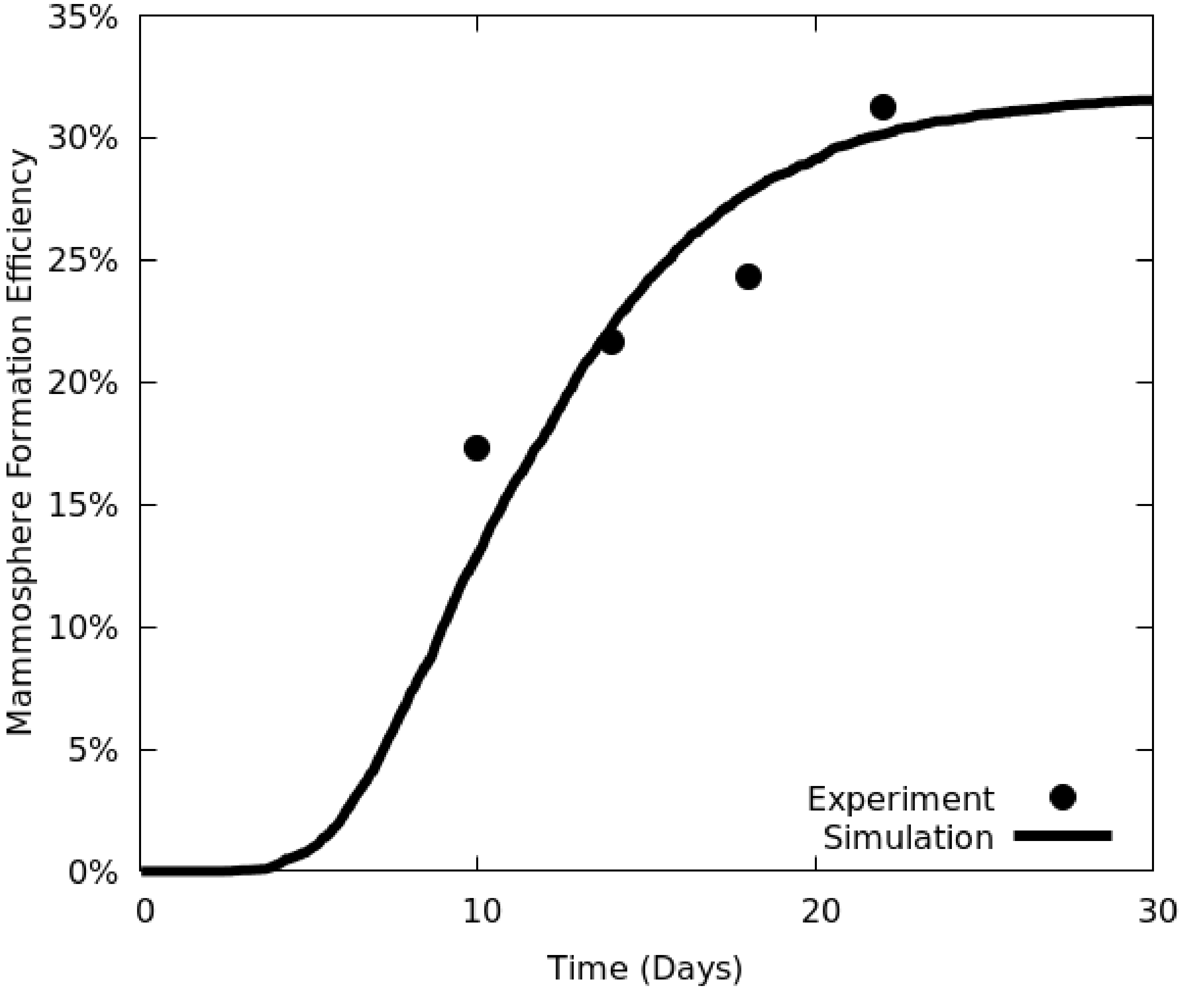

Figure 2.3: Mammosphere formation efficiency vs time. Mammosphere formation efficiency for the simulation are shown for the set of parameters given in Table 2.1 with data points from experimental MFE data with the MCF-7 cancer cell line. The ensemble size was 10,000 simulations, and a successful mammosphere was defined as reaching 25 cells. We can see that the simulation results agree with the experimental data collected and that the mammosphere formation efficiency saturates with time.

2.3.2 Fraction of cancer stem cells

We utilize two different fluorescent biomarkers, CD24 and CD44, for identifying the different cell subpopulations. Traditionally, cancer stem cells have been identified as $CD44^{+}CD24^{-}$ cells [17, 21]. However, $CD44^{+}CD24^{+}$ cells have also been shown to exhibit stem-like characteristics such as drug resistance [51]. Thus, we considered $CD44^{+}$ cells as cancer stem cells.

Cells exhibit different amounts of cell surface biomarkers, and we can measure this using imaging flow cytometry. Fluorescent tags targetting the cell surface biomarkers are used to label the different cell populations. Imaging flow cytometry then measures the fluorescence intensity for the two biomarkers for each individual cell. The results are plotted as a scatterplot as shown in Figure 2.4. For any given cell line, a gate is chosen to separate the CSCs from the non-CSCs. The result is a number describing the proportion of cancer stem cells in the tumour growth [52].

In the simulations, an ensemble of 10,000 simulations was run for comparison. Each single simulation runs on the order of seconds, so the entire ensemble may take several minutes (in the case where many of the cells are dying out) or a few hours (in the case where the cell population is thriving and producing a large mammosphere). In the simulations, the fraction of cancer stem cells was calculated as the number of cancer stem cells in a mammosphere divided by the total number of cells.

The experimental data of various cell lines showed that the fraction of cancer stem cells can vary from cell line to cell line (see Appendix A for other cell lines). Note that these values are also dependent on the gating used for the cell line since there is no current standard expression level for identifying a cancer stem cell based on its biomarkers [17]. In other words, the gate used to separate the different cell subpopulations could be placed differently depending on how the cells are distributed in the fluorescence intensity space. Thus, the measurement of positive cells and negative cells may differ from experimentalist to experimentalist based on how they choose to configure their measurement.

During the parameter fitting process, we only considered parameter sets that resulted in a fraction of cancer stem cells less than 30% based on our experimental observations. In other words, we used the fraction of cancer stem cells data to check that the parameter fit was biologically relevant. Our simulation (with the set of parameters given in Table 2.1) had a steady state fraction of cancer stem cells of approximately 5%, which falls in our acceptable range of values.

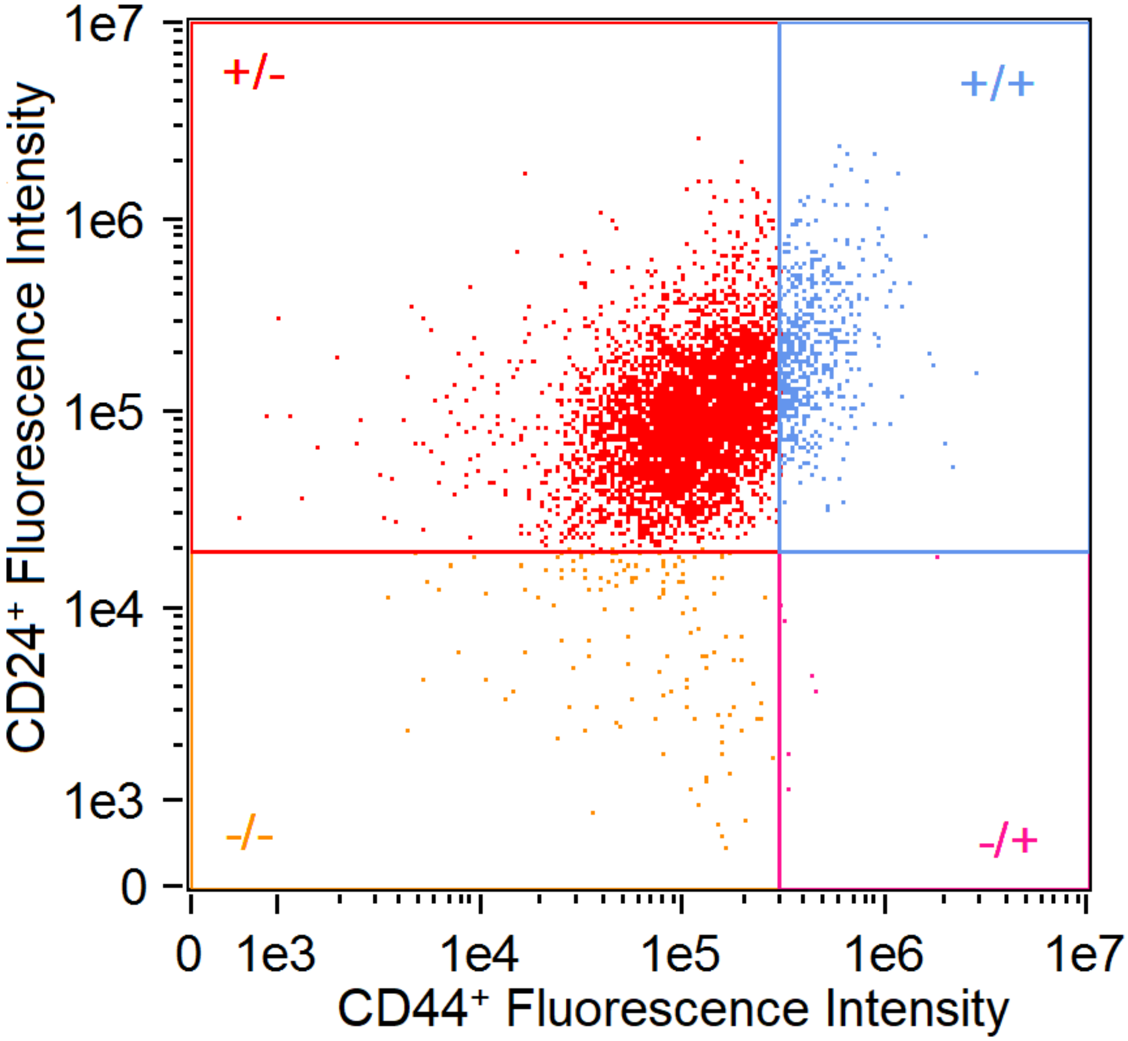

Figure 2.4: Flow cytometry results for breast cancer cell line MCF-7. The biomarkers CD24 (y-axis) and CD44 (x-axis) were used to identify different cell subpopulations. We considered CD44$^+$ cells as cancer stem cells since these cells have been shown to exhibit stem-like properties.

Note that the units for fluorescence intensity are arbitrary since fluorescence is compared through relative expression. These results are quantified in Table 2.2.

	MCF-7 Cells	Colony %		Simulation %
All cells	5398	100 %		100 %
CD44$^-$	4796	$\sim$ 89 %		$\sim$ 95 %
CD44$^+$	539	$\sim$ 10 %		$\sim$ 5 %

Table 2.2: Quantification of the flow cytometry results, given in Figure 2.4. We can see that the subpopulation corresponding to cancer stem cells makes up approximately 10% of the mammosphere population. In our parameter fitting process, we only considered parameter sets that resulted in a fraction of cancer stem cells less than 30% due to the variability in choosing a gate. The simulation results were for the set of parameters given in Table 2.1, and the simulation fraction of cancer stem cells was approximately 5% on average after 30 days.

2.3.3 Average mammosphere size

After fitting our parameters to the mammosphere formation efficiency measurement and ensuring that we had a biologically relevant fraction of cancer stem cells measurement, we had two possible parameter sets with the same parameters except for the presence or lack of migration. The final piece of data that we used to fit our data was the average mammosphere size.

In the experimental studies, the imaging software (ImageJ [46]) was used to count all the mammospheres in each image and measure their relative sizes. Thus, we had a measure of the average mammosphere size, as seen in Figure 2.2. In the simulations, each cell was tracked so that we could check for any changes to its location and state. To measure the average mammosphere size, the number of cells in each simulation was averaged over all mammospheres in the ensemble. Like the f_{CSC}, this calculation can take several minutes to several hours to complete depending on the number of successful mammospheres.

Given that the diameter of an MCF-7 breast cancer cell is $\sim$20-24 μm and assuming a circular mammosphere shape, d = 1mm corresponds to approximately 41.67 to 50 cell-widths, which corresponds to an area of approximately $1,363$ to $1,963$ cell-widths^2 = $O(10^3)$ cells. In our simulations, after about 18 days of growth, we had an average mammosphere size of $\sim$331 cells. Thus, the average diameter size for our mammospheres was between 0.1 and 1 millimetres. We can compare these results with the experimental results in Figure 2.2. Although those results are for 14 days, we can see that there are only a few mammospheres that reach diameters above 1 millimetre, but the majority of the mammospheres are quite small in comparison. Thus, it is reasonable to assume that the average mammosphere would be between 0.1 and 1 millimetre in diameter.

Thus, we justified the need for migration as a phenomenon in our model. In the absence of migration, the average mammosphere size of the mammospheres in our simulation at 18 days is $\sim$117 cells. This suggests that the average diameter for a given mammosphere is closer to 0.1 millimetres. Since the result with migration was closer to what was observed in Figure 2.2, we assumed that migration should be included in our model. The phenomenon of migration has not been biologically observed in the early stages of tumour growth since the tumour is not yet detectable, so the migration rate in our simulation could roughly reflect cells pushing each other to make space for cell division.

When comparing the images of the *in vitro* mammospheres with the *in silico* mammospheres after 20 days (see Figure 2.5), we found that including migration resulted in a more realistic tumour shape and size. Without migration, the mammosphere size was reduced by self-inhibition, as observed in the literature [37]. As stated earlier, one of the assumptions of the spatial framework was that a cell that was surrounded by other cells would go into quiescence. In other words, a cell with no adjacent space can not migrate, dedifferentiate, or proliferate but can still die spontaneously and go through dedifferentiation. Thus, migration allows cells to move away from the tumour core, creating space for cells to proliferate and migrate, resulting in faster growth.

In these experiments, we can ignore three-dimensional growth effects since cells in an *in vitro* mammosphere formation assay grow in a monolayer until the cell dish approaches confluence. However, a three-dimensional tumour *in vivo* would likely experience self-inhibition if there is no mechanism of migration in the tumour. Biologically, this would translate to cells pushing outwards during proliferation or to the active dispersal of cells.

2.3.4 One-at-a-time sampling

We performed one-at-a-time sampling on each of the fitted model parameters to obtain the key parameters in our model [40]. Each of the parameters of our model (see Table 2.1) was perturbed by ±50%, resulting in a higher value at 150% and a lower value at 50%. A single exception was made for r_3 since the nominal value was $r_3 = 0.91$. A perturbation of +50% would break the constraint $0 \leq r_i \leq 1$ and $r_1 + r_2 + r_3 = 1$, so it was set to the maximum value within constraints, i.e. $r_3 = 0.99$.

For each perturbed parameter set, an ensemble of 10,000 simulations was generated and the average mammosphere size, fraction of cancer stem cells, and mammosphere formation

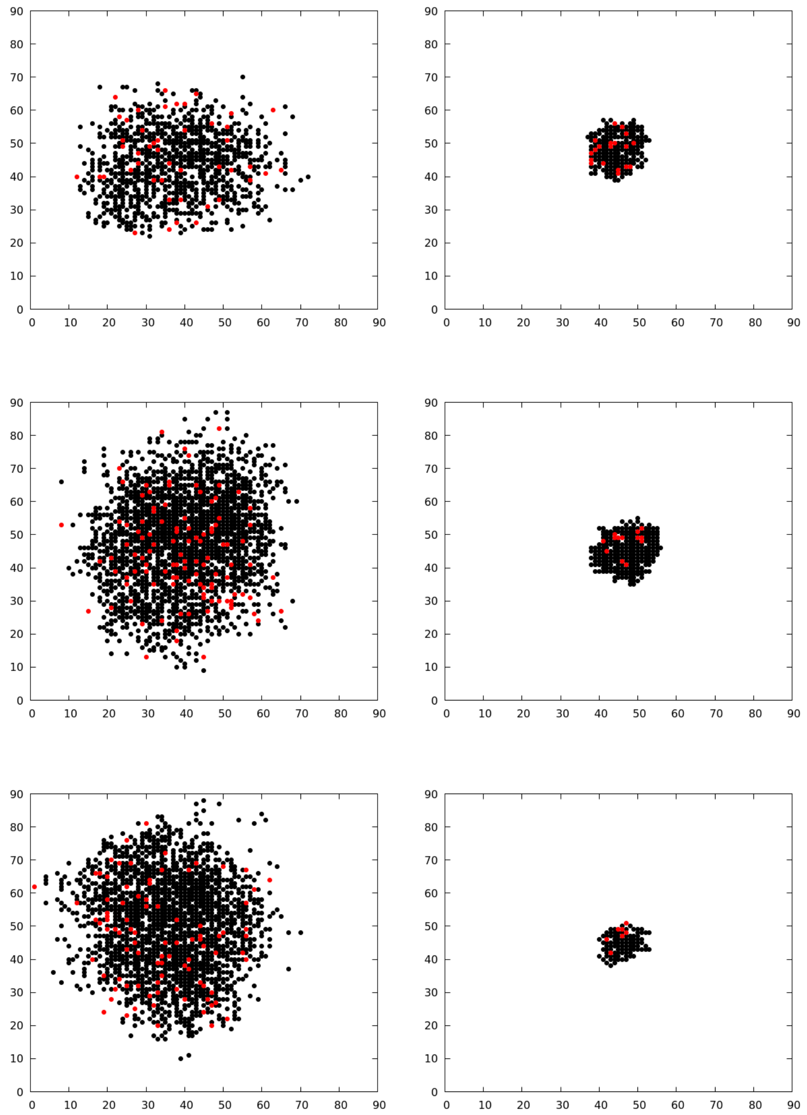

(a) with migration

(b) without migration

Figure 2.5: Mammosphere simulations: (left column) with migration, (right column) without migration. Progenitor cells are shown in black, and cancer stem cells are shown in red. Each plot is shown on a grid that is 90 cell-widths tall and 90 cell-widths wide. These plots represent growth of successful mammospheres after 20 days of growth. Without migration, mammosphere growth is reduced by self-inhibition, but with migration, the cells experience continued growth.

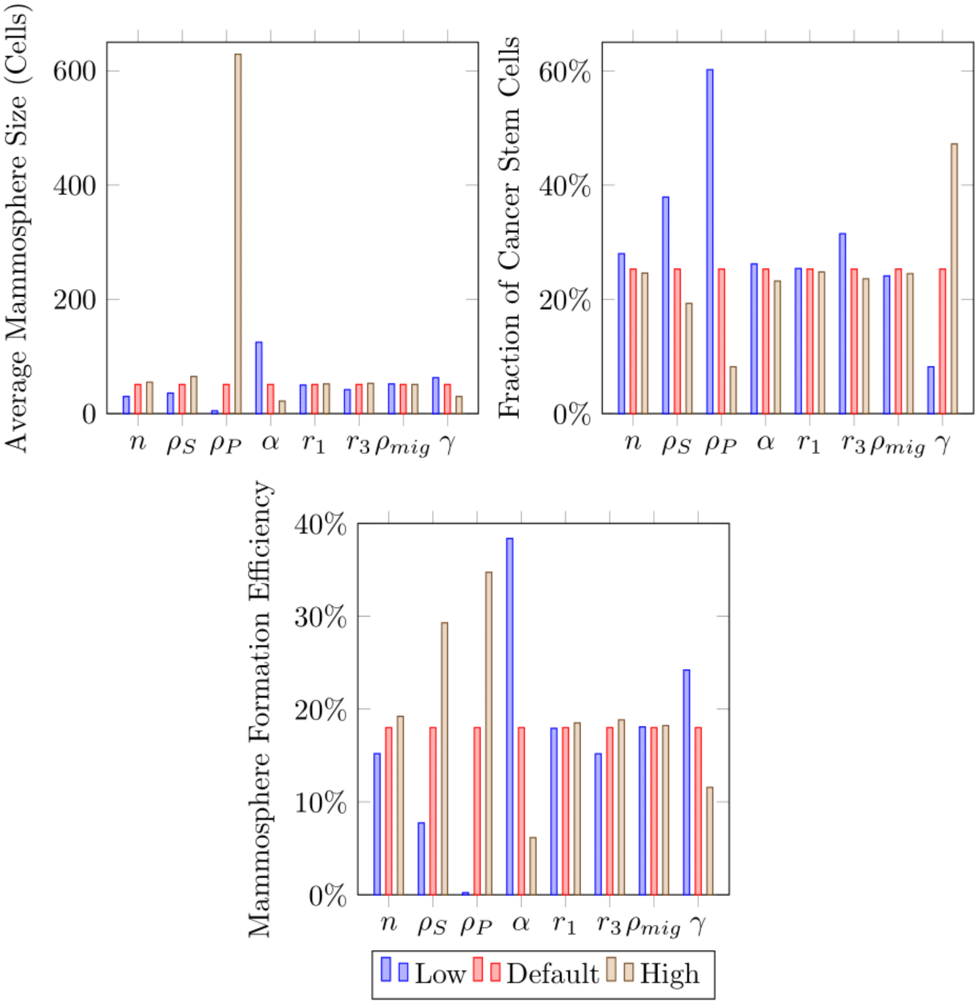

Figure 2.6: One-at-a-time sampling. Each of the parameters of our model (see Table 2.1) was perturbed by ±50%, resulting in a higher parameter value at 150% and a lower parameter value at 50%. A single exception was made for the positive perturbation for r_3, which was set to the maximum valid value. For each perturbed parameter set, an ensemble of 10,000 simulations was generated and the average mammosphere size, fraction of cancer stem cells, and mammosphere formation efficiency were calculated. The relative local sensitivity is then calculated and plotted. ρ_P was the most significant factor for all properties. Other significant factors included γ, ρ_S, and α.

efficiency were measured after 20 days. One-at-a-time sampling was completed and the resulting metrics of average mammosphere size, fraction of cancer stem cells, and mammosphere formation efficiency were plotted [40]. From our results (as seen in Figure 2.6), we found that the proliferation of progenitor cells (ρ_P) was the most significant factor for all properties. Other significant factors included the probability of dedifferentiation (γ), the proliferation rate of cancer stem cells (ρ_S), and the probability of spontaneous death (α).

We found that the most significant factors in MCF-7 mammosphere formation were the proliferation of progenitor cells, the probability of dedifferentiation, the proliferation rate of cancer stem cells, and the probability of spontaneous death. Overall, these four factors suggest that progenitor cells play an important role in early tumour development of MCF-7 cells. Even though cancer stem cells have gotten a lot of attention in terms of targeted therapy, these results give evidence that researchers developing targeted therapy should investigate the non-stem portion of the tumour when considering how to limit early MCF-7 cancer growth.

The proliferation of progenitor cells suggests that the primary role of progenitor cells within the mammosphere is to proliferate often. Thus, the uninhibited initial growth of a mammosphere is driven by the progenitor cells present.

The probability of dedifferentiation seems to indicate that mammosphere formation is driven mainly by the progenitor cells that are able to dedifferentiate back to cancer stem cells as needed. One interesting result is that if progenitor cells are too prone to dedifferentiation, then this results in a lower mammosphere formation efficiency and lower average mammosphere size, even though the fraction of cancer stem cells increases. Thus, cancer stem cells are necessary for continued growth, but excessive dedifferentiation will deplete the progenitor population and result in eventual annihilation of the colony.

The third most important factor is proliferation of cancer stem cells, which suggests that the cancer stem cells need to be proliferating enough to get the mammosphere started. It may also indicate that the cancer stem cell needs to produce an adequate supply of progenitor cells through asymmetric and symmetric differentiation in order for the mammospheres to succeed. In other words, increased proliferation of cancer stem cells results in more cancer stem cells but more importantly, more progenitor cells. Finally, the probability of spontaneous death suggests that the increased killing of cells is a key factor in controlling mammosphere formation.

2.4 Discussion

In this chapter, we have demonstrated a process in which experimental *in vitro* studies and computational *in silico* studies can be used together to characterize breast cancer cell lines based on their mammosphere formation dynamics. To our knowledge, this model is the first example of an agent-based model (of the hierarchy model) to study the early cancer stage of mammosphere formation [42]. Data from mammosphere formation assays and image flow cytometry can be used to fit the model parameters, giving us a mathematical description of the cancer cell line under consideration.

The resulting model can then be subjected to one-at-a-time sampling to identify the key model parameters, which correspond to specific cellular behaviours [40]. The changes in the key metrics of average mammosphere size, fraction of cancer stem cells, and mammosphere formation efficiency give an indication of what the key mechanisms are during early cancer development for that particular cell line. One-at-a-time sampling of similar cancer cell lines can also give us insight into the factors that should be considered in treatment design. Hypothetically, one could take a biopsy of a tumour from a patient and compare it to cell lines that have been previously characterized by their *in vitro* characteristics. These comparisons can help us understand what dynamics are at work for a given patient's tumour and what treatment options would be most effective to kill the cancerous cells.

In our demonstration using MCF-7 breast cancer cells, we produced a mathematical description of the growth dynamics of MCF-7 mammosphere formation. With the resulting model, we gave evidence that progenitor cells are the driving force behind mammosphere formation in MCF-7. Although cancer stem cells play a key role, these one-at-a-time sampling results indicate that progenitor cells should be our primary focus for early stages of MCF-7 growth.

This characterization of cancer cell lines can also be used as a method of objectively comparing different cell lines. It can be useful to compare the cellular dynamics of different *in vitro* cell lines, but it is also valuable to have a method of comparing a patient's biopsy with experimental cell lines. This characterization of cell lines is useful in the design of *in vitro* experiments but also in treatment design.

The resulting *in silico* model can be used as a substitute for *in vitro* experiments. *In silico* experiments are more cost-effective and efficient than their *in vitro* counterparts, so it is valuable to have an *in silico* model as an alternative, especially in the early stages of hypothesis generation and testing.

Another important result of this work is that we justified the use of a spatial framework when studying mammosphere growth. The only cellular activity unique to the spatial model is migration. Migration refers to a cell's ability to either migrate outwards or push cells further away to promote further growth. In the absence of this movement or pushing outwards, we find that tumour development is limited due to self-inhibition. Self-inhibition refers to the phenomena where cells become quiescent due to lack of space in the surrounding area. In other words, cells are not able to complete certain actions due to lack of space. In this study, we gave evidence that migration was a necessary assumption in order to properly recreate the observed *in vitro* mammosphere formation dynamics when we assume that cells experience quiescence when completely surrounded by other cancer cells.

Biologically, migration may be explained as the cancer's lack of adhesion inhibition, in which normal cells stop growing when they are in contact with other cells [53]. Alternatively, epithelial-mesenchymal transition may allow tumour cells to physically disperse from the inner core of the tumour, allowing for accelerated growth [24, 25]. These cancer characteristics are thus key phenomena in capturing early cancer development dynamics. As stated earlier in Section 2.3.3, we can ignore three-dimensional growth effects since cells in an *in vitro* mammosphere formation assay grow in a monolayer until the cell dish approaches confluence. However, a three-dimensional tumour *in vivo* would likely experience self-inhibition if there is no mechanism of migration in the tumour. Biologically, this would translate to cells pushing outwards during proliferation or to the active dispersal of cells.

2.4.1 Limitations of the model

One limitation of the model is our choice of initial conditions. In the corresponding *in vitro* mammosphere formation assay experiment that we are trying to recreate, the type of cell to be considered is unknown. In other words, we have no information about the initial conditions of the *in silico* experiment. We thus assume that every simulation begins with a cancer stem cell, which is unlikely to be the case in reality. Alternatively, we could randomly set the initial conditions to a random type of cell, but then we would need to make assumptions about the frequencies of each cell type. To avoid the effect of this assumed distribution, we set the initial condition as a single cancer stem cell.

One spatial assumption of the model that was adopted from previous work is that cells that are completely surrounded by other cells cannot proliferate, move, or dedifferentiate. In reality, space is not necessary for dedifferentiation since it reflects either a mutation or an epigenetic change in gene expression. It may be more biologically realistic to allow for dedifferentiation in the absence of space since quiescent cells continue to mutate [54].

In the fraction of cancer stem cells measurement, we used simulations that had run for 30 days and had reached average colony sizes in the order of thousands of cells. However, *in vitro* flow cytometry experiments normally require around one million cells to adequately capture all of the subpopulations. Thus, the resolution of our fraction of cancer stem cell measurements could be improved by allowing one simulation to run for a longer period of time so that it reaches a colony size of one million cells.

2.4.2 Future work

Future work with this framework includes applying this framework to other cell lines, improving the identification of key cellular behaviours by using sensitivity and uncertainty analyses, incorporating the tumour microenvironment, and modifying the model into three dimensions. The methodology presented in this work could be applied to other cell lines (e.g. MDA-MB-231, SKBR3) of breast cancer and of other cancers (e.g. glioblastoma). This characterization of various cell lines could help us understand the heterogeneity between cell lines of the same cancer type as well as the inter-patient heterogeneity that is observed clinically. Understanding the dynamics of tumour heterogeneity could also aid in treatment design as the key actions taken by cells are identified. In other words, we could understand the dynamics at work that promote or hinder response to specific drugs by comparing responsive and unresponsive cell lines. This insight could also aid in the development of new drugs that can target the key mechanisms at work in different cell lines.

This work could be improved by using sensitivity and uncertainty analyses. In this work, we used one-at-a-time sampling to identify the key cellular behaviours for a given cell line [40]. This analysis could be improved by using local sensitivity analysis since local sensitivity analysis identifies the influential parameters after a very small perturbation [41]. By only using a small perturbation, we are reducing the likelihood that we have moved into a parameter subspace than that which characterizes our cell line. Additionally, uncertainty analysis could be used to evaluate our parameter estimates by calculating the confidence intervals for each parameter. Thus, we can evaluate the probability that our set of parameters is an accurate description of a given cell line [55].

In Section 1.2.3, the tumour microenvironment was identified as an important factor in cell heterogeneity and plasticity [30, 31, 56]. This model could be combined with a partial differential equation model for various microenvironmental factors such as hypoxia, angiogenesis, drug, or pressure (as in Chapter 3). The resulting hybrid model could then be fit to *in vitro* measurements of such phenomena to describe the phenotypic changes as a result of the microenvironment. Fitting to *in vitro* data could also help us understand the spatial factors involved in the development of cancer stem cell niches, as observed in the literature.

This model could also be extended into three-dimensional space. Ideally, this would be supported by three-dimensional spheroid *in vitro* colony data, i.e. the three-dimensional equivalent of the mammosphere formation assay [57]. One benefit of using a three-dimensional setup is that we would be measuring anchorage-independent growth, which is characteristic of cancer stem cells. Thus, three-dimensional tests would be a more robust test for cancer stem cell activity.

Chapter 3

The effect of pressure and drug on mammosphere formation

In this chapter, we modify and build on the agent-based model of Chapter 2 to characterize the effect of pressure on phenotypic plasticity during mammosphere formation with and without the presence of a chemotherapy drug. We hypothesized that pressure would induce a change in the cellular phenotype from non-resistant (CD44^{-}) to a resistant phenotype (CD44^{+}) since we generally expect adverse conditions to either result in cell death or result in increased resistance to cell death for cells that survive.

To test our hypothesis, *in vitro* mammosphere formation assays and flow cytometry experiments were completed in the presence of pressure. Additionally, cell cycle and drug uptake data were collected since we hypothesized that pressure would result in increased apoptosis and decreased drug uptake. Finally, our *in silico* model was fit to mammosphere formation and flow cytometry data to characterize the cells under different microenvironmental conditions.

Our results from the *in vitro* experiments give evidence that pressure did increase apoptosis but that it did not change the uptake of drug into the cell. Thus, cells in the presence of pressure are fully capable of taking in drug. The results of our *in silico* experiments give evidence that pressure more generally increases bidirectional plasticity, which can both sensitize cells to chemotherapy but can also result in a highly resistant colony of cells.

Dr. Ting Luo and Dr. Homeyra Pourmohammadali were the lab technicians of the Mathematical Medicine Laboratory who collaborated on this project. Dr. Ting Luo completed the *in vitro* experiments, and Dr. Homeyra Pourmohammadali assisted in organizing the *in vitro* results for analysis. All the experimental details are included in the unpublished manuscript but are not included here. The experimental procedures and data will be included in full detail in the final publication. Although other microenvironmental factors have been studied, this is the first time that an experimental-mathematical study has been used to characterize the effect of pressure on mammosphere formation. The manuscript for this project is currently in preparation.

3.1 *In vitro* Experiments

All *in vitro* experiments were completed using the breast cancer cell line, MCF-7. These cells were given as a kind gift from Dr. Aaron Goldman at Harvard Medical School.

3.1.1 Mammosphere formation assay

The first set of experiments were mammosphere formation assays as described in Chapter 2 with the additional factors of pressure and drug. Cells were treated with 0 or 20 nM of docetaxel (Tocris) for 24 hours under normal or high pressure (∼8 kPa) conditions. Pressure conditions were achieved by placing the cell dishes within a pressure chamber that maintained the pressure levels. The pressure chamber with the contained cell dishes was then placed in the incubator for the prescribed time of growth. Cells were then collected and reseeded for mammosphere formation. After staining, colonies were counted using ImageJ [58]. These *in vitro* results are shown in Figure 3.4.

3.1.2 Flow cytometry

Our second set of experiments were flow cytometry experiments as described in Chapter 2. Cells were grown under either normal or pressure (∼8 kPa) conditions for five days, then collected for control conditions or chemotherapy treatment with docetaxel (Tocris) (20 nM) under normal or high pressure. Twenty-four hours later, cells were located and stained with a $CD44^+$ biomarker, CD44-APC (BD Biosciences, Mississauga, ON, Canada), for flow cytometry. These *in vitro* results are shown in Figure 3.4.

3.1.3 Cell cycle

The third set of experiments identified the stage of the cell cycle of the cells under different experimental conditions as shown in Figure 3.1. Cells were treated with 0, 2, or 20 nM docetaxel (Tocris) under normal or high (∼8 kPa) pressure for 24 hours. They were then collected for cell cycle analysis with PI (FluoroPure) flow cytometric analysis [59], which measures the DNA content of a cell. Different stages of the cell cycle have different amounts of DNA as the cell prepares for cell division. Thus, we can classify cells based on the amount of intracellular DNA.

For our *in silico* experiments, we looked specifically at the sub-G1 proportion, representing apoptotic cells, under normal pressure and under high pressure. If a cell has reduced DNA content compared to the G1 phase, i.e. sub-G1, then the cell has lost DNA content and is probably undergoing apoptosis. We found that more cells were in the sub-G1 subpopulation under higher pressure conditions irrespective of the presence of drug. Thus, we expected more cell death in the presence of pressure.

3.1.4 Drug uptake

In our final set of *in vitro* experiments, we tested the drug uptake under all experimental conditions as shown in Figure 3.2. Cells were treated with either 0 or 100 nM DOX (TOCRIS) under normal or high (∼8 kPa) pressure for 24 hours, then collected for flow cytometry (DOX fluorescence). Doxorubicin can be used to test drug uptake due to its inherent fluorescence [60]. Using flow cytometry, the fluorescence intensity for each of the experimental conditions was measured and used as a measurement of drug uptake. Results suggest that cells in the presence of drug undergo increased DOX uptake with or without pressure. Although this test used a different chemotherapy drug, this experiment suggests that pressure does not affect drug uptake. Thus, the effect of pressure is more complex than the exclusion of drug from within cancerous cells. We hypothesized that the effect of pressure is a microenvironmental stress that may induce cells to change their phenotype, changing the intra-tumoural cell dynamics.

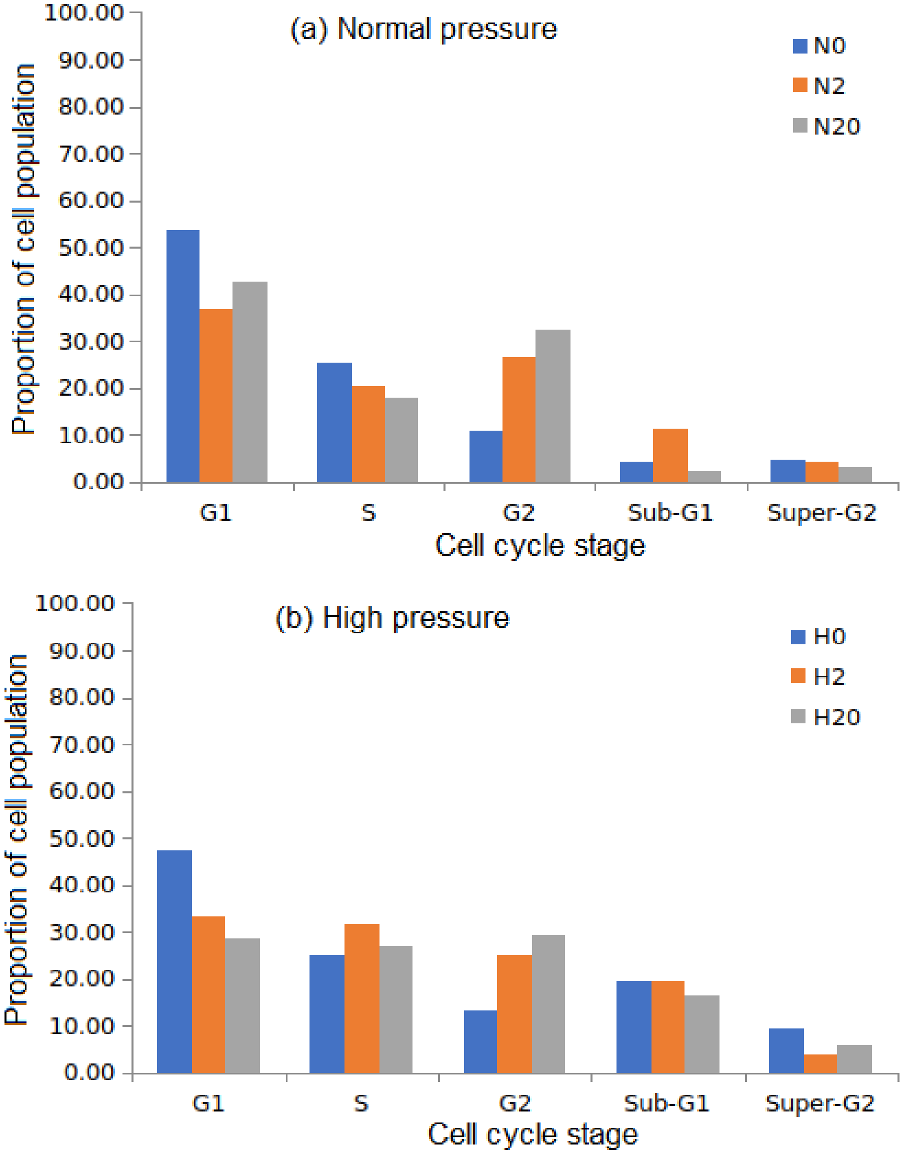

Figure 3.1: PI flow cytometric analysis, as described in Section 3.1.3
(a) for normal pressure conditions and (b) for high pressure conditions. Cells were treated with 0, 2, or 20 nM docetaxel under normal or high (∼8 kPa) pressure for 24 hours. PI flow cytometric analysis was used to classify the cell cycle stage based on the amount of intracellular DNA content of each cell. We found that sub-G1 proportion increases with increased pressure. This data was collected and plotted by Dr. Ting Luo.

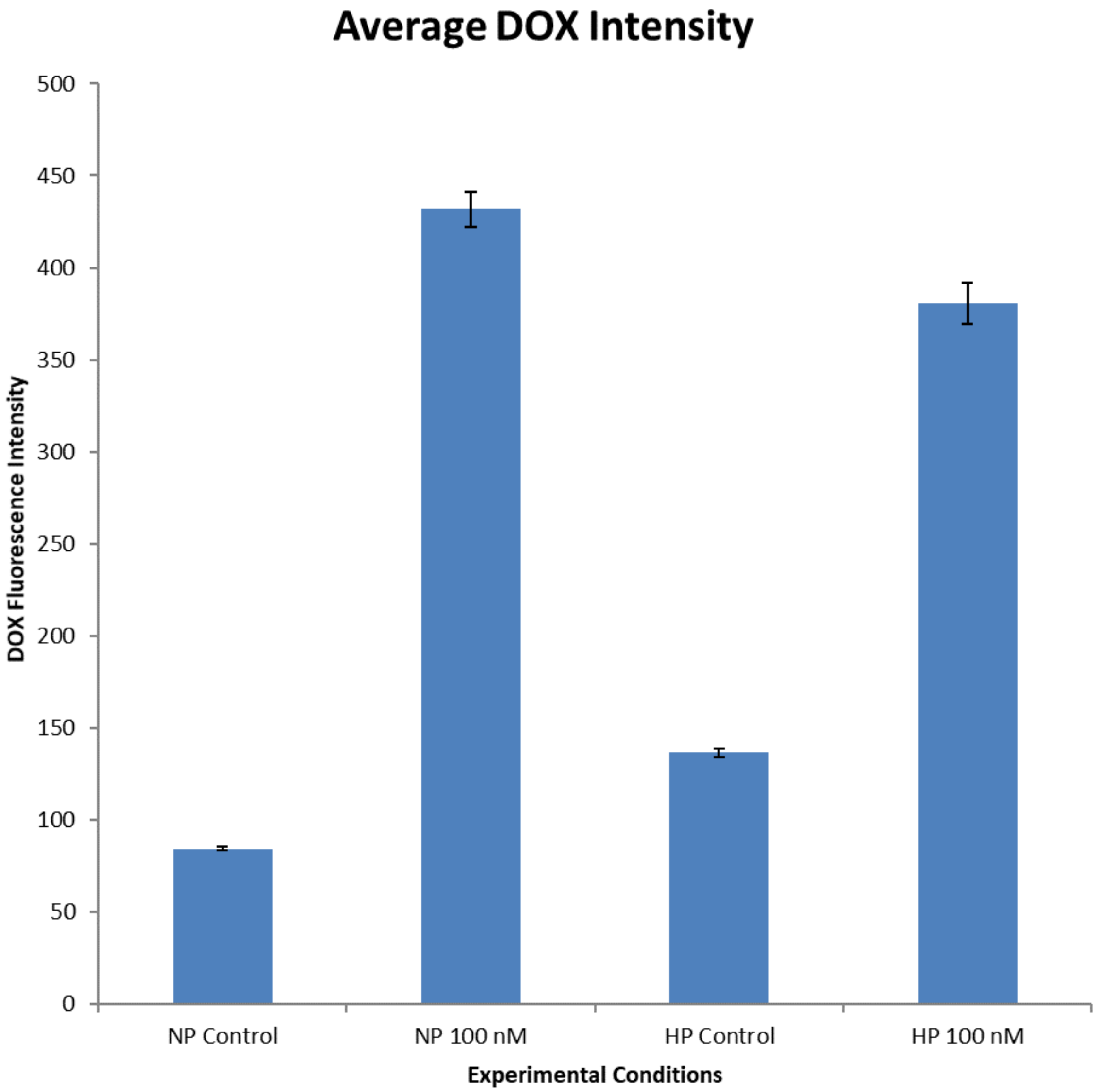

Figure 3.2: Average DOX fluorescence intensity under all experimental conditions. Cells were treated with either 0 or 100 nM doxorubicin under normal or high (∼8 kPa) pressure for 24 hours, then collected for flow cytometry (DOX fluorescence). We found that DOX uptake was unaffected by pressure conditions. This data was collected and plotted by Dr. Ting Luo.

3.2 Mathematical model

3.2.1 Background

As discussed in Chapter 1, CD44$^+$CD24$^-$ cells have been traditionally recognized as the cancer stem cell biomarker for breast cancer cells [17, 21]. Cancer stem cells are cells with tumour-initiating potential and intrinsic drug-resistant characteristics [61]. CD44$^+$CD24$^+$ cells have been identified as cells that are in a transient, drug-resistant state [51]. Together, CD44$^+$ cells mark a subpopulation that can make chemotherapy difficult due to different mechanisms of resistance.

This mathematical model modifies the agent-based model in Chapter 2. The first modification was to simplify the model into a two-compartment model, as discussed in Chapter 1 Section 1.3.2, since binary results are what is most commonly measured *in vitro* with cell surface biomarkers. Note that there are ways of extending to multiple compartments, but this would require additional biomarkers or more bins along the spectrum of biomarker expression. Since the two-compartment model was being incorporated into a spatial framework, we added two additional parameters: probability of migration for positive cells, and probability of migration for negative cells.

This model has eight parameters: (1) probability of spontaneous death for positive and negative cells respectively, (2) probability of proliferation for positive and negative cells respectively, (3) probability of conversion for positive and negative cells respectively, and (4) probability of migration for positive and negative cells respectively. These reactions are summarized in Table 3.1, and a flowchart of the agent-based model algorithm is shown in Figure 3.3.

Variable	Description	Representation
ρ_P	Positive cell division	$S \rightarrow S + S$
α_P	Positive cell death	$S \rightarrow \emptyset$
γ_P	Positive cell conversion	$S \rightarrow P$
m_P	Positive cell migration	-
ρ_N	Negative cell division	$P \rightarrow P + P$
α_N	Negative cell death	$P \rightarrow \emptyset$
γ_N	Negative cell conversion	$P \rightarrow S$
m_N	Negative cell migration	-

Table 3.1: Two-compartment model. S (stem) represents positive cells and P (progenitor) represents negative cells.

3.2.2 Definitions

In order to match our *in silico* experiments to our *in vitro* experiments, we defined a colony or mammosphere to be a collection of cells (starting from a single seeded cell) that reaches a minimum size of 25 cells within 10 days. This definition was used to calculate the colony formation efficiency and the fraction of CD44$^+$ cells in our simulations. Note that this definition differs from the previous chapter (Chapter 2) where we used 12 days of growth to define a mammosphere. The number of days was chosen arbitrarily since we were more interested in the change of parameters as opposed to having an exact measurement of mammosphere formation.

As in Chapter 2, the colony formation efficiency (a.k.a. mammosphere formation efficiency) for a given parameter set is calculated by considering each simulation as the result of a single seeded cell in a colony formation assay. If the simulation is successful in producing a colony as defined above, then we count that as a successful colony. The colony formation efficiency is then defined as the number of successful colonies divided by the total number of simulations completed, representing the total number of seeded cells. In our simulations, we ran each potential parameter set with an ensemble size of 100 and a timestep of one hour to find the best fit to our *in vitro* data.

To calculate the fraction of CD44$^+$ cells, we allow a simulation to either run to 1,000,000 cells or for 100 days, starting from a single cell. We assume that the resulting colony has a sufficient number of cells or has run for a sufficient time for the colonys subpopulation

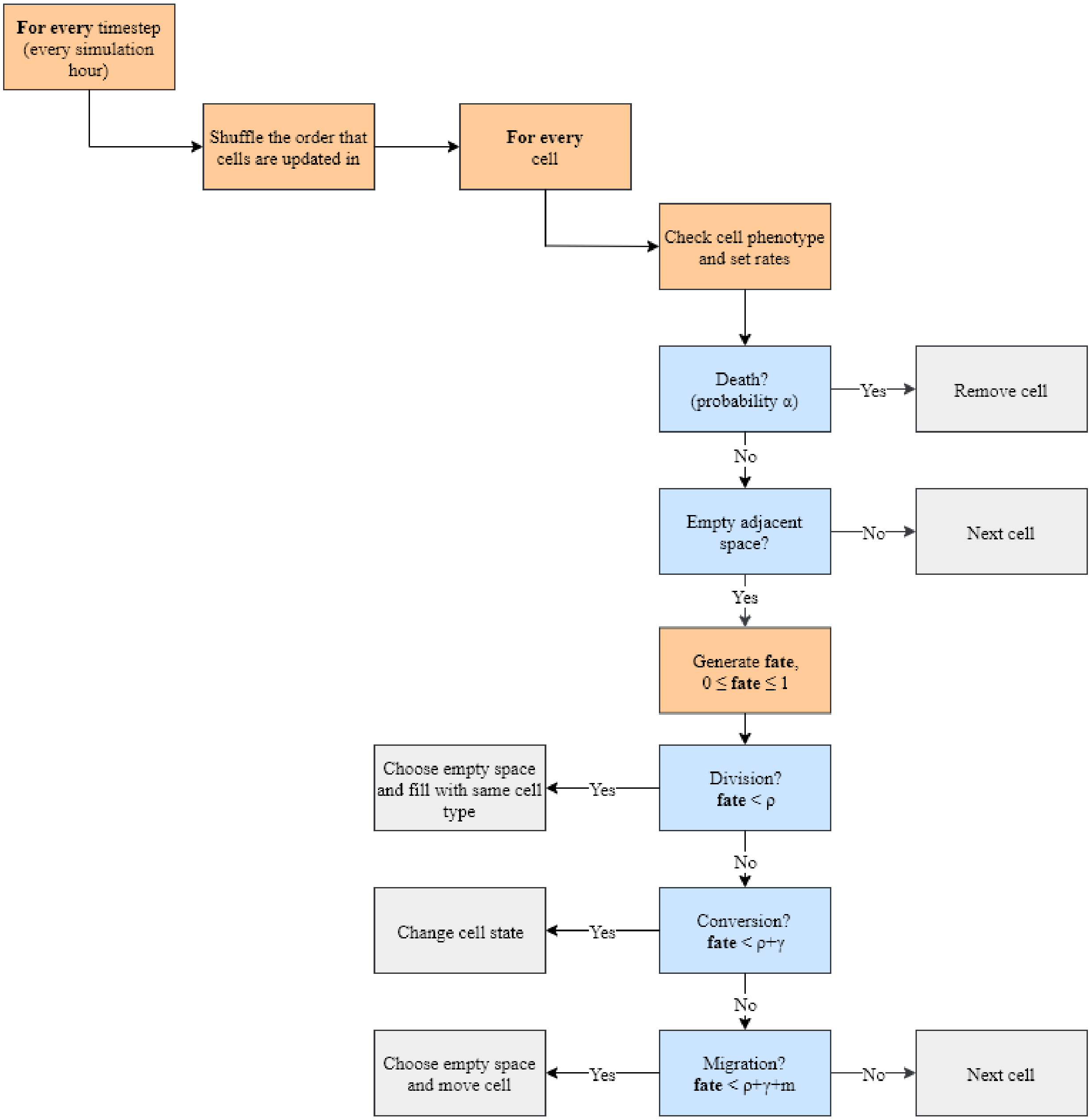

Figure 3.3: Agent-based model flowchart for two-compartment model.

proportions to reach equilibrium. Note that the simulation must run much longer than the time of the *in vitro* experiment because the *in vitro* experiments start with a collection of cells while a simulation starts with a single cell. We then count the number of CD44$^+$ cells and divide by the total number of cells to give us the fraction of CD44$^+$ cells in the colony.

3.2.3 Parameter estimation

Given the above assumptions, the mathematical model had 8 parameters, i.e. 4 parameters for each subpopulation: proliferation, cell death, migration, and conversion. To fit these parameters to the *in vitro* data, we used the genetic algorithm of MATLAB (ga(), with function tolerance of 10^{-15}) to minimize the error between the *in vitro* colony formation efficiency and fraction of CD44$^+$ cells and the *in silico* colony formation efficiency and fraction of CD44$^+$ cells. When calculating the error of each set of parameters, we assigned an error of 0 if the resulting simulated result was within one standard deviation of the *in vitro* data to account for the observed variability in measurements. In other words, we wanted to avoid penalizing results that fell within one standard deviation of the mean since we were uncertain as to the true value of the measurement. Otherwise, we calculated the error as the minimum distance of the *in silico* measurement from ± 1 standard deviation from the *in vitro* data point. The resulting sets of parameters give us some insight into what may be happening to the cellular makeup of the colony in response to pressure and drug exposure.

When fitting the parameters, we made the following additional assumptions. We assumed that all actions were mutually exclusive so that all parameter values for a given cell phenotype (CD44$^+$ or CD44$^-$) summed up to at most 1, allowing for a probability of no action taking place at each timestep (hour). We assumed that the probability of proliferation at every hour would be between 0.01 and 0.03 divisions per hour, for all conditions. The range was given to allow for a cell doubling time between 23 and 70 hours since MCF-7 documentation gives an expected doubling time of 38 hours. For normal conditions, we expected the rate of dedifferentiation, i.e. conversion from a CD44$^-$ cell to a CD44$^+$ cell or - conversion, was between 0.00083 and 0.00167 conversions per hour. These estimates came from a previous study [62], which estimated a conversion rate between 0.02 and 0.04 conversions per day, i.e. 0.00083 and 0.00167 conversions per hour. We also assumed that under the effect of drug or pressure individually, the rate of dedifferentiation and the rate of death for all cells would be greater than those respective rates under normal conditions. We assumed that dedifferentiation would increase under drug and pressure based on previous observations of increased plasticity under adverse conditions [51]. We expected increased death with drug due to its cytotoxic nature. Finally, we assumed increased death with pressure based on the *in vitro* cell cycle experiments as described in Section 3.1.3.

3.3 Results

3.3.1 Parameter sets

The resulting sets of parameters had a mean square error of at least $O(10^{-3})$ and are presented in Figure 3.5. Some of the sets of parameters were more difficult to fit due to the very small colony formation efficiency measured in our *in vitro* experiments (e.g. 0.1% mammosphere formation efficiency). These small colony formation efficiencies are more unstable due to the stochasticity of our mathematical model and since we used ensemble sizes of 100 to fit each condition.

The sets of parameters found had parameter values as shown in the four plots of Figure 3.5. We made the following observations based on these parameter sets. CD44^{-} cells saw increased death in all non-control conditions. CD44^{+} cells saw increased activity (proliferation, death, and migration) with pressure, while CD44^{-} cells saw increased activity (proliferation, death, and migration) with drug. Finally, pressure conditions appear to induce increased bidirectional conversion, i.e. phenotypic plasticity.

3.3.2 Colony simulations

With each set of parameters, we generated a colony by running a simulation for 100 days as in the fraction of CD44^{+} cells *in silico* experiments. Each of the images in Figure 3.6 represents a tumour grown under each of the experimental conditions.

Under control conditions, the resistant, tumour-initiating CD44^{+} cells make up the core of the tumour. The CD44^{+} cells are then surrounded by the more mobile, non-resistant CD44^{-} cells, which spread out and make up the periphery of the tumour.

In the presence of drug (20nM docetaxel), we find that the less resistant CD44^{-} cells respond to treatment and are thus less prevalent within the tumour. The resulting colony

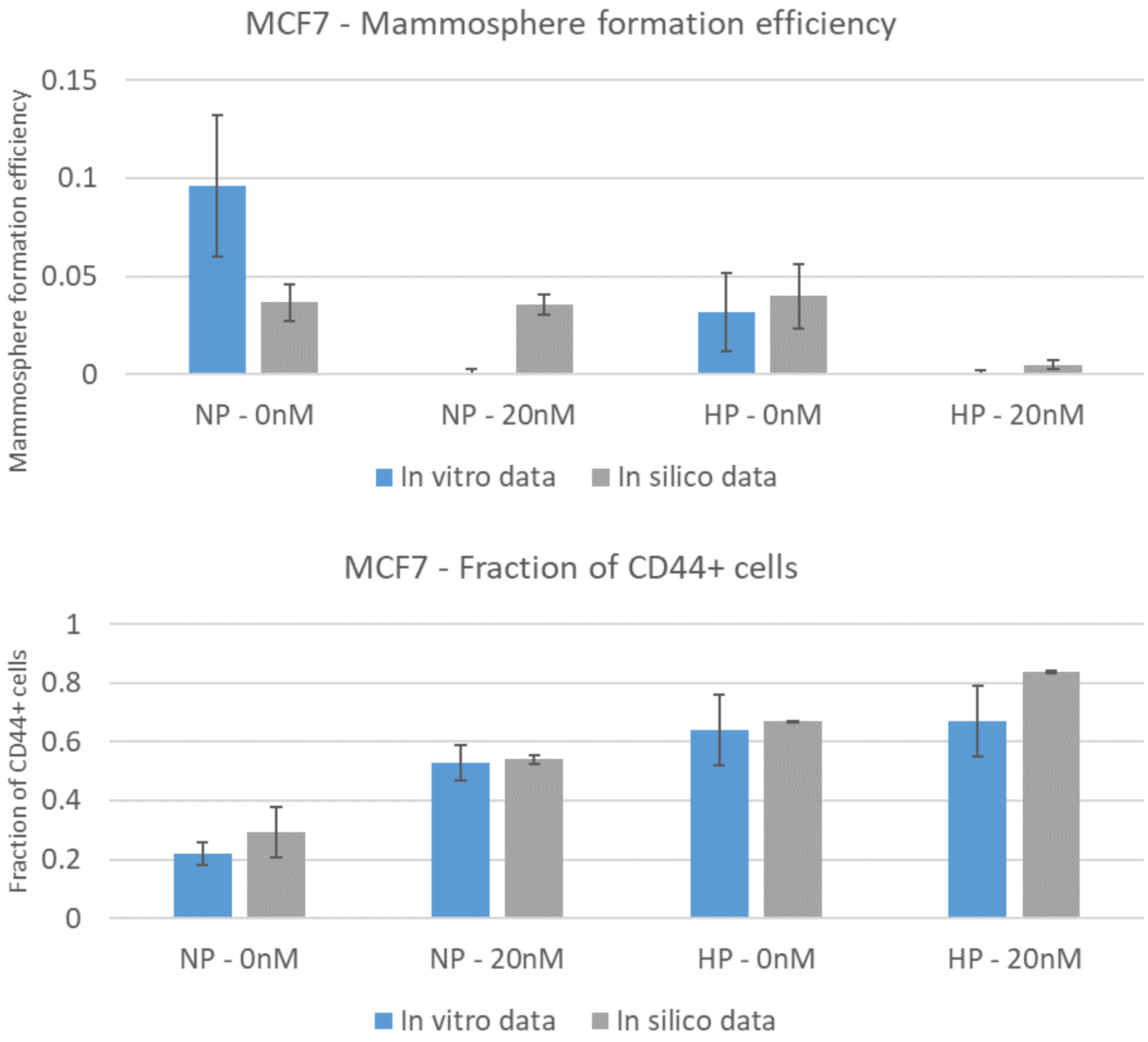

Figure 3.4: Mammosphere formation efficiency and fraction of CD44$^+$ comparison of the *in vitro* results (in blue) and the *in silico* results (in grey), produced through triplicate simulations of the fitted parameter sets (see Figure 3.5) for each of the experimental conditions (normal or high pressure, 0 or 20nM docetaxel). The resulting sets of parameters had a mean square error of at least O(10^{-3}). Error bars show the standard deviation for each of the data points. Note that observed mammosphere formation efficiency values with drug were difficult to fit due to the stochastic nature of the model, the low observed mammosphere formation efficiency values, and the *in silico* ensemble size of 100 simulations.

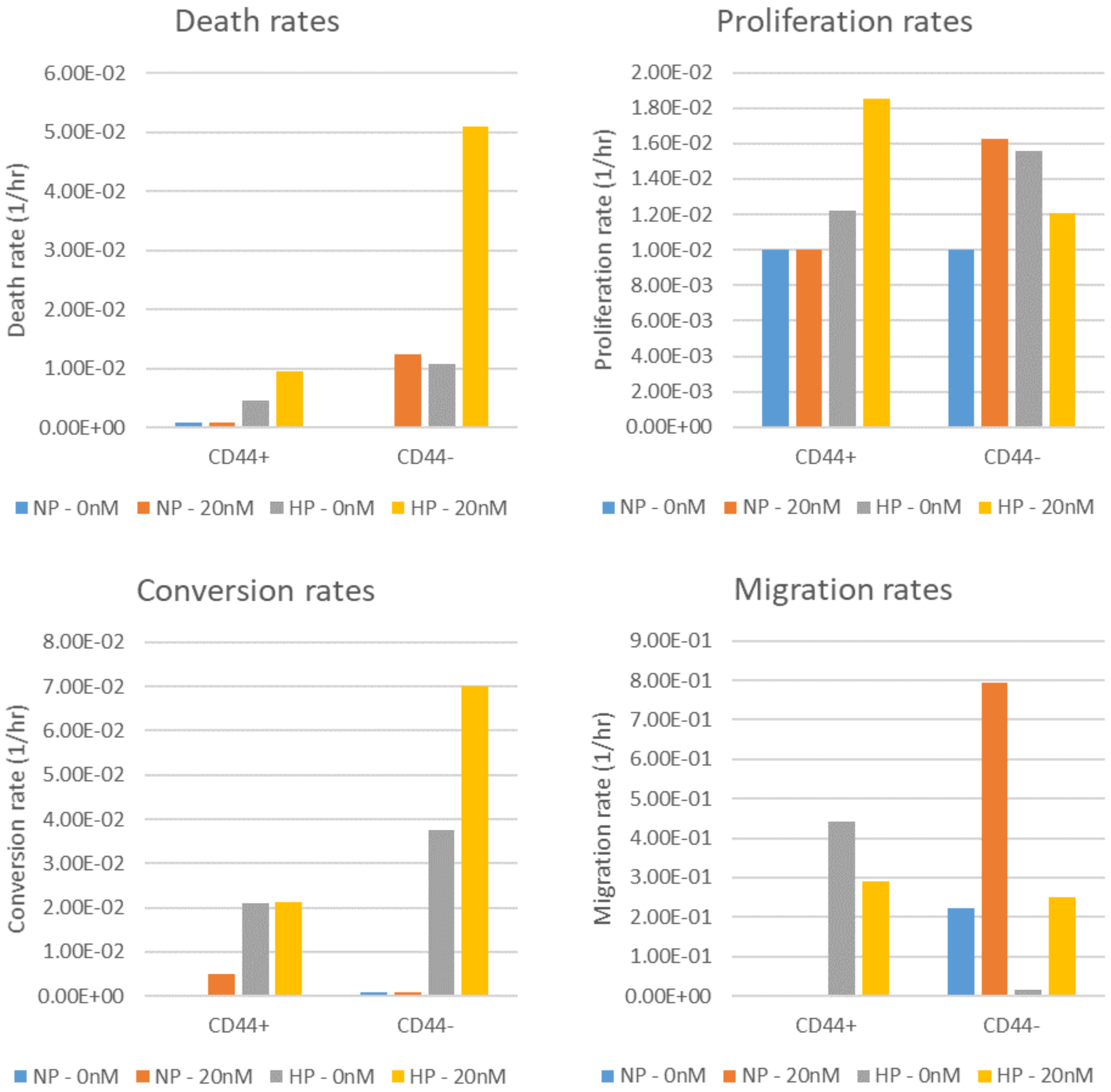

Figure 3.5: Fitted parameter values for all experimental conditions. The genetic algorithm of MATLAB (ga(), with function tolerance of 10^{-15}) was used to minimize the error between the *in vitro* data colony formation efficiency and fraction of CD44^{+} cells and the *in silico* colony formation efficiency and fraction of CD44^{+} cells (see Figure 3.4). These four plots show how each cell behaviour changes under different conditions for both CD44^{+} cells and CD44^{-} cells.

shares the same structure as under normal conditions but is primarily made up of CD44$^+$ resistant and tumour-initiating cells, marking a drug-resistant colony of cancer cells.

Under pressure conditions ($\sim$8 kPa), we see increased plasticity between the two phenotypes (CD44$^+$ and CD44$^-$), resulting in a more homogeneous tumour. CD44$^-$ cells appear to experience increased conversion, resulting in the loss of the periphery of negative cells as in the control conditions. Additionally, CD44$^+$ cells appear to experience increased proliferation, migration, and conversion. This increased activity expands the CD44$^+$ core to the entire tumour. This is evidence that pressure conditions may shift the tumour to a CD44$^+$-dominated tumour.

Finally, we have the combined drug and pressure condition. For this last colony, we see the synergy between the increased plasticity and the CD44$^-$ susceptibility to drug. Thus, our colony of cells consists of less cells, $O(10^4)$, compared to the other conditions, $O(10^5)$ cells. However, the resulting cells are likely very resistant since they have successfully cultured under the stresses of both drug and pressure.

In summary, our *in silico* experiments give evidence that pressure and drug increase cell death for CD44$^-$ cancer cells, i.e. non-resistant cells. However, pressure causes increased activity in CD44$^+$ resistant cancer cells. Pressure also results in increased phenotypic plasticity, which may explain the increased activity in CD44$^+$ cells since they become a more dominant force within the tumour. When pressure and drug conditions are combined, we find synergy between the plasticity induced by pressure and the CD44$^-$ cell-killing induced by drug, resulting in fewer, smaller mammospheres.

3.4 Discussion

In this work, we modified the model from Chapter 2 to characterize the effect of pressure and drug on mammosphere formation. To our knowledge, this is the first study to look at the effect of pressure (with and without a chemotherapy drug) on mammosphere formation.

Our results indicate that pressure conditions may induce increased plasticity in cell phenotype, which can lead to improved response to chemotherapy as observed in the *in vitro* experiments. Note however that if the colony of cancer cells is able to persist in the adverse conditions of pressure and drug, the resulting phenotype would be highly resistant to cell death.

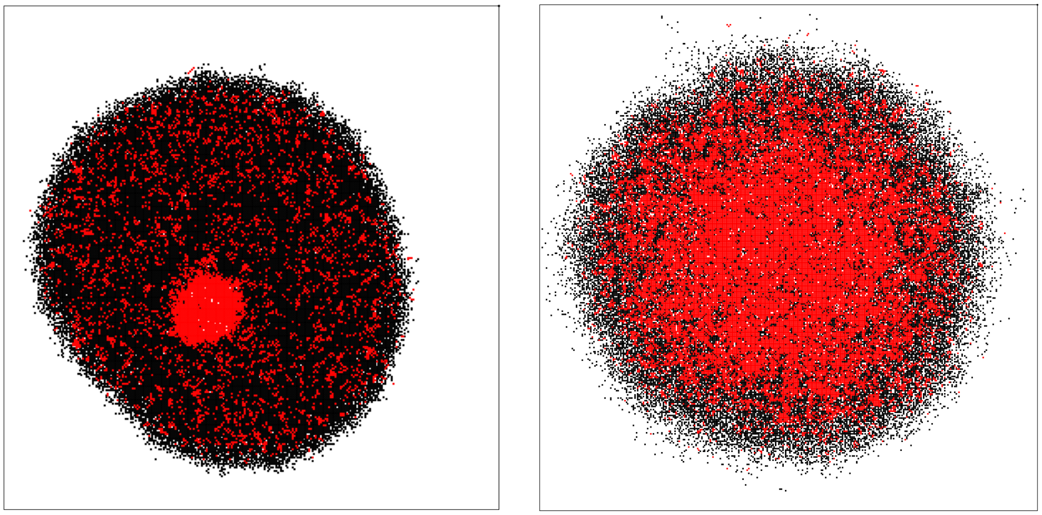

(a) NP - 0nM, 39,533 cells

(b) NP - 20nM, 55,083 cells

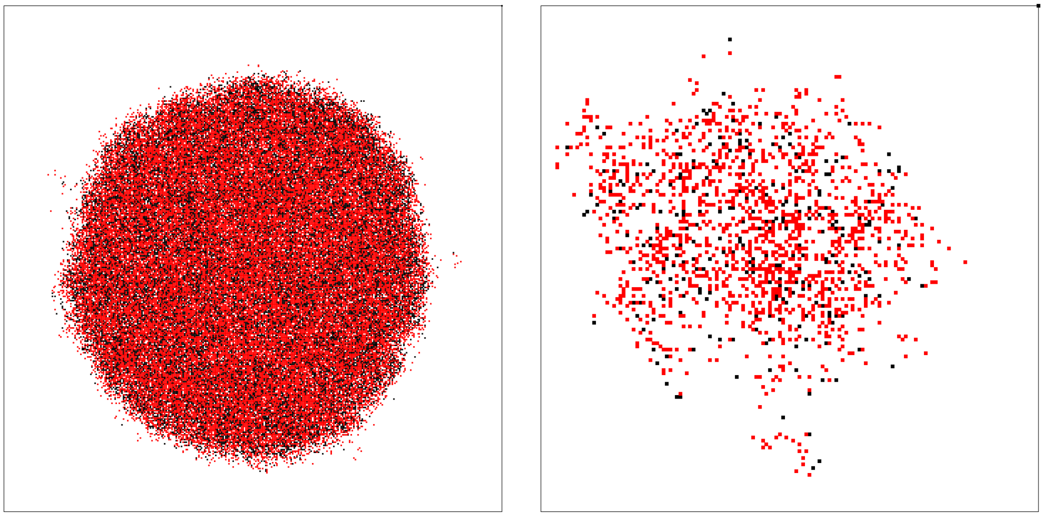

(c) HP - 0nM, 46,852 cells

(d) HP - 20nM, 1,583 cells

Figure 3.6: Tumour simulations under all experimental conditions. Each plot shows a representative tumour after 100 simulated days for one of the experimental conditions (normal or high pressure, 0 or 20nM docetaxel). CD44$^+$ cells are plotted in red and CD44$^-$ cells in black. Each tumour is plotted on its own scale to best show the tumour structure. (a) Control conditions, 39,533 cells. (b) Drug (20nM docetaxel) conditions, 55,083 cells. (c) Pressure (∼8 kPa) conditions, 46,852 cells. (d) Both drug and pressure conditions, 1,583 cells.

Another result of this work is that drug uptake is not affected by high pressure. Docetaxel is a small molecule drug [63] but it is a BCS class IV drug, i.e. a dissolution-limited and permeability-limited drug [64]. However, the results of Figure 3.2 give evidence that pressure on the cells' exterior does not change the uptake of drug. In the case of interstitial fluid pressure, drug is not able to enter the tumour microenvironment to act on the cells [32]. However, these results seem to indicate that the cells still possess the ability to take in drug in the presence of drug. Thus, the reason for less effect in the presence of interstitial fluid pressure must be the inability of drug to penetrate the tumour microenvironment as opposed to the inability of the drug to penetrate the cell.

3.4.1 Limitations of the model

As in chapter 2, one limitation of the model is our choice of initial conditions. In the corresponding *in vitro* mammosphere formation assay experiment that we are trying to recreate, the type of cell to be considered is unknown. In other words, we have no information about the initial conditions of the *in silico* experiment. We thus assume that every simulation begins with a cancer stem cell, which is unlikely to be the case in reality. Alternatively, we could randomly set the initial conditions to a random type of cell, but then we would need to make assumptions about the frequencies of each cell type. To avoid the effect of this assumed distribution, we set the initial condition as a single cancer stem cell.

One spatial assumption of the model that was adopted from previous work is that cells that are completely surrounded by other cells cannot proliferate, move, or dedifferentiate. In reality, space is not necessary for dedifferentiation since it reflects either a mutation or an epigenetic change in gene expression. It may be more biologically realistic to allow for dedifferentiation in the absence of space since quiescent cells continue to mutate [54].

3.4.2 Future work

Future work with this framework includes improving the identification of cellular behaviours by using sensitivity and uncertainty analyses, introducing spatial heterogeneity in modelling pressure, distinguishing between different forms of division for CSCs, extending the model to a three-compartment model of EMT, and investigating combination therapy within a spatial context.

Local sensitivity analysis identifies the influential parameters in the tumour's response to the tumour microenvironment [41]. Uncertainty analysis could be used to evaluate our parameter estimates by calculating the confidence intervals for each parameter. Thus, we can evaluate the probability that our set of parameters is an accurate description of the tumour's phenotypic state in response to the microenvironment [55].

One simplification of this experimental setup is the homogeneous effect of pressure in the *in vitro* microenvironment. In reality, the effect of pressure on a tumour would be heterogeneous due to the presence of normal cells, other structures (e.g. bones, blood vessels, organs) and intracellular fluid [3]. However, in the early stage of mammosphere formation, the effect of pressure may be homogeneous due to the small area that the mammosphere takes up within the body.

A more realistic implementation of pressure would allow for heterogeneity. This can be difficult to manipulate and control in an *in vitro* setting; however, an *in silico* model could be more easily constructed since we can observe and manipulate the pressure conditions at each grid point of the spatial model. A tumour microenvironment could first be placed (randomly or by design) onto the computational space in which the cells grow. Then, the cells would choose their parameters based on their location and the surrounding microenvironment. The microenvironment could then be updated given the presence or absence of cells in the neighbourhood of a given grid point. An alternative way of incorporating heterogeneous pressure in the model is to overlay the agent-based model with a continuous partial differential equation for pressure as mentioned in Chapter 2. This *in silico* extension of the model would allow researchers to perform *in silico* studies of a heterogeneous tumour microenvironment without having to work with more complex *in vitro* apparatuses.

One simplification of the mathematical model framework is in using the two-compartment model. The CSC hypothesis assumes that there exists different forms of division for CSCs: symmetric self-renewal, asymmetric self-renewal, and symmetric differentiation. The two-compartment model captures these phenomena as a series of reactions. Our *in silico* experiments give evidence that pressure increases CSC or positive cell activity, including positive conversion to negative cells. However, it is not clear as to which form of division positive cells are using to increase the negative cell population, i.e. symmetric differentiation and asymmetric self-renewal. In the former case, cells are losing their stem cell phenotype and in the latter case, positive cells are maintaining their subpopulation within the tumour. Investigating this phenomena more closely can distinguish between the two reactions to the pressure environment.

Another possible extension of this model is to extend the two-compartment model into a three-compartment model. As discussed in Chapter 1, epithelial-mesenchymal transition is an important mechanism during the process of cancer metastasis but also in other stages of tumour development [24,25]. It is a mechanism of phenotypic plasticity, and the hybrid epithelial-mesenchymal state between the two extremes is currently an area of study within mathematical oncology [26]. A three-compartment extension of this model could be used to study the effect of pressure on epithelial-mesenchymal transition and it may provide insight into the role that these hybrid cells play in tumour development. In other words, this *in silico* model could be used to answer questions in the epithelial-mesenchymal research area, such as 'what role do cells in the hybrid epithelial-mesenchymal state play in cellular growth dynamics during mammosphere formation?'.

Another possible extension is to consider different single and combined treatment strategies, taking into account the response of each population to a given drug. For example, it is well known that CSCs are more resistant to standard chemotherapy drugs, so this heterogeneity can be included in the model [15]. There are also novel treatment strategies that target dedifferentiation of cells [65]. Finally, some of the drugs can affect the tumour microenvironment (such as anti-angiogenic treatment) [66]. Our model can be used *in silico* to design efficient combinations of these drugs.

Chapter 4

In silico experiments of an Hsp90 chemical reaction network

In this chapter, we identify the Hsp90 protein network as a means by which drug resistance can be overcome in a DTC. Since Hsp90 expression is increased in cancer cells that are resistant to docetaxel, we hypothesized that an Hsp90-inhibitor such as radicicol could be used to overcome the acquired drug resistance to docetaxel. Thus, we constructed a minimal *in silico* model of this network using a systems biology approach to design a treatment schedule for docetaxel and radicicol. Additionally, we hypothesized that a nanoparticle administration would be a more effective drug vehicle compared to a free drug administration due to the different timescales in which drug would be released into the tumour microenvironment. Finally, we used the *in silico* model to identify the most effective improvements that could be made to the drugs in order to improve the efficacy of the treatment sequence.

For this project, we collaborated with Dr. Aaron Goldman and his team. They provided the *in vitro* protein expression data used in fitting the mathematical models. All the experimental details are included in the unpublished manuscript but are not included here. The experimental procedures and data will be included in full detail in the final publication. This study identified a novel treatment sequence that could overcome drug resistance through the Hsp90 pathway. The work in this chapter has recently been submitted for publication.

4.1 Biological background

In developing our *in silico* model, we first researched several key prosurvival proteins (Hsp90, Src, ERK, STAT3, and Akt). In the literature, there has been evidence to suggest that each of the previously listed survival proteins promotes cell survival. These prosurvival proteins are then related and used in the construction of a minimal Hsp90 chemical reaction network.

4.1.1 Key proteins

Heat shock protein 90 (Hsp90) is the most abundant chaperone protein in human cells [67]. In normal healthy cells, it maintains homeostasis and ensures proper folding of a range of key (but often oncogenic) proteins [68,69]. One of its important functions is the regulation of apoptosis, which is accomplished by regulating proteins necessary for caspase activation [69, 70]. In cancerous cells, Hsp90 regulates the abnormal functions of mutated cells to prevent apoptosis and supports other cancerous properties (e.g. growth, survival, and infinite replicative potential) [70]. In other words, Hsp90 protects cancer cells from various oncogenic and microenvironmental stresses so that cell survival is enhanced [67,69].

Src is a regulatory protein that plays a key role in cell differentiation, motility, proliferation, and survival. There has also been evidence that abnormal Src activity induces anchorage-independent growth [71]. The c-Src proto-oncogene plays a major role in the development, growth, progression, and metastasis of a wide variety of human cancers. Inversely, Src inhibition is correlated with antiproliferative activity [72].

ERK is a protein kinase that controls cell cycle progression by regulating signal transduction from the cell surface to the nucleus. More specifically, ERK1/2 and ERK5 signaling pathways are responsible for cell proliferation and differentiation [68]. Through the activation of ERK1/2, cells accomplish important functions such as entry and progression through the G2/M phase, normal microtubular function, and proper functioning of the mitotic spindle apparatus. In cancer, the activation of ERK1/2 results in a cytoprotective effect [73].

STAT3 is a transcription factor that is required for cell maintenance and development in both normal and disease phenotypes [74]. The STAT3 signaling pathway is a crucial cell survival pathway that inhibits cell apoptosis [75]. More generally, malfunctioning in STAT3 is associated with oncogenesis and immune disorders [74].

Akt is a protein kinase that regulates cell signaling pathways that suppress cell death [76] and promote cell survival, resistance, cell growth [70], proliferation [76, 77], energy metabolism [76], and motility [78]. Akt also promotes anchorage-independent growth, which is a characteristic of cancerous cells [70].

4.1.2 Key interactions

Based on the literature, Hsp90 plays a key role in promoting Src, ERK, and Akt activity. Hsp90 modulates Src activity, specifically the transportation of Src into the plasma membrane where Src is activated [79]. Hsp90 indirectly regulates ERK activity, and Hsp90 inhibition results in a decrease of activated ERK through the Raf-MEK-ERK pathway [68]. Finally, Hsp90 supports and regulates Akt activation as part of its function of apoptosis regulation [67]. In our model, we consider these reactions by having Hsp90 activate Src, ERK, and Akt.

Src plays a key role in activating ERK, STAT3, and Akt activity. Src kinase is an activator of ERK since it modulates growth factor-induced activation of the MAPK cascade [80]. Src directly binds with STAT3, leading to phosphorylation and activation of STAT3 [81], in the cellular processes of cell growth [82]. It has also been shown that STAT3 inhibition is associated with decreased Src activation [83]. Src is an activating kinase upstream of Akt [84], and inhibition of Src signaling results in decreased Akt [83]. In our model, we consider these reactions by having Src activate ERK, STAT3, and Akt.

ERK activates STAT3, and STAT3 may mediate ERK activation through cytokines [75]. In our model, we include this by having ERK and STAT3 activate each other. Also, STAT3 activation contributes to Akt phosphorylation, and STAT3 inhibition results in less Akt activity [85]. In our model, we include this by having STAT3 activate Akt. Since Hsp90, ERK, STAT3, and Akt are prosurvival proteins, we have each of these proteins inhibiting Caspase-3 in our model. In addition, an increase in Caspase-3 has been observed with a decrease in Akt levels [70], so our model includes Caspase-3 inhibiting Akt.

4.1.3 Drug effects

The drugs under consideration are a cytotoxic drug, docetaxel, and an Hsp90-inhibitor, radicicol. Docetaxel is a drug that induces microtubular stabilization, which leads to cell cycle arrest in G2/M phase and eventually apoptosis. When docetaxel is administered, it results in an activation of ERK and Akt (unless an ERK-inhibitor is administered simultaneously). Moreover, reducing ERK through ERK inhibitors enhances cytotoxicity by docetaxel [73]. Inhibiting Akt also enhances the apoptotic effect of chemotherapy [70]. In the case of a cell that has survived docetaxel treatment, Hsp90 is also increased since increased drug resistance is associated with increased expression of Hsp90 [86]. Additionally, we assumed that docetaxel shifted the cell phenotype from a drug-naive state to a drug-tolerant state by sensitizing the cell to the Hsp90 survival pathway. In other words, we assume that the mechanism for drug resistance is an adaptation to the increased Hsp90 levels.

Radicicol was one of the first drugs used to identify Hsp90 as a drug target. It works through Hsp90-inhibition, which has an antiproliferative effect and results in cell death in cancer cells but not normal cells [69]. Since Hsp90 regulates many critical proteins, Hsp90 inhibition has the potential to inhibit a range of critical cancer pathways, leading to the degradation of survival proteins [68]. This works through the intrinsic apoptotic pathway (Caspase-9 - Caspase-3 pathway). More specifically, Hsp90 inhibition results in an increase in Caspase-3 and Caspase-7 and decreases Akt, all of which stop the growth of cells and increase apoptosis [70]. Hsp90 inhibition also results in a decrease of activated ERK (but not on total ERK levels) through the Raf-MEK-ERK pathway [68]. These results reiterate that Hsp90 activates ERK and Akt.

4.2 Mathematical model

4.2.1 Model construction

Using a systems biology approach, we constructed a minimal chemical reaction network based on the aforementioned proteins, interactions, and drug effects [38]. Each protein can exist in an active or inactive state, usually corresponding to phosphorylated and dephosphorylated states. However, to reduce the complexity of the model, each protein is normalized and modelled only in its activated state. We assume that the level of activated protein can be used as a proxy for the level of inactivated protein. We also assume that all proteins and drugs are well-mixed within the system, so that the spatial component is negligible.

It is assumed that each protein has constant "production" and exponential decay, in addition to its specific interactions with other proteins and drugs, as illustrated in Figure

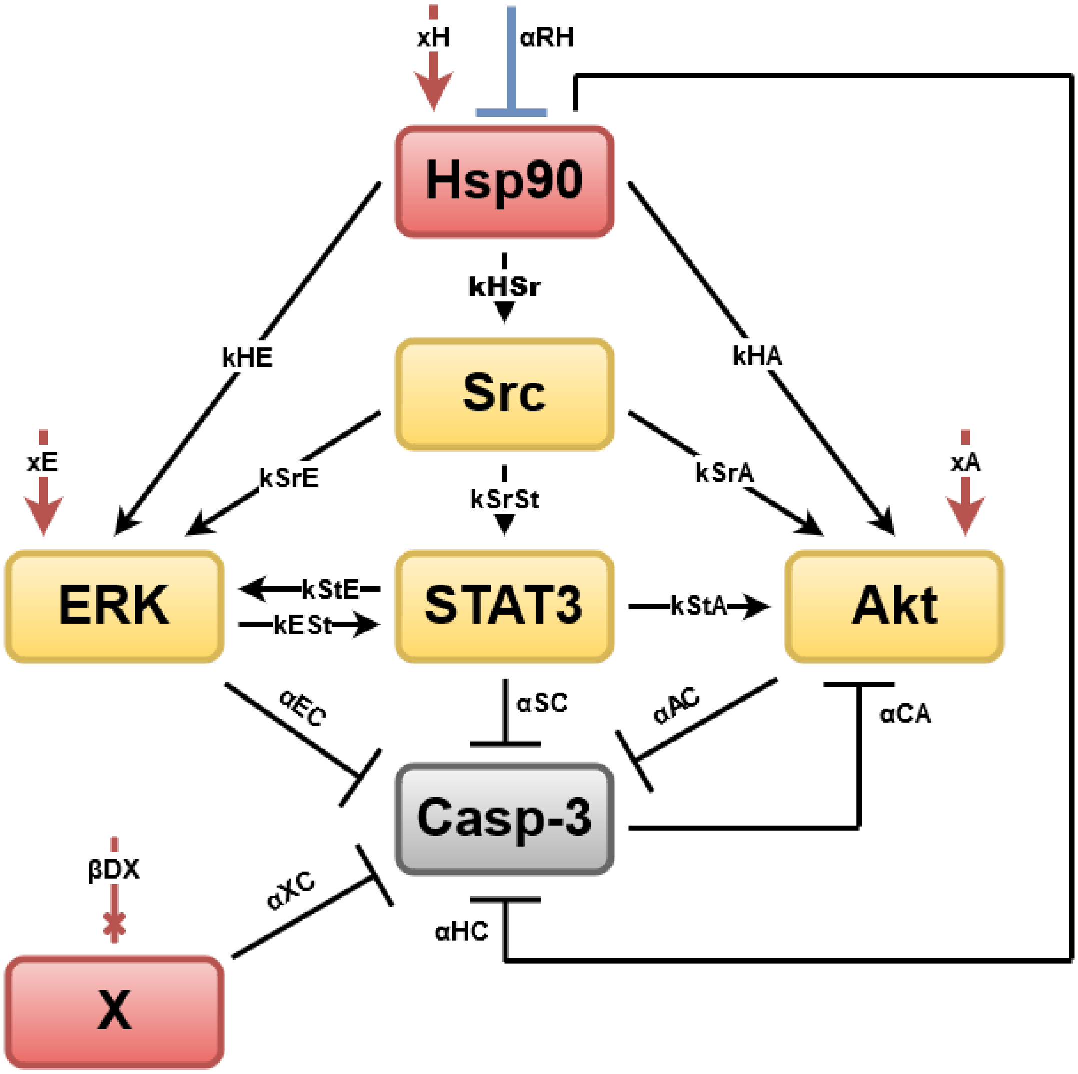

Figure 4.1: Hsp90 chemical reaction network with the effect of drug. Arrows show an activation relationship and block-headed arrows show an inhibiting relationship. X-headed arrows show a removal process. Normal processes in the absence of drug are shown in black, docetaxel activity is shown in red, and radicicol activity is shown in blue. The corresponding parameters are shown for each reaction.

4.1. Production is meant to represent a background level of activation for each of the proteins due to cellular processes other than the activation interactions explicitly included in our model. Activation rates of proteins are assumed to be dependent on the amount of inactivated protein available as well as the amount of activator protein available. As stated earlier, we excluded inactivated states of each of our proteins to reduce the number of considered species and to limit the number of model parameters. Instead, we assumed that the amount of activated protein could serve as a proxy for the amount of inactivated protein. Thus, the activation rates of each of the proteins are assumed to be dependent on the amount of activated protein available as well as the amount of activator protein available. Inhibition by proteins is dependent only on the amount of (inhibiting) protein available. Finally, it is assumed that protein levels are at equilibrium in untreated cells.

To model the drug dynamics, we assumed that the uptake rate of drug into a cell is constant. The drug is then metabolized and removed from within the cell, leading to exponential decay. This convention neglects removal of the drug from the microenvironment, thus assuming that the external drug concentration is constant, which would be the case in a saturated *in vitro* environment. It is assumed that the drug is only in the cells microenvironment for a finite amount of time, beginning with t_{start} and ending with t_{end}. These drug equations are presented in Equations 4.10 - 4.11.

Equations 4.10 - 4.11 correspond to the *in vitro* experiments where drug is introduced into the cell microenvironment and then washed out after a specified amount of time (e.g. two days). Once the drug was washed out, it was no longer in the cell microenvironment and ceased to enter the cell. As illustrated in the chemical reaction network (Figure 4.1) we assume that docetaxel activates Hsp90, ERK, and Akt and that radicicol inhibits Hsp90. We assume that the activation/inhibition rate is dependent only on the amount of drug available in the cell. In other words, we assume that the increased activation of drug increases the background activation of Hsp90, ERK, and Akt.

As stated earlier (Section 4.1.3), we assumed docetaxel causes cells to become solely dependent on the Hsp90-dependent chemical network for survival. In other words, we assumed that docetaxel shifted the cell phenotype from a drug-naive state to a drug-tolerant state. We assumed that this change in cell phenotype from drug-naive to drug-tolerant state is due to a sensitization of the cell to Hsp90 protein survival network. In the modelling process, we found that the model with only proteins and drug components was not able to capture any drug synergy.

To capture the change in cell phenotype, an additional species, X, was included in the model to represent the other survival and anti-apoptotic pathways that are independent of the Hsp90-dependent network. This species, X, is assumed to be constant at a normalized steady state value of one in the drug-naive state. As docetaxel sensitizes the cell, X is removed from the network since it is no longer relevant or necessary for the cells survival. The removal of the X species represents the shift of the cell from a drug-naive to a drug-tolerant state. We assume that the cell does not return to a drug-naive state within the timescale of our experiments, so we do not model the return to a drug-naive state.

These reaction rates were used to construct a system of ordinary differential equations representing the protein and drug dynamics. The naming conventions for the model parameters are as follows: b_{protein} for "production" constants into the activated state, b_{protein2} for inhibition constants, d_{protein} for decay constants, $k_{\text{reacting protein -activated protein}}$ for reaction constants, $\alpha_{\text{reacting protein -inhibited protein}}$ for inhibition constants, x_{protein} for activation by docetaxel, and $\beta_{\text{reacting protein -inhibited protein}}$ for removal of protein from the model. The time evolution of the proteins in the network are described by Equations 4.1 - 4.9.

With regards to the effect of the drug on the chemical reaction network, we made the following assumptions: a) the initial population of cells are in a drug-naive state; b) as the cells move through the treatment, DTC are present which are a mixture of intrinsically resistant cells and cells that have acquired resistance; c) cells in the presence of drug are not proliferating due to stress; d) docetaxel activates Hsp90, ERK and Akt; e) docetaxel-treated cells become more dependent on the Hsp90 prosurvival pathway; and f) radicicol inhibits the activation of Hsp90.

4.2.2 Model equations

Heat shock protein 90 (Hsp90)

$$\frac{d[Hsp90]}{dt} = \frac{b_{H1} + x_H[Doc]}{b_{H2} + \alpha_{RH}[Rad]} - d_H[Hsp90] \tag{4.1}$$

We assume that Hsp90 has background activation from cell processes that are not explicitly included in the model. We assume that this background activation is increased by the presence of docetaxel within the cell [86]. We also assume that all Hsp90 activation is inhibited by the presence of radicicol within the cell (first term) [69]. We assume that Hsp90 undergoes exponential decay (second term).

Src

$$\frac{d[Src]}{dt} = b_{Sr} + k_{HSr}[Hsp90][Src] - d_{Sr}[Src] \tag{4.2}$$

We assume that Src has background activation from cell processes that are not explicitly included in the model. We assume that the presence of Hsp90 results in activation of Src and that this activation is dependent on both the amount of Hsp90 and the amount of activated Src within the cell (second term) [79]. We assume that Src undergoes exponential decay (third term).

ERK

$$\begin{align}\frac{d[ERK]}{dt} = b_E + x_E[Doc] + k_{HE}[Hsp90][ERK] + k_{SrE}[Src][ERK] \tag{4.3}\\ + k_{StE}[STAT3][ERK] - d_E[ERK] \tag{4.4}\end{align}$$

We assume that ERK has background activation from cell processes that are not explicitly included in the model (first term). We assume that this background activation is increased by the presence of docetaxel within the cell (second term) [73]. We assume that the presence of Hsp90 results in activation of ERK and that this activation is dependent on both the amount of Hsp90 and the amount of activated ERK within the cell (third term) [68]. We assume similar interactions for Src (fourth term) [80] and STAT3 (fifth term) [75] respectively. We assume that ERK undergoes exponential decay (sixth term).

STAT3

$$\frac{d[STAT3]}{dt} = b_{St} + k_{SrSt}[Src][STAT3] + k_{ESt}[ERK][STAT3] - d_{St}[STAT3] \tag{4.5}$$

We assume that STAT3 has background activation from cell processes that are not explicitly included in the model (first term). We assume that the presence of Src results in activation of STAT3 and that this activation is dependent on both the amount of Src and the amount of STAT3 within the cell (second term) [81, 82]. We assume a similar interaction for ERK (third term) [75]. We assume that STAT3 undergoes exponential decay (fourth term).

Akt

$$\frac{d[Akt]}{dt} = \frac{b_{A1} + x_A[Doc]}{b_{A2} + \alpha_{CA}[Casp3]} + k_{HA}[Hsp90][Akt] + k_{SrA}[Src][Akt] + k_{StA}[STAT3][Akt] - d_A[Akt] \tag{4.6}$$

We assume that Akt has background activation from cell processes that are not explicitly included in the model. We assume that this background activation is increased by the presence of docetaxel within the cell [73]. We also assume that all Akt activation is inhibited by the presence of Caspase-3 within the cell (first term) [70]. We assume that the presence of Hsp90 results in activation of Akt and that this activation is dependent on both the amount of Hsp90 and the amount of Akt within the cell (second term) [67]. We assume similar interactions for Src (third term) [84] and STAT3 (fourth term) [85]. We assume that Akt undergoes exponential decay (fifth term).

Caspase-3 (Casp3)

$$\frac{d[Casp3]}{dt} = \frac{b_{C1}}{b_{C2} + \alpha_{HC}[Hsp90] + \alpha_{EC}[ERK] + \alpha_{StC}[STAT3] + \alpha_{AC}[Akt] + \alpha_{XC}[X]} \tag{4.7}$$

$$- d_C[Casp3] \tag{4.8}$$

We assume that Caspase-3 has background activation from cell processes that are not explicitly included in the model. We assume that this activation is inhibited by the presence of the following prosurvival proteins in the model (line one): Hsp90 [67,69,70], ERK [68,73], STAT3 [75], Akt [76], and X. We assume that Caspase-3 undergoes exponential decay (line two).

Other survival pathways (X)

$$\frac{d[X]}{dt} = -\beta_{DX}[X][Doc] \tag{4.9}$$

We assume that there are other survival and anti-apoptotic pathways that contribute to an untreated cell's survival and are independent of the Hsp90 protein network. This species is assumed to be constant at a normalized steady state value of one in the drug-naive state. Once docetaxel is introduced into the cell, this species is removed from the network since it is no longer relevant or necessary for the cell's survival.

Docetaxel (Doc)

$$\begin{aligned} \frac{d[Doc]}{dt} &= b_D(t) - d_D[Doc] \\ b_D(t) &= \begin{cases} b_D & t_{\text{start}} \leq t \leq t_{\text{end}} \\ 0 & \text{otherwise} \end{cases} \end{aligned} \tag{4.10}$$

We assume that docetaxel undergoes constant uptake into the cell (first term) and exponential decay within the cell (second term). We assume that docetaxel is being taken into the cell only when it is in the cell microenvironment, i.e. $t_{\text{start}} \leq t \leq t_{\text{end}}$. Note that each drug will have its own t_{start} and t_{end}.

Radicicol (Rad)

$$\frac{d[Rad]}{dt} = b_R(t) - d_R[Rad] \tag{4.11}$$

$$b_R(t) = \begin{cases} b_R & t_{\text{start}} \leq t \leq t_{\text{end}} \\ 0 & \text{otherwise} \end{cases}$$

We assume that radicicol undergoes constant uptake into the cell (first term) and exponential decay within the cell (second term). We assume that radicicol is being taken into the cell only when it is in the cell microenvironment, i.e. $t_{\text{start}} \leq t \leq t_{\text{end}}$. Note that each drug will have its own t_{start} and t_{end}.

4.2.3 Parameter estimation

To fit the model parameters, our collaborators collected data from a docetaxel-radicicol treatment sequence. In their experimental setup, they exposed cells in an assay to 48 hours of docetaxel, followed by drug washout, then 48 hours of radicicol. They collected Western blot data for the proteins HCK, phosphorylated ERK, phosphorylated STAT3, and phosphorylated mTOR at $t = 48$ hours and $t = 96$ hours. HCK was used as a proxy for phosphorylated SRC levels, and phosphorylated mTOR was used as a proxy for phosphorylated Akt levels. With the model, the genetic algorithm [39] in MATLAB was used to explore the multi-dimensional parameter space to find a local minimum for the error between the simulation results and the normalized quantification of the Western blots from the docetaxel-radicicol treatment sequence. The fitted parameters are shown in Table 4.1.

Given the large parameter space, the following constraints were used to limit the algorithm to relevant parameter possibilities: a) parameters must be strictly positive so that every reaction is accounted for in the model; b) the network is at equilibrium in a drug-naive cell, i.e. in the absence of drug, resulting in the constraints given in Equations 4.12 - 4.17 corresponding to Equations 4.1 - 4.7 respectively (calculated by setting the derivatives to zero with all normalized protein levels equal to one and all drug levels equal to zero); c) drug decay rates must be sufficiently slow to ensure that there is still drug present in the cell for at least 12 hours after drug washout; d) drug decay rates must be sufficiently fast to

#	Name	Parameter Description	Units	Value
1	b_{H2}	Inhibition scaling constant for Hsp90	-	8.54
2	b_{A2}	Inhibition scaling constant for Akt	-	15.93
3	b_{C2}	Inhibition scaling constant for Caspase-3	-	0.19
4	b_D	Intake rate of docetaxel	mol/hr	2.06
5	b_R	Intake rate of radicicol	mol/hr	1
6	d_H	Decay rate of Hsp90	hr^{-1}	1.28
7	d_{Sr}	Decay rate of Src	hr^{-1}	1.26
8	d_E	Decay rate of ERK	hr^{-1}	16.69
9	d_{St}	Decay rate of STAT3	hr^{-1}	2.87
10	d_A	Decay rate of Akt	hr^{-1}	17.61
11	d_C	Decay rate of Caspase-3	hr^{-1}	7.7
12	d_D	Decay rate of docetaxel	hr^{-1}	0.20
13	d_R	Decay rate of radicicol	hr^{-1}	0.26
14	k_{HE}	Activation rate of ERK by Hsp90	hr^{-1}	1.6
15	k_{HSr}	Activation rate of Src by Hsp90	hr^{-1}	0.35
16	k_{HA}	Activation rate of Akt by Hsp90	hr^{-1}	1.36
17	k_{SrE}	Activation rate of ERK by Src	hr^{-1}	0.53
18	k_{SrSt}	Activation rate of STAT3 by Src	hr^{-1}	1.00e-6
19	k_{SrA}	Activation rate of Akt by Src	hr^{-1}	0.85
20	k_{ESt}	Activation rate of STAT3 by ERK	hr^{-1}	1
21	k_{StE}	Activation rate of ERK by STAT3	hr^{-1}	1.08
22	k_{StA}	Activation rate of Akt by STAT3	hr^{-1}	0.07
23	α_{HC}	Inhibition strength of Hsp90 on Caspase-3	-	6.43
24	α_{EC}	Inhibition strength of ERK on Caspase-3	-	0.38
25	α_{StC}	Inhibition strength of STAT3 on Caspase-3	-	1
26	α_{AC}	Inhibition strength of Akt on Caspase-3	-	1.06
27	α_{CA}	Inhibition strength of Caspase-3 on Akt	-	1.42
28	α_{RH}	Inhibition strength of radicicol on Hsp90	mol^{-1}	2.25
29	α_{XC}	Inhibition strength of X on Caspase-3	-	2.22
30	x_H	Activation constant of docetaxel on Hsp90	$\text{mol}^{-1}\cdot \text{hr}^{-1}$	1.4
31	x_E	Activation constant of docetaxel on ERK	$\text{mol}^{-1}\cdot \text{hr}^{-1}$	0.54
32	x_A	Activation constant of docetaxel on Akt	$\text{mol}^{-1}\cdot \text{hr}^{-1}$	14.63

Table 4.1: HSP90 fit parameters, rounded to two decimal places, as a result of the genetic algorithm in MATLAB.

Name	Parameter Description	Units	Value
b_{H1}	(Uninhibited) "production" rate of Hsp90	hr^{-1}	10.91
b_{Sr}	"Production" rate of Src	hr^{-1}	0.91
b_{E}	"Production" rate of ERK	hr^{-1}	13.48
b_{St}	"Production" rate of STAT3	hr^{-1}	1.87
b_{A1}	(Uninhibited) "production" rate of Akt	hr^{-1}	265.92
b_{C1}	(Uninhibited) "production" rate of Caspase-3	hr^{-1}	86.83
β_{DX}	"Removal" rate of X	$\text{mol}^{-1}\cdot\ \text{hr}^{-1}$	1

Table 4.2: Hsp90 set parameters, rounded to two decimal places, as a result of the parameter constraints necessary to maintain equilibrium in a drug-naive state.

ensure that drug levels decrease after the drug is no longer being taken in by the cell; and e) drug intake rates must be sufficiently slow to ensure that the protein levels take at least 12 hours to saturate within the cell, i.e. the protein dynamics are changing/saturating in a relevant timescale.

$$b_{H1} = b_{H2}\left(d_H\right) \tag{4.12}$$

$$b_{Sr} = d_{Sr} - k_{HSr} \tag{4.13}$$

$$b_E = d_E - k_{HE} - k_{SrE} - k_{StE} \tag{4.14}$$

$$b_{St} = d_{St} - k_{SrSt} - k_{ESt} \tag{4.15}$$

$$b_{A1} = \left(b_{A2} + \alpha_{CA}\right)\left(d_A - k_{HA} - k_{SrA} - k_{StA}\right) \tag{4.16}$$

$$b_{C1} = d_C\left(b_{C2} + \alpha_{HC} + \alpha_{EC} + \alpha_{StC} + \alpha_{AC} + \alpha_{XC}\right) \tag{4.17}$$

Although the set of parameters is not unique, it is sufficiently close to model the protein dynamics and most of the parameters are within the same orders of magnitude as in other systems biology models, e.g. [87]. Some of the parameter values related to ERK and Akt have high parameter values, but this is probably due to the fact that these proteins are key proteins in other survival pathways, i.e. the Raf-MEK-ERK pathway [88] and the PI3K-Akt pathway [89]. We should note that we are comparing to other systems biology models that have uncertainty in their model parameters as well. And even if we had a systems biology model with more confidence in their model parameters, the difference in model structure complicates any comparison. Our model is a minimal model that simplifies the relationship between parameters, but in reality, there are additional steps and other species that are present in the network. Thus, the resulting values for our parameters are not easily compared to those in other systems biology models. All model parameters are shown in Tables 4.1 and 4.2. Additionally, the ad hoc removal rate of X was set arbitrarily to ensure a smooth and complete transition to a docetaxel-treated cell that is dependent only on the Hsp90-dependent survival pathways.

4.3 Results

4.3.1 Treatment schedules

After determining the model network, constraints, and parameters, we tested the hypothesis that temporal sequencing of radicicol and docetaxel can overcome the activation of multiple survival kinases. With the given set of parameters, *in silico* experiments were completed to compare the two treatment sequences (docetaxel-radicicol and radicicol-docetaxel). As stated earlier in Section 4.2.3, we assume that the cells are initially in a drug-naive state with all proteins at equilibrium.

The results suggest that administering docetaxel first initially increases survival protein expression in the cell with increased Hsp90 levels. However, this sensitizes the cell so that radicicol has a significant impact, resulting in increased Caspase-3. In the radicicol-docetaxel treatment, radicicol is able to moderately increase Caspase-3 levels, but this effect is largely negated by the “boost” in survival protein expression induced by docetaxel. The normalized protein levels with respect to time as in the treatment schedules are plotted in Figure 4.2.

4.3.2 Drug delivery

Given the results in Section 4.3.1, we decided to test the docetaxel-radicicol synergy in a nanoparticle drug delivery vehicle. To do this, we develop a relationship for the drug parameters of two different drug deliveries (free drug and nanoparticle) so that the two different formulations result in the same amount of drug exposure within the cell. Mathematically, we would like the definite integral of the function representing the drug amount in the cell over time to be equal for both formulations (also corresponding to having the same AUC).

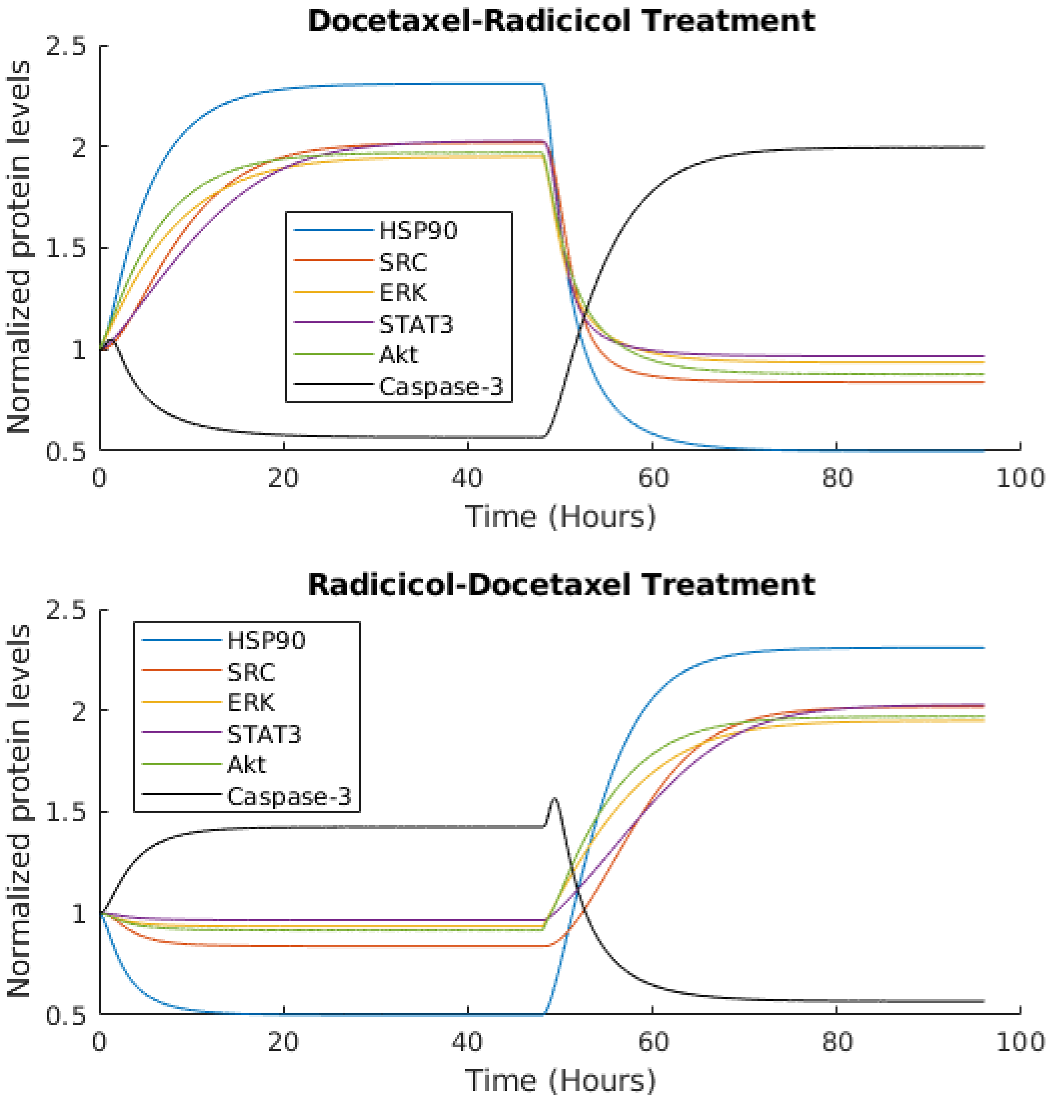

Figure 4.2: The effect of treatment sequencing on the normalized protein levels. In each treatment sequence, the first drug was administered at $t = 0$ hours, followed by drug washout and administration of the second drug at $t = 48$ hours. The results suggest that the docetaxel-radicicol treatment schedule results in lower normalized prosurvival protein levels and a higher normalized Caspase-3 level, signifying increased cell death and greater treatment efficacy. The model parameters are given in Tables 4.1 and 4.2.

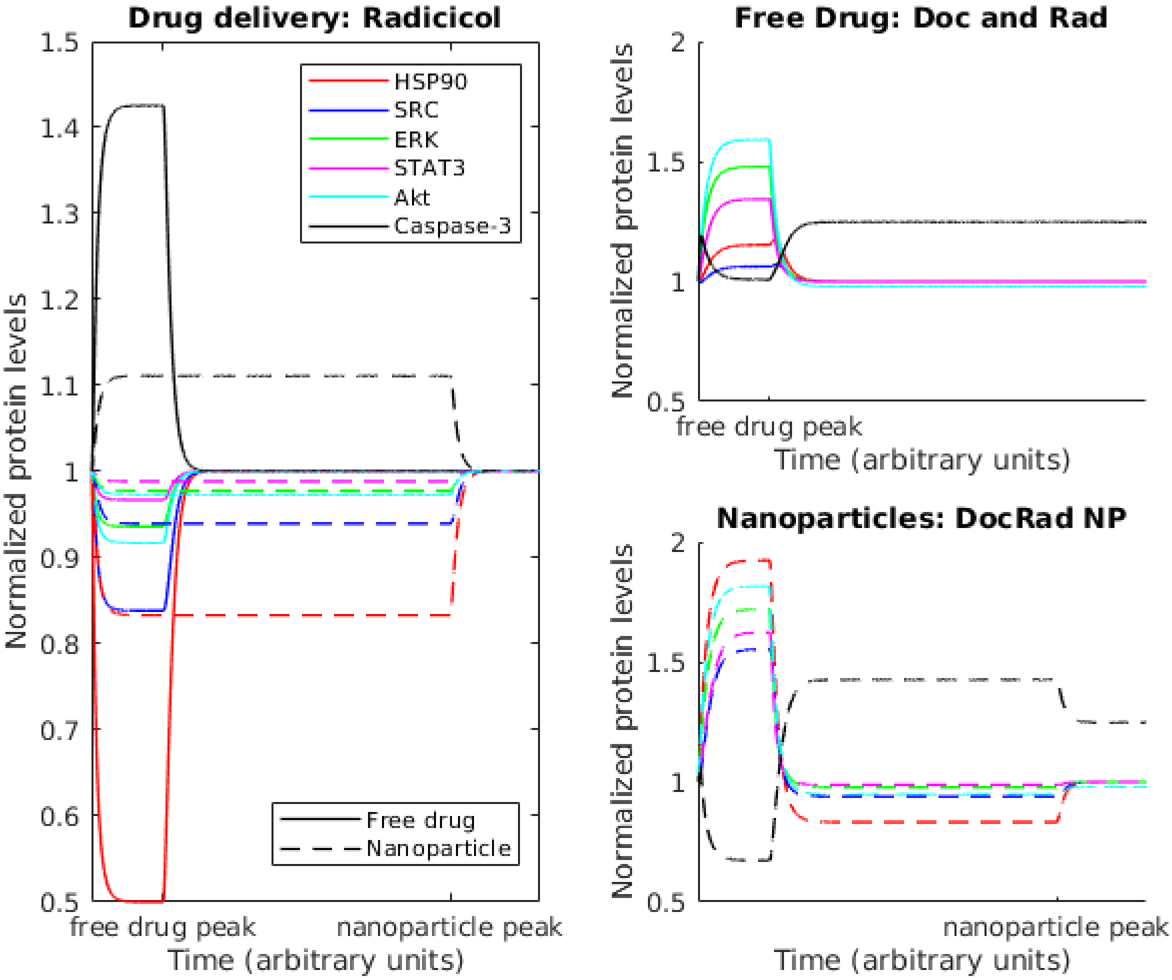

Figure 4.3: The effect of drug delivery on the normalized protein levels. (left) Normalized protein levels for free drug (solid lines) and for nanoparticles (dashed lines) for radicicol only. (right) Normalized protein levels for free drug (solid lines, top plot) and for nanoparticles (dashed lines, bottom plot) for both docetaxel and radicicol. We extended the time of radicicol uptake by a factor of five for the theoretical nanoparticle formulation and adjusted the drug nanoparticle parameters to ensure a fair comparison (see Equation 4.38). For both cases, the drug was administered at $t = 0$. We found that nanoparticles better take advantage of the synergy between docetaxel and radicicol.

If we consider a drug being administered (e.g. Equations 4.10 and 4.11), we have two different functions, $y_1(t)$ and $y_2(\mathrm{t})$, to represent the amount of drug within the cell when drug is available in the microenvironment and when the drug is absent from the microenvironment respectively. Let t^* be the time when the drug is no longer in the microenvironment. Thus, assuming that the drug is administered at $t = 0$, we define $y(t)$, the amount of drug within the cell, as in Equation 4.18.

$$y(t) = \begin{cases} y_1(t) & 0 \leq t \leq t^* \\ y_2(t) & t > t^* \end{cases} \tag{4.18}$$

which can be derived from the differential equation 4.19.

$$\frac{dy}{dt} = b(t) - \delta y \tag{4.19}$$
$$b(t) = \begin{cases} b & 0 \leq t \leq t^* \\ 0 & t > t^* \end{cases}$$

We require $y(t)$ to be a continuous function, so below, we solve the differential equations for $y_1(t)$ and $y_2(t)$ and set the initial conditions so that $y_1(t^*) = y_2(t^*)$.

When the drug is available in the microenvironment, the change in drug concentration increases at a drug uptake rate of b and decays at an exponential rate of δ. We assume that the drug concentration at $t = 0$ is 0, and we can solve this differential equation to give us the following equation for $y_1(t)$ as shown in Equation 4.20.

$$\frac{dy_1}{dt} = b - \delta y_1,\ y_1(0) = 0 \qquad \Longrightarrow \qquad y_1(t) = \frac{b}{\delta}\left[1 - \exp(-\delta t)\right] \tag{4.20}$$

When there is no drug available in the microenvironment, then the drug concentration only changes due to exponential decay at a rate of δ. We can calculate a general solution to this differential equation, giving us $y_2(t)$ as shown in Equation 4.21.

$$\frac{dy_2}{dt} = -\delta y_2 \qquad \Longrightarrow \qquad y_2(t) = C \exp(-\delta t) \tag{4.21}$$

Since the drug concentration is continuous for the duration of the treatment, we require the two functions to be equal at $t = t^*$, i.e. $y_2(t^*) = y_1(t^*)$. This becomes an initial condition for $y_2(t)$, so we solve for $y_2(t)$ as calculated in Equations 4.22 - 4.25.

$$y_2(t^*) = y_1(t^*) \tag{4.22}$$

$$C\exp(-\delta t^*) = \frac{b}{\delta}\left[1 - \exp(-\delta t^*)\right] \tag{4.23}$$

$$C = \frac{b}{\delta}\left[\exp(\delta t^*) - 1\right] \tag{4.24}$$

$$\implies y_2(t) = \frac{b}{\delta}\left[\exp(\delta t^*) - 1\right]\exp(-\delta t) \tag{4.25}$$

Thus, the equations for $y_1(t)$ and $y_2(t)$ are given in Equations 4.26 and 4.27.

$$y_1(t) = \frac{b}{\delta}\left[1 - \exp(-\delta t)\right] \tag{4.26}$$

$$y_2(t) = \frac{b}{\delta}\left[\exp(\delta t^*) - 1\right]\exp(-\delta t) \tag{4.27}$$

Now that we have the two functions for our drug dynamics, we can integrate them over their respective domains and add them together to calculate the total amount of drug over the course of treatment. The calculation is shown in Equations 4.28 - 4.36.

$$\int_0^{t^*} \frac{b}{\delta}\left[1 - \exp(-\delta t)\right]dt = \frac{b}{\delta}\left[t - \frac{\exp(-\delta t)}{-\delta}\right]\Bigg|_0^{t^*} \tag{4.28}$$

$$= \frac{b}{\delta}\left[t^* + \frac{\exp(-\delta t^*)}{\delta} - \frac{1}{\delta}\right] \tag{4.29}$$

$$= \frac{b}{\delta^2}\left[\delta t^* + \exp(-\delta t^*) - 1\right] \tag{4.30}$$

$$\int_{t^*}^{\infty} \frac{b}{\delta}\left[\exp(\delta t^*) - 1\right]\exp(-\delta t)dt = \lim_{s\to\infty}\int_{t^*}^{s} \frac{b}{\delta}\left[\exp(\delta t^*) - 1\right]\exp(-\delta t)dt \tag{4.31}$$

$$= \lim_{s\to\infty}\frac{b}{\delta}\left[\exp(\delta t^*) - 1\right]\frac{\exp(-\delta t)}{-\delta}\Bigg|_{t^*}^{s} \tag{4.32}$$

$$= \lim_{s\to\infty}\frac{b}{\delta^2}\left[1 - \exp(\delta t^*)\right]\left(\exp(-\delta s) - \exp(-\delta t^*)\right) \tag{4.33}$$

$$= \frac{b}{\delta^2}\left[1 - \exp(-\delta t^*)\right] \tag{4.34}$$

$$\frac{b}{\delta^2}\left[\delta t^* + \exp(-\delta t^*) - 1\right] + \frac{b}{\delta^2}\left[1 - \exp(-\delta t^*)\right] = \frac{b}{\delta^2}(\delta t^*) \tag{4.35}$$

$$= \frac{bt^*}{\delta} \tag{4.36}$$

Thus, the total amount of drug over the course of treatment is given by Equation 4.36 and is independent of the vehicle of drug delivery, i.e. nanoparticle or free drug.

When comparing free drug and nanoparticle formulations of the drug, we set the total amount of drug for the two cases to be equal. This equality is given in Equation 4.37 and after simplification, Equation 4.38.

$$\frac{b_f\ t_f}{\delta} = \frac{b_{NP}\ t_{NP}}{\delta} \tag{4.37}$$

$$b_{NP} = \frac{b_f\ t_f}{t_{NP}} \tag{4.38}$$

Thus, we can set the drug intake rate for the nanoparticle case so that the two treatment formulations result in the same amount of drug exposure.

We assumed that a theoretical nanoparticle formulation of the drug would extend the time of drug uptake by a factor of five arbitrarily. Using the above equality to ensure a fair comparison, NP drug delivery and free drug delivery for docetaxel and radicicol together and radicicol alone were simulated. For both cases, the drug was administered at the beginning of the experiment. The only difference between the two administrations was the slower release of radicicol into the cell microenvironment for the nanoparticle drug delivery due to the cholesterol binding to radicicol in the nanoparticle design. This was modelled by decreasing the intake rate of radicicol and increasing the time for which the drug is being taken into the cell so that the total drug exposure within the cell is the same for free drug and nanoparticle drug delivery.

When we considered radicicol only, we found that the nanoparticle structure resulted in a lesser but longer lasting effect as shown in Figure 4.3. For docetaxel and radicicol together, we found that the DocRad-NP took greater advantage of the sensitizing effect of docetaxel as shown in Figure 4.3. In the free drug case, both drugs were in effect concurrently, allowing for radicicol to take effect before the cell was completely sensitized to Hsp90. In the case of the nanoparticle, due to the slow-release kinetics of radicicol, docetaxel has more time to sensitize the cell to Hsp90 so that radicicol acts on a more sensitized cell, resulting in increased Caspase-3 levels.

4.3.3 Local sensitivity analysis

Local sensitivity analysis [40] of the Caspase-3 extremum during the docetaxel-radicicol treatment schedule was completed to identify the key parameters in bringing about cell

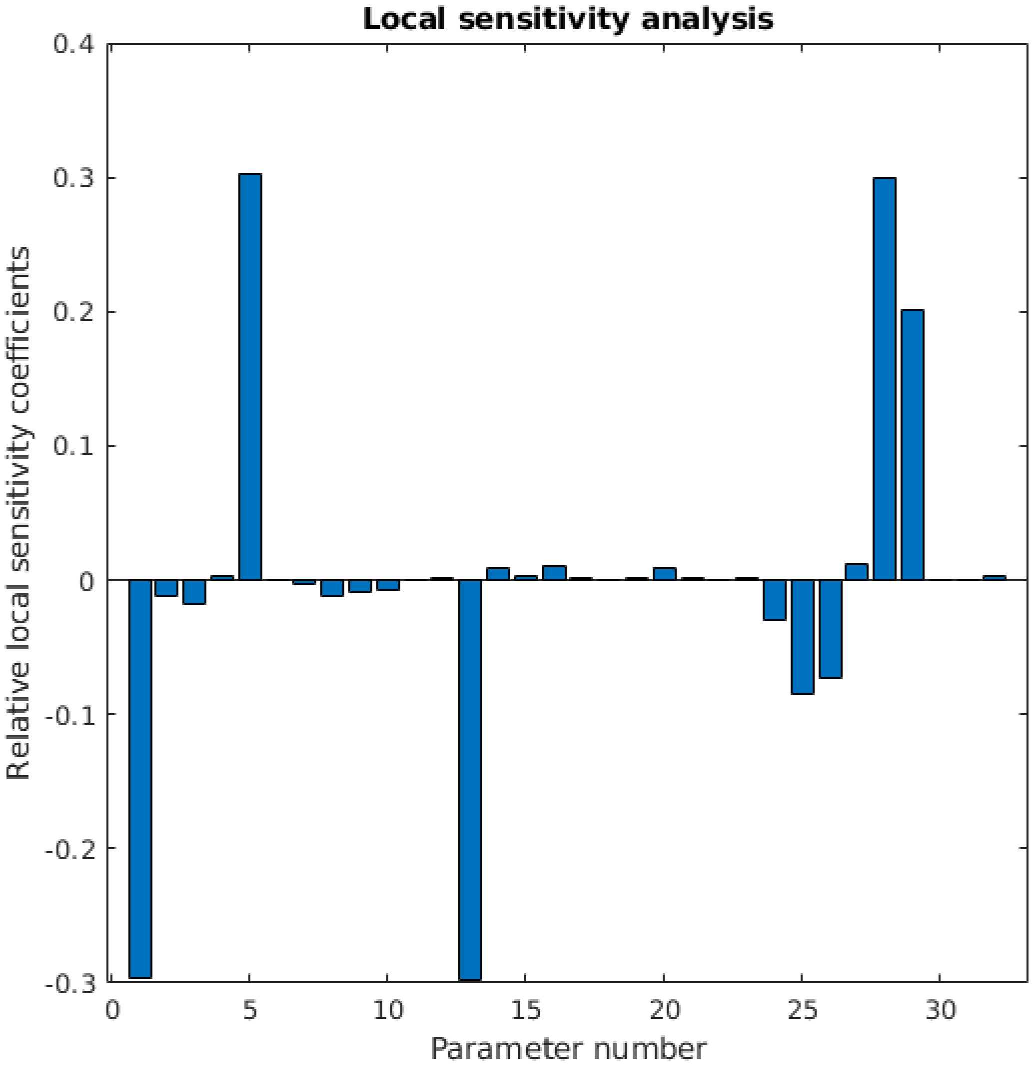

Figure 4.4: Relative local sensitivity coefficients of the Caspase-3 extremum during docetaxel-radicicol treatment schedule, looking at the relative change in the Caspase-3 extremum (over the course of the experiment) when perturbing each parameter by 1% (from the fitted parameter values). The parameter numbers and nominal parameter values are given in Table 4.1. The parameters with the highest relative sensitivities (from highest to lowest) are parameters 5, 28, 13, and 1.

death as well as to confirm that our parameters resulted in a realistic representation. Each parameter was positively perturbed individually by 1% of its nominal value, and the resulting parameter sets were simulated. In each simulation, the extremum of Caspase-3 (from steady state) was calculated and then used to calculate the change in Caspase-3 extremum (from its nominal value, i.e. using the original set of parameters, see Tables 4.1 and 4.2). The change in Caspase-3 extremum was divided by the change in the parameter to give us the absolute sensitivity of each parameter. This value was then divided by the nominal Caspase-3 extremum to calculate the relative sensitivities as shown in Figure 4.4. The absolute value of each of these relative sensitivities was then calculated to identify the key parameters and are shown in Figure 4.4. Local sensitivity analysis was repeated for different perturbation values ranging from 10^{-5} to 10^{-2} with qualitatively similar results.

The analysis identified the four most influential parameters (ordered from most to least) as 5) intake rate of radicicol, 28) inhibition strength of radicicol on Hsp90, 13) decay rate of radicicol, and 1) inhibition scaling constant for Hsp90. Note that the parameter numbers correspond to the table of fit parameters (Tables 4.1 and 4.2). As expected, the most important parameters with respect to cell death are related to the efficacy of radicicol on Hsp90. The inhibition scaling constant for Hsp90 is inherent to the nature of Hsp90, which may be outside of our control. However, the intake rate, decay rate, and inhibition strength of radicicol indicate the importance of radicicol as a follow-up drug to docetaxel in this treatment sequence. Improving the efficacy of radicicol on Hsp90 in the docetaxel-radicicol treatment sequence may improve this treatment.

4.4 Discussion

In this study, we identified the Hsp90 protein network as a means by which we can overcome drug resistance in drug-tolerant cancer cells. *In silico* experiments were used to give evidence that radicicol can overcome the development of drug resistance in drug-tolerant cancer cells from docetaxel if the treatment sequence took advantage of the synergy between the two drugs. To our knowledge, this is the first model to analyze the Hsp90 protein network in a drug-tolerant cancer cell and design a treatment schedule to overcome its drug resistance.

Additionally, we considered an alternative drug formulation. Using *in silico* experiments, we gave evidence that using drug nanoparticles took better advantage of the synergy between docetaxel and radicicol compared to the simultaneous release of free drug into the tumour microenvironment. Due to the slower release of radicicol in the nanoparticles, cells had more time to develop resistance to docetaxel before radicicol effected the reversal of resistance in those drug-tolerant cancer cells, resulting in a greater increase of cell death.

Finally, we used the model to identify key mechanisms or factors that would be most effective in increasing cell death with the docetaxel-radicicol treatment sequence. All the significant parameters were related to Hsp90 activity, confirming the importance of this drug in effecting cell death in a drug-tolerant cancer cell. The inhibition strength of radicicol on Hsp90 and the inhibition scaling constant for Hsp90 are parameters that would be dependent on the patient characteristics, which is likely outside of the clinician's control. On the other hand, the intake rate and the decay rate of radicicol are drug properties. Drug intake rate is dependent on factors like permeability across cell membranes, while drug decay rate is dependent on how quickly the drug is metabolized or degraded within the cell. Thus, radicicol could potentially be improved with respect to these drug characteristics.

4.4.1 Future work

There is further analysis and model improvements or extensions that we can add to this model. Further analysis includes global sensitivity analysis [40], model reduction [40], identifiability analysis [39], and uncertainty analysis [55]. Model improvements and extensions include explicitly modelling the drug in the cell microenvironment, improving our model assumptions in constructing the model equations, and adding biological details such as the caspase cascade or other survival pathways.

In this work, we utilized local sensitivity analysis to identify the key parameters in bringing about cell death during the docetaxel-radicicol treatment sequence. However, our local sensitivity analysis results are limited due to the uncertainty in our parameter values. In other words, there is uncertainty that we are in the correct point within the parameter space. Due to this uncertainty, global sensitivity would better capture the effect of the model parameters on bringing about cell death. Global sensitivity analysis is used to identify the most significant parameters across the entire parameter space, as opposed to local sensitivity analysis, which calculates sensitivities for a specific set of parameters, i.e. a specific point within the parameter space. Calculating global sensitivities would thus identify the most significant parameters independent of the particular parameter fit or cell line that we're working with. Global sensitivities can also identify the most effective ways of traversing the parameter space, which can be very useful when trying to modify the phenotype or behaviour of a cell line, e.g. manipulating a cell line from a drug-tolerant state to a drug-responsive state [40].

Along with sensitivity analysis, we could apply a model reduction to this Hsp90 model by identifying the key reactions necessary to produce the desired output (a proper fit to *in vitro* data). This model reduction would reduce the number of parameters and make *in silico* experiments more cost-effective with regards to computational time [40].

Identifiability analysis is used to evaluate whether it is theoretically possible to identify the true values of a model. It is important that we check that our model is identifiable before assessing the accuracy of our parameters [39]. Once a model has been identified as identifiable or once it has been modified to be identifiable, uncertainty analysis is used to evaluate our parameter estimates by calculating the confidence intervals for each parameter. Thus, we can evaluate the probability that our set of parameters is an accurate description of the observed phenomenon [55].

This model could also be improved or extended with additional biological details. One model improvement is to explicitly model the amount of drug in the cell microenvironment. This additional information could be used to model the diffusion of drug into the cell based on the drug gradient between the cell and cell microenvironment.

Another model improvement is to remove two of the simplifying assumptions made in constructing the minimal model. One simplifying assumption made is that the amount of activated protein can serve as a proxy for the amount of inactivated protein. This is a simplifying assumption that was made to reduce the number of species included in the model, but it is not supported by any biological evidence. Our phenomenological model currently uses simple products to capture the correlated activation of key prosurvival proteins. However, these reactions could be researched further to distinguish between direct or indirect interactions between proteins. Once these interactions have been clarified, terms specific to the protein interaction could be used. For our second simplifying assumption, the effect of docetaxel on Hsp90, ERK, and Akt is included as a simple increase in background activation that is dependent only on the amount of drug within the cell. These interactions could also be clarified so that the corresponding terms better reflect the biological phenomena.

We could also explicitly model the caspase cascade by including other kinases and caspases that are significant in the apoptotic machinery of the cell, such as in Lee et al. [90]. This would be useful only with additional *in vitro* measurements since the current framework already captures a basic trigger for apoptosis. The additional measurements may identify any additional complexity or nuance in the apoptotic process of a cell.

We could also explicitly model the other survival pathways represented by X, such as the EGF signal transduction pathway [91], to better understand and model the Hsp90 sensitization of a drug-tolerant cancer cell through docetaxel. Our current framework includes this phenomenon simplistically, so it may benefit from a more explicit and detailed modelling of the sensitization process.

Chapter 5

Explaining variability in patient response to anti-PD-1 immunotherapy

In this chapter, we investigate the variability in immune system response to anti-PD-1 immunotherapy. PD-1 (programmed cell death protein 1) is a cell surface molecule that is exhibited on cancer cells and activated T cells. Immune cells that are expressing PD-1 are inhibited when PD-1 is engaged by its ligands (e.g. PD-L1). Anti-PD1 immunotherapy such as nivolumab has been investigated to prevent the inhibition of immune cells by PD-1 ligation. Thus, we would expect nivolumab to result in increased activation of T cells and subsequent cancer regression [43]. However, anti-PD-1 immunotherapy treatment has resulted in both positive and negative results in its ability to inhibit tumour growth. We hypothesized that Th1 and Th2 cells determines immune response [44]. In this work, we construct a systems biology model and utilize sensitivity analysis to identify potential biomarkers for a positive response to anti-PD-1 immunotherapy.

This project was done in collaboration with Dr. Michelle Przedborski and Dr. Aaron Goldman and his team. I completed the research on the biological background involved in constructing the model. Dr. Michelle Przedborski and I jointly wrote the code for parameter estimation. I wrote the code for the local sensitivity analysis, and they wrote the code for the global sensitivity analysis. The discussion of the results was done by me in this thesis. Dr. Aaron Goldman and his team provided the *ex vivo* data (cytokine assays and flow cytometry) used in fitting the model. All the experimental details are included in the unpublished manuscript but are not included here. The experimental procedures and data will be included in full detail in the final publication. This study identified potential biomarkers of a positive response to anti-PD-1 immunotherapy that could be tested further by *in vitro* experiments. The manuscript for this project is currently in preparation.

5.1 Biological background

The immune system involves a variety of cells including T cells, B cells, antigen-presenting cells (e.g. dendritic cells) [92]. In this project, we focus on T cells as the main players in the immune system. There are several important T cell subpopulations: CD4$^+$ helper T cells [44], CD8$^+$ cytotoxic T cells [44], and regulatory T cells [93]. Regulatory T cells prevent the development of autoimmunity, where cells become hypersensitive, and the immune cells begin to destroy the host's own normal cells [93]. In this work, we assumed that regulatory T cells have the same effect on all CD4$^+$ helper Th cells and did not include them in our model for simplicity. Instead, we focused on the balance between type 1 helper T cells and type 2 helper T cells as the deciding factor between response and non-response to anti-PD1 immunotherapy [44].

5.1.1 Cytotoxic T cells

CD8$^+$ cytotoxic T cells (Tc) are the T cells mainly responsible for cell killing [44]. These cells target specific antigens and release granzyme B and perforin to induce apoptosis in the targeted cells [94]. For these cells to be activated, other immune cells such as CD4$^+$ type 1 helper T cells (see section 5.1.2) and antigen-presenting cells need to process and present specific antigens to these cells [92].

5.1.2 Helper T cells

CD4$^+$ helper T cells consist of type 1 helper T cells (Th1) and type 2 helper T cells (Th2). The primary response of the immune system is dictated by the balance of CD4$^+$ Th1 cells and CD4$^+$ Th2 cells as well as the cytokines that are produced by the antigen response [44].

If Th1 cytokines are the primary proteins available in the tumour microenvironment, Th1 cells are going to be recruited and Th2 cell activity will be inhibited. This will result in a cell-mediated pro-inflammatory response to the tumour, which generally results in the activation of T cells, specifically cytotoxic $CD8^+$ Tc cells, and subsequent cancer cell killing [44].

If Th2 cytokines are the primary proteins available in the tumour microenvironment, the immune system will respond with Th2 cell activity and inhibited Th1 cell activity, which results in a humoral immune response. A humoral immune response activates B cells, which result in antibodies handling the antigen. The lack of cell killing allows the cancer cells to escape the immune response [44]. This is one mechanism of immune escape since cancer cells promote this anti-inflammatory environment through expression of Th2 cytokines such as IL-6 [95] as well as expression of PD-L1 [43], as discussed in section 5.1.3.

Note that there are other mechanisms of immune escape. As the cancer progresses, antigen presentation by cancer cells decreases so that the immune system exhibits less activated [10]. Also, activated T cells become exhausted and inactivated with prolonged antigen exposure [96]. In this project, we focus on PD-1 and PD-L1 as the main mechanism of immune escape and neglect other strategies such as reduced antigen presentation [43].

Cytokines

In the immune system, there are many different cytokines that serve multiple functions in activation and inhibition of different T cell subpopulations. In this project, we focus on four specific cytokines: IFN_γ [97] and IL-12 [98] as Th1 promoters, and IL-4 [97] and IL-6 [95] as Th2 promoters.

IFN_γ is secreted by $CD4^+$ Th1 cells [97] and $CD8^+$ Tc cells [96]. It promotes differentiation into type 1 helper T cells [95] and inhibits $CD4^+$ Th2 growth [99]. IL-12 is produced by dendritic cells, which are activated by $CD4^+$ Th1 cells [98]. IL-12 promotes differentiation into type 1 helper T cells [97] and growth of $CD8^+$ Tc cells [11]. These two cytokines provide a positive feedback loop to $CD4^+$ Th1 cells and promote a pro-inflammatory tumour microenvironment.

IL-4 is secreted by $CD4^+$ Th2 cells and serves as an autocrine signal for Th2 cell growth. It also promotes differentiation into type 2 helper T cells [97]. IL-6 is secreted by $CD4^+$ Th2 cells and produced by antigen-presenting cells specific to cancer. IL-6 promotes IL-4 cytokine secretion [95]. Both IL-6 and IL-4 with the support of IL-6 provide a positive feedback loop for Th2 cell expansion. Cytokine expression by Th1 cells is also inhibited by IL-4 [44] and IL-6 [95].

5.1.3 PD-1, PD-L1, and anti-PD-1 immunotherapy

PD-1 (programmed cell death protein 1) is a cell surface molecule that is expressed on activated T cells. Immune cells that are expressing PD-1 are inhibited when PD-1 is engaged by its ligands (e.g. PD-L1) [43]. PD-L1 is also expressed by activated T cells but also by cancer cells. PD-L1 expression on cancer cells is also upregulated in the presence of IFN_γ, which often signifies a pro-inflammatory response [43]. This form of negative feedback helps cancer cells accomplish immune escape.

Anti-PD1 antibodies, such as nivolumab [43] or pembrolizumab [100], have been investigated as a blockade of PD-1 activity, preventing the inhibition of immune cells by PD-1 ligation. However, anti-PD-1 immunotherapy treatment has resulted in both positive and negative results in its ability to inhibit tumour growth.

5.2 Mathematical model

5.2.1 PD-1 network

The model includes one cancer cell population and five T-cell subpopulations: naive $\mathrm{CD4}^+$ helper T cells (Th0), $\mathrm{CD4}^+$ type 1 helper T cells (Th1), $\mathrm{CD4}^+$ type 2 helper T cells (Th2), naive $\mathrm{CD8}^+$ T cells, and $\mathrm{CD8}^+$ cytotoxic T cells (Tc). We also considered four key cytokines: IL-12 and IFN_γ as Th1 promoters, and IL-4 and IL-6 as Th2 promoters. To incorporate treatment, PD-1 and PD-L1 surface molecules are modelled as being expressed by certain cell populations, and nivolumab is modelled as an anti-PD-1 antibody. We assume that all cells, cytokines, protein, and drug are well-mixed within the system, so that the spatial component is negligible. After researching the cells and cytokines of the immune system, the interaction network was constructed with the relevant cell populations and cytokines, as informed by the available patient data. The figure network is shown in Figures 5.1 and 5.2.

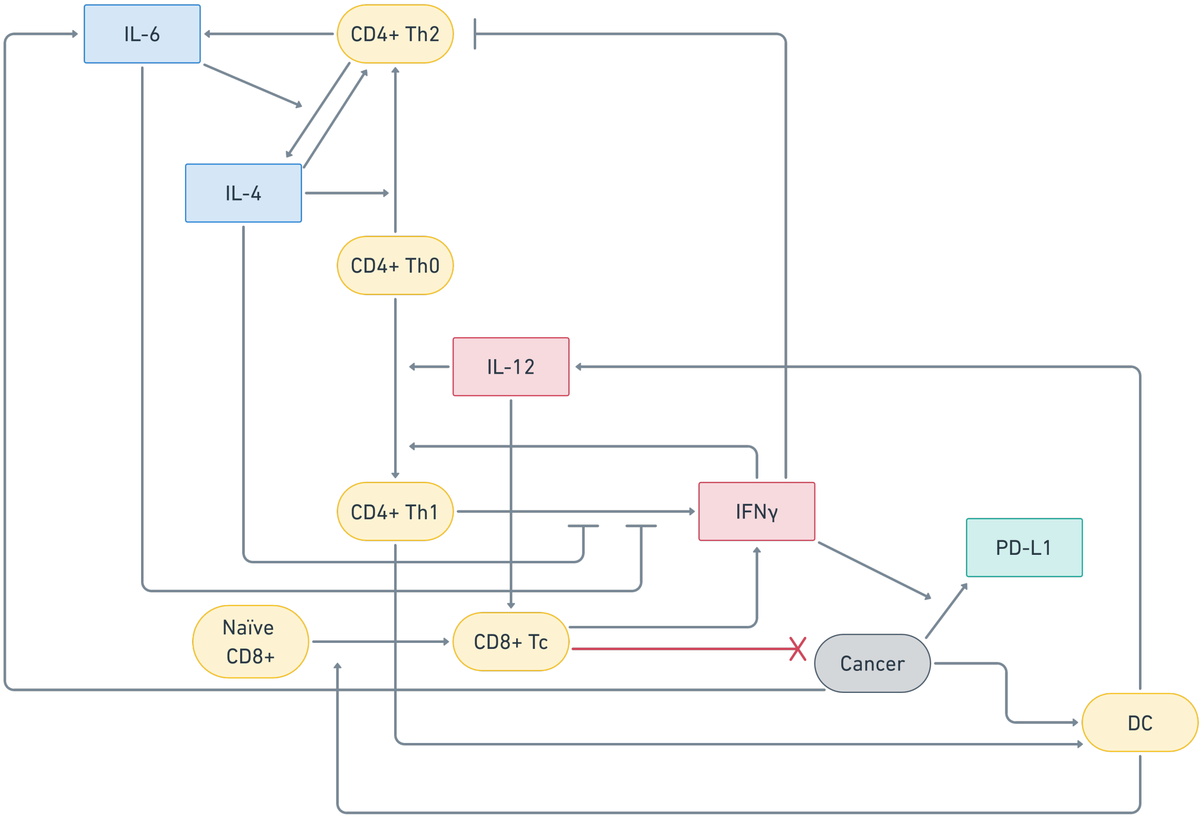

Figure 5.1: PD-1 network, part 1. This network of cells and proteins show the immune system's response to anti-PD-1 treatment. Cells are shown in ellipses (yellow for T cells and grey for cancer cells), and cytokines or cell surface molecules are shown in boxes (pink for pro-Th1 cytokines, blue for pro-Th2 cytokines, and green for cell surface molecules). Arrows show an activating relationship, and block-headed arrows show an inhibiting relationship. X-headed arrows show a cell-killing relationship.

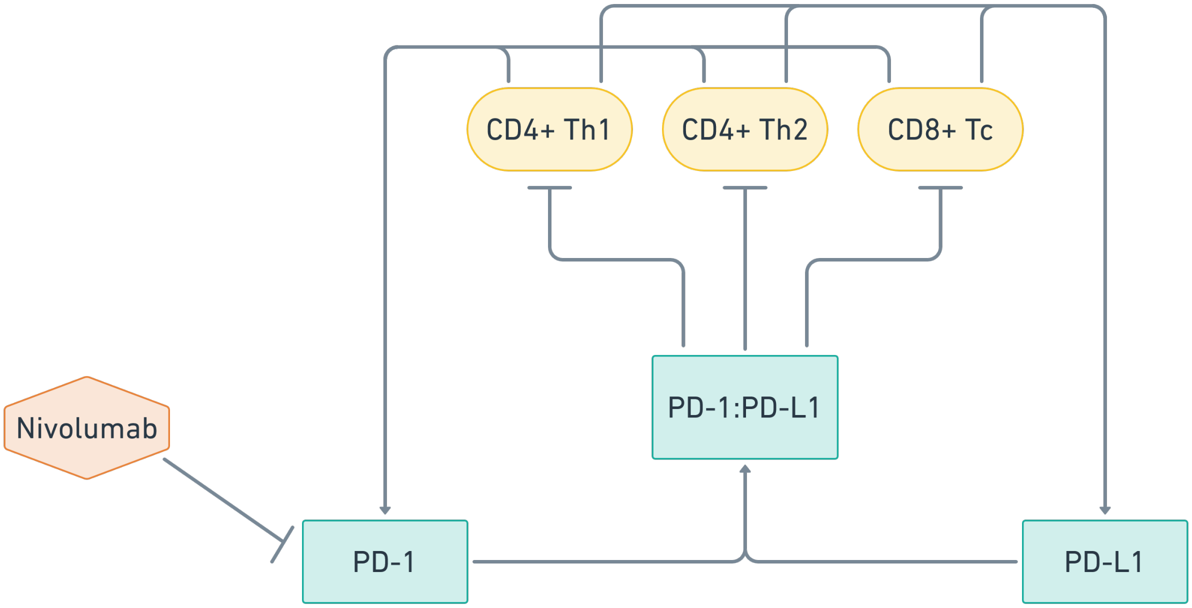

Figure 5.2: PD-1 network, part 2. This network of cells and proteins show the immune system's response to anti-PD-1 treatment. T cells are shown in ellipses and cell surface molecules are shown in green rectangles. Nivolumab, the immunotherapy, is shown in an orange hexagon. Arrows show an activating relationship, and block-headed arrows show an inhibiting relationship.

5.2.2 Model equations

The law of mass action was used to convert each of the interactions into rate laws and subsequently into a system of coupled ordinary differential equations [38]. Below, we list the assumptions made for each equation.

Naive CD4$^+$ Th0 cells (T_{N4})

$$\begin{aligned}\frac{dT_{N4}}{dt} &= n_4 T_{N4} \\ &- \left(d_{1\text{-}12} T_{N4} \frac{[IL\text{-}12]}{q_{dIL12} + [IL\text{-}12]} + d_{1\text{-}IFN} T_{N4} \frac{[IFN_\gamma]}{q_{IFN\text{-}1} + [IFN_\gamma]}\right)\left(\frac{s_1}{s_1 + [PD\text{-}1 : PD\text{-}L1]}\right) \\ &- \left(d_2 T_{N4} \frac{[IL\text{-}4]}{q_{dIL4} + [IL\text{-}4]}\right)\left(\frac{s_2}{s_2 + [PD\text{-}1 : PD\text{-}L1]}\right)\end{aligned} \tag{5.1}$$

We assume that naive CD4$^+$ Th0 cells grow exponentially through mitosis and experience exponential decay. The net proliferation of these cells is captured in the parameter n_4 (line one). We assume that naive CD4$^+$ Th0 cells can differentiate into Th1 cells in the presence of IL-12 [97] or IFN$_\gamma$ [95] (line two). We assume that naive CD4$^+$ Th0 cells can also differentiate into Th2 cells in the presence of IL-4 (line three) [95, 97]. We assume that this differentiation and subsequent activation of Th1 and Th2 is inhibited by the PD-1:PD-L1 complex (lines two and three) [43, 96, 101].

CD4$^+$ Th1 cells (Th_1)

$$\begin{aligned}\frac{dTh_1}{dt} &= n_1 Th_1 \\ &+ \left(d_{1\text{-}12} T_{N4} \frac{[IL\text{-}12]}{q_{dIL12} + [IL\text{-}12]} + d_{1\text{-}IFN} T_{N4} \frac{[IFN_\gamma]}{q_{IFN\text{-}1} + [IFN_\gamma]}\right)\left(\frac{s_1}{s_1 + [PD\text{-}1 : PD\text{-}L1]}\right)\end{aligned} \tag{5.2}$$

We assume that CD4$^+$ Th1 cells grow exponentially through mitosis and experience exponential decay. The net proliferation of these cells is captured in the parameter n_1 (line one). We assume that Th1 cells differentiate from naive CD4$^+$ Th0 cells in the presence of IL-12 [97] or IFN$_\gamma$ [95] (line two). We assume that this differentiation and subsequent activation of Th1 is inhibited by the PD-1:PD-L1 complex (line two) [43, 96, 101].

CD4$^+$ Th2 cells ($Th2$)

$$\begin{aligned}\frac{dTh_2}{dt} &= \left(g_2 Th_2 + g_{2\text{-}4} Th_2 \frac{[IL\text{-}4]}{q_{gIL4} + [IL\text{-}4]}\right)\left(\frac{r_{IFN}}{r_{IFN} + [IFN_\gamma]}\right) \\ &\quad + \left(d_2 T_{N4} \frac{[IL\text{-}4]}{q_{dIL4} + [IL\text{-}4]}\right)\left(\frac{s_2}{s_2 + [PD\text{-}1 : PD\text{-}L1]}\right) - \delta_2 Th_2\end{aligned} \tag{5.3}$$

We assume that CD4$^+$ Th2 cells grow exponentially through mitosis and experience exponential decay (lines one and two). The proliferation of CD4$^+$ Th2 cells is upregulated by IL-4 (line one) [97]. However, this proliferation was inhibited by IFN$_\gamma$ (line one) [99]. We assume that CD4$^+$ Th2 cells differentiate from naive CD4$^+$ Th0 cells in the presence of IL-4 (line two) [97]. We assume that this differentiation and subsequent activation of Th2 is inhibited by the PD-1:PD-L1 complex (line two) [43, 96, 101].

Naive CD8$^+$ T cells (T_{N8})

$$\frac{dT_{N8}}{dt} = n_8 T_{N8} - d_C T_{N8} \left(\frac{Th_1}{q_1 + Th_1}\right)\left(\frac{s_C}{s_C + [PD\text{-}1 : PD\text{-}L1]}\right) \tag{5.4}$$

We assume that naive CD8$^+$ T cells grow exponentially through mitosis and experience exponential decay. The net proliferation of these cells is captured in the parameter n_8 (first term). We assume that naive CD8$^+$ T cells differentiate into cytotoxic Tc cells in the presence of CD4$^+$ Th1 cells (second term) [11]. We assume that this differentiation and subsequent activation of cytotoxic Tc cells is inhibited by the PD-1:PD-L1 complex (second term) [43, 96, 101].

Cytotoxic CD8$^+$ Tc cells (T_c)

$$\frac{dT_c}{dt} = n_C T_c + g_{C\text{-}12} T_C \frac{[IL\text{-}12]}{q_{gIL12} + [IL\text{-}12]} + d_C T_{N8}\left(\frac{Th_1}{q_1 + Th_1}\right)\left(\frac{s_C}{s_C + [PD\text{-}1 : PD\text{-}L1]}\right) \tag{5.5}$$

We assume that cytotoxic CD8$^+$ Tc cells grow exponentially through mitosis and experience exponential decay. The net proliferation of these cells is captured in the parameter n_C (first term). We assume that the proliferation of cytotoxic CD8$^+$ T cells is upregulated in the presence of IL-12 (second term). We assume that cytotoxic CD8$^+$ Tc cells differentiate from naive CD8$^+$ T cells in the presence of CD4$^+$ Th1 cells (third term) [11]. We assume that this differentiation and subsequent activation of cytotoxic Tc cells is inhibited by the PD-1:PD-L1 complex (third term) [43, 96, 101].

Cancer cells (Can)

$$\frac{dC}{dt} = n_{Can}C - k_C C T_c \tag{5.6}$$

We assume that cancer cells grow exponentially through mitosis and experience exponential decay. The net proliferation of these cells is captured in the parameter n_{Can} (first term). We assume that cancer cells are killed by cytotoxic CD8$^+$ Tc cells through mechanisms such as granzyme/perforin-induced apoptosis (second term) [94].

Interferon gamma (IFN_γ)

$$\frac{d[IFN_\gamma]}{dt} = p_{1\text{-}IFN}Th_1\left(\frac{r_{IL4}}{r_{IL4}+[IL\text{-}4]}\right)\left(\frac{r_{IL6}}{r_{IL6}+[IL\text{-}6]}\right) + p_{C\text{-}IFN}T_c - \delta_{IFN}[IFN_\gamma] \tag{5.7}$$

We assume that IFN$_\gamma$ is secreted by CD4$^+$ Th1 cells [97] and that this cytokine secretion is inhibited by the presence of IL-4 [102] and IL-6 [95] (first term). We assume that IFN$_\gamma$ is also secreted by cytotoxic CD8$^+$ Tc cells (second term) [96]. Finally, we assume that IFN$_\gamma$ undergoes exponential decay (third term).

Interleukin 4 (IL-4)

$$\frac{d[IL\text{-}4]}{dt} = p_{2\text{-}4}Th_2 + p_{2\text{-}4\text{-}6}Th_2\left(\frac{[IL\text{-}6]}{q_{IL6}+[IL\text{-}6]}\right) - \delta_{IL4}[IL\text{-}4] \tag{5.8}$$

We assume that IL-4 is secreted by CD4$^+$ Th2 cells [97] (first term) and that this secretion is upregulated in the presence of IL-6 [98] (second term). We also assume that IL-4 undergoes exponential decay (third term).

Interleukin 6 (IL-6)

$$\frac{d[IL\text{-}6]}{dt} = p_{2\text{-}6}Th_2 + p_{Can\text{-}6}C - \delta_{IL6}[IL\text{-}6] \tag{5.9}$$

We assume that IL-6 secreted by CD4$^+$ Th2 cells (first term). We additionally assume that IL-6 is produced by APCs, which are not explicitly modelled. However, we assume that the number of APCs would be proportional to the cancer cells so that the IL-6 produced by APCs is proportional to the amount of cancer in the system (second term) [95]. Finally, we assume IL-6 undergoes exponential decay (third term).

Interleukin 12 (IL-12)

$$\frac{d[IL\text{-}12]}{dt} = p_{Can\text{-}12}C + p_{1\text{-}12}Th1 - \delta_{IL12}[IL\text{-}12] \tag{5.10}$$

We assume that IL-12 is produced by DCs, which are not explicitly modelled. However, we assume that the amount of DCs is proportional to the number of cancer cells so that the IL-12 produced by DCs is proportional to the amount of cancer in the system (first term) [98]. We also assume that DCs are alternatively activated by Th1, so we assume that IL-12 is produced at a rate proportional to the amount of CD4$^+$ Th1 cells in the system (second term) [103]. Finally, we assume IL-12 undergoes exponential decay (third term).

Programmed cell death protein 1 (PD-1)

$$[PD\text{-}1] = \rho\left(Th_1 + Th_2 + T_c\right) \tag{5.11}$$

$$\begin{aligned}\frac{d[PD\text{-}1]}{dt} &= \rho\left(\frac{dTh_1}{dt} + \frac{dTh_2}{dt} + \frac{dT_C}{dt}\right) - \beta_+[PD\text{-}1][PD\text{-}L1] + \beta_-[PD\text{-}1 : PD\text{-}L1] \\ &- \alpha_+[PD\text{-}1][A] + \alpha_-[A : PD\text{-}1]\end{aligned} \tag{5.12}$$

We assume that PD-1 is expressed on all activated T cells, i.e. CD4$^+$ Th1 cells, CD4$^+$ Th2 cells, and cytotoxic CD8$^+$ Tc cells [96], and we additionally assume that the same amount of PD-1 is expressed on all types of T cells. Thus, the amount of PD-1 is proportional to the sum of these cell populations (Equation 5.11). We assume that PD-1 can bind to and disassociate from PD-L1 (line one of Equation 5.12) [96] or the anti-PD-1 antibody (line two of Equation 5.12) [43].

Programmed death-ligand 1 (PD-$L1$)

$$[PD\text{-}L1] = \lambda\left(Th_1 + Th_2 + T_c + C\right) + \lambda_{Can\text{-}IFN}C\left(\frac{[IFN_\gamma]}{q_{IFN\text{-}PDL1} + [IFN_\gamma]}\right) \tag{5.13}$$

$$\begin{aligned}\frac{d[PD\text{-}L1]}{dt} &= \lambda\left(\frac{dTh_1}{dt} + \frac{dTh_2}{dt} + \frac{dT_C}{dt} + \frac{dC}{dt}\right) \\ &+ \lambda_{Can\text{-}IFN}\frac{dC}{dt}\left(\frac{[IFN_\gamma]}{q_{IFN\text{-}PDL1} + [IFN_\gamma]}\right) \\ &- \beta_+[PD\text{-}1][PD\text{-}L1] + \beta_-[PD\text{-}1 : PD\text{-}L1]\end{aligned} \tag{5.14}$$

We assume that PD-L1 is expressed on all activated T cells, i.e. CD4$^+$ Th1 cells, CD4$^+$ Th2 cells, and cytotoxic CD8$^+$ Tc cells, and we additionally assume that the same amount of PD-L1 is expressed on all types of T cells. We assume that PD-L1 is also expressed on cancer cells and that this cell surface expression is upregulated by IFN$_\gamma$ (last term of Equation 5.13). We assume that PD-L1 can bind to and disassociate from PD-1 (line three of Equation 5.14) [96].

PD-1:PD-L1 complex (PD-$1 : PD$-$L1$)

$$\frac{d[PD\text{-}1 : PD\text{-}L1]}{dt} = \beta_+[PD\text{-}1][PD\text{-}L1] - \beta_-[PD\text{-}1 : PD\text{-}L1] \tag{5.15}$$

We assume that the PD-1:PD-L1 complex is the result of the binding between free PD-1 and free PD-L1. We assume that there is both binding and disassociation with this binding [96].

Anti-PD-1 antibody (A)

$$\frac{d[A]}{dt} = \tilde{A}(t) - \alpha_+[A][PD\text{-}1] + \alpha_-[A : PD\text{-}1] - \delta_A[A] \tag{5.16}$$

We assume that the anti-PD-1 antibody is injected into the tumour microenvironment according to our treatment schedule and is mathematically defined by $\tilde{A}(t)$ (first term). We assume that there is binding and disassociation between the anti-PD-1 antibody and PD-1, and we assume that the anti-PD-1 antibody binds to PD-1 with a higher affinity than PD-L1 [43]. Thus, the disassociation constant $K_\alpha \equiv \alpha_-/\alpha_+ \ll K_\beta \equiv \beta_-/\beta_+$ (second and third terms). Finally, we assume that anti-PD-1 undergoes exponential decay (fourth term).

Anti-PD-1:PD-1 complex ($A : PD$-1)

$$\frac{d[A : PD\text{-}1]}{dt} = \alpha_+[A][PD\text{-}1] - \alpha_-[A : PD\text{-}1] \tag{5.17}$$

We assume that the A:PD-1 complex is the result of the binding between free PD-1 and free anti-PD-1 antibody. We assume that there is both binding and disassociation with this binding [43].

5.2.3 Parameter estimation

Tumour samples from fifty different patients with various head and neck cancers were cultured *ex vivo* and subjected to control and treatment conditions. Under treatment conditions, nivolumab, an anti-PD-1 antibody [43], was administered every 24 hours for three days with drug washout before subsequent drug administration. The experimental data exhibited a high degree of variability under both control and treatment conditions.

The measurements were measured using Luminex cytokine arrays [104], which measure the cytokine levels from the media surrounding the tumour sample, and using flow cytometry [52], which was used to identify the proportion of the tumour that exemplified biomarkers for specific T cell populations. For the cytokine measurements, IFN_γ, IL-12p70, and IL-6 measurements were taken at the end of each day, i.e. at $t = 24, 48$, and 72 hours. Negligible and unreliable data points were removed from the data set, and the average data and standard deviation were used in the parameter fitting process.

For the T cell subpopulations, the following biomarker expression was used: $\mathrm{CD8}^+$ biomarker expression for both naive $\mathrm{CD8}^+$ T cells and $\mathrm{CD8}^+$ Tc cells. $\mathrm{CD8}^+\mathrm{IFN}_\gamma+$ biomarker expression for $\mathrm{CD8}^+$ Tc cells since activated $\mathrm{CD8}^+$ Tc cells should be producing IFN_γ [11]. $\mathrm{CD4}^+$ biomarker expression for naive $\mathrm{CD4}^+$ Th0 cells, $\mathrm{CD4}^+$ Th1 cells, and $\mathrm{CD4}^+$ Th2 cells [97]. $\mathrm{CD4}^+\mathrm{CD25}^+$ was used to identify regulatory T cells, which is not included in our model [105]. Thus, we had a measure for the sum of the $\mathrm{CD4}^+$ Th compartments. This data was collected for control conditions and at $t = 72$ hours for treatment conditions. Negligible and unreliable was removed from the data set, and the average data and standard deviation were used in the parameter fitting process.

The parameter fitting process was joint work with Dr. Michelle Przedborski. Given the *in vitro* data collected, we needed several simulations to utilize the data appropriately. First, we assumed that the PD-1, PD-L1, and PD-1:PD-L1 complex would be at steady state at the beginning of treatment. Since the steady state depends on the kinetic parameters of PD-1, PD-L1, and the PD-1:PD-L1 complex, which vary from parameter set to parameter set, we first ran the PD-1, PD-L1, and PD-1:PD-L1 complex equations to equilibrium.

The next step was to incorporate the cytokine data from the tumour microenvironment. In the tumour microenvironment, the effect of the cancerous cells is negligible in comparison to the cytokine activity from circulating T cells. Thus, we ran the treatment simulations in the absence of cancer.

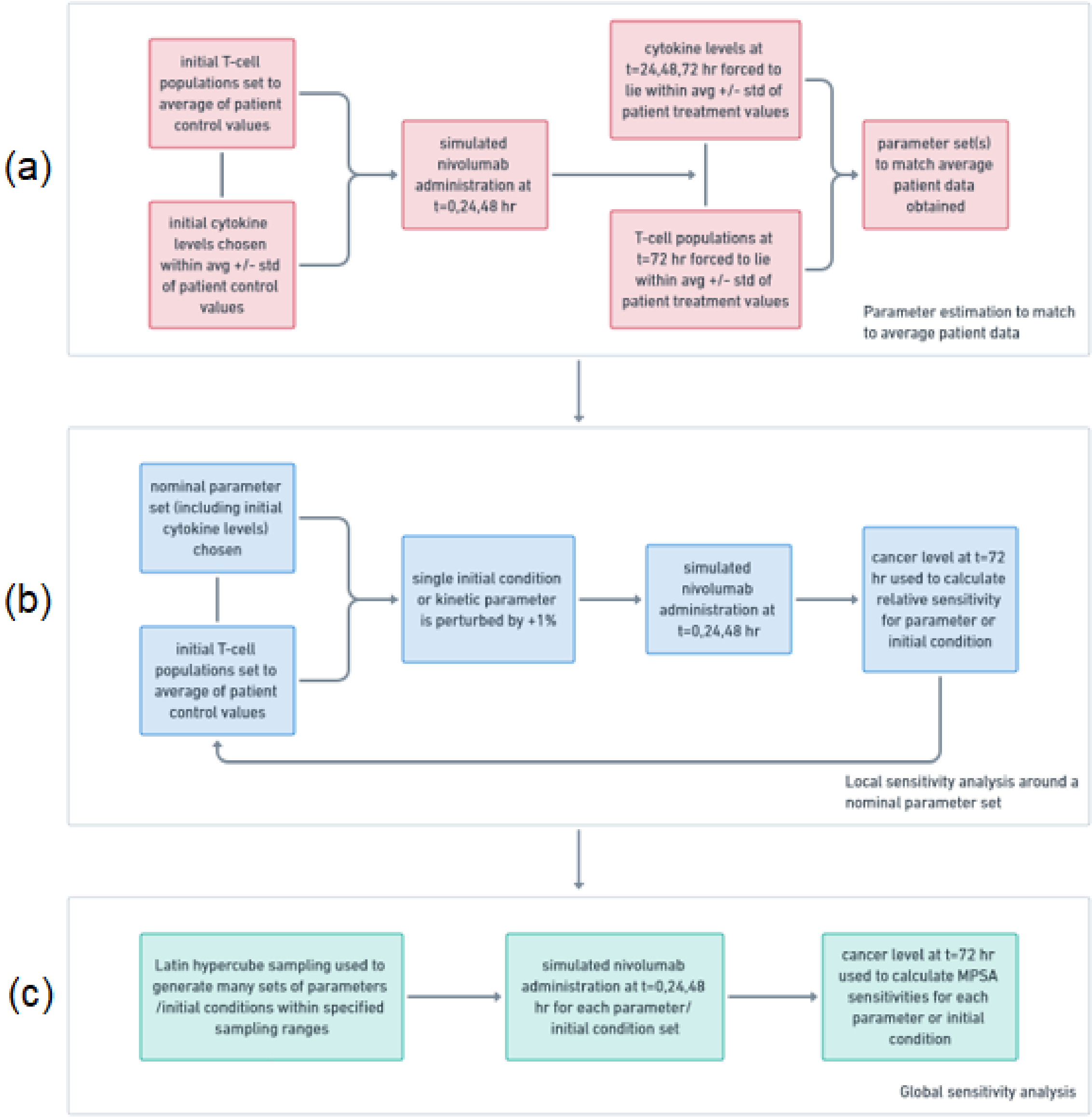

Figure 5.3: Method workflow schematics, summarizing the workflows for the following analyses: (a) parameter estimation, (b) local sensitivity analysis, and (c) global sensitivity analysis. The schematic was designed by Dr. Michelle Przedborski.

The final piece of information to incorporate was the flow cytometry data from within the tumour. We assumed that the protein dynamics of the T cells was the same within the tumour and circulating in the tumour microenvironment. Thus, the final set of simulations simulated the dynamics within the tumour with the addition of cancer and its cytokines and cell surface proteins.

Given this *in silico* setup, the genetic algorithm, ga(), in MATLAB was used to minimize the r^2 error between the *in silico* cytokine levels and T-cell proportions and within one standard deviation of the *in vitro* cytokine levels and T-cell proportions. The genetic algorithm is a global method in that it explores the entire parameter space, but it only guarantees a local minimum of the parameter space [39]. And given the variability in the *in vitro* data, there may be several sets of parameters that result in zero error. Thus, we acknowledge that this particular set of parameters is just one possible explanation for the *in silico* data (see Tables 5.1- 5.5).

Name	Parameter Description	Units	Value
$\text{IFN}_{\gamma,0}$	Initial IFN_{γ} levels	pg/ml	2.54
IL-12_0	Initial IL-12 levels	pg/ml	5.53e-1
IL-6_0	Initial IL-6 levels	pg/ml	3301.39
IL-4_0	Initial IL-4 levels	pg/ml	113.59

Table 5.1: Experimental data: average of the initial cytokine levels under control conditions, rounded to two decimal places.

Name	Parameter Description	Units	Value
C_{frac}	Initial cancer fraction	cell	3.7e-1
Th1_{frac}	Initial Th1 fraction	cell	2.46e-2
Th2_{frac}	Initial Th2 fraction	cell	1.49e-2

Table 5.2: PD-1 parameter fit: initial cell proportions, rounded to two decimal places.

#	Name	Parameter Description	Units	Value
1	n_4	Net proliferation of Th0 cells	hr^{-1}	9.98e-5
2	n_8	Net proliferation of naive CD8$^+$ T cells	hr^{-1}	4.57e-4
3	n_1	Net proliferation of Th1 cells	hr^{-1}	3.82e-4
4	n_C	Net proliferation of Tc cells	hr^{-1}	9.29e-5
5	n_{Can}	Net proliferation of cancer cells	hr^{-1}	1.36e-3
6	g_2	Growth of Th2 cells	hr^{-1}	2.81e-4
7	$g_{2\text{-}4}$	Growth of Th2 cells by IL-4	hr^{-1}	1.49e-4
8	$g_{C\text{-}12}$	Growth of Tc cells by IL-12	hr^{-1}	2e-4
9	δ_2	Death of Th2 cells	hr^{-1}	9.61e-6
10	$d_{1\text{-}IFN}$	Differentiation into Th1 cells by IFN$_\gamma$	hr^{-1}	2.11e-4
11	$d_{1\text{-}12}$	Differentiation into Th1 cells by IL-12	hr^{-1}	2.39e-4
12	d_2	Differentiation into Th2 cells	hr^{-1}	1.24e-4
13	d_C	Differentiation into Tc cells	hr^{-1}	1.5e-4
14	k_C	Cell killing of cancer cells by Tc cells	$\text{cell}^{-1}\cdot\ \text{hr}^{-1}$	1.51e-8
15	$p_{1\text{-}IFN}$	Production of IFN$_\gamma$ by Th1 cells	pg/(ml·cell·hr)	1.13e-6
16	$p_{2\text{-}4\text{-}6}$	Production of IL-4 by Th2 cells by IL-6	pg/(ml·cell·hr)	6.61e-7
17	$p_{Can\text{-}6}$	Production of IL-6 by cancer cells	pg/(ml·cell·hr)	2.02e-5
18	$p_{Can\text{-}12}$	Production of IL-12 by cancer cells	pg/(ml·cell·hr)	1.5e-9
19	δ_{IFN}	Decay of IFN$_\gamma$	hr^{-1}	3.74e-3
20	δ_{IL4}	Decay of IL-4	hr^{-1}	1.05e-3
21	δ_{IL6}	Decay of IL-6	hr^{-1}	4.69e-3
22	δ_{IL12}	Decay of IL-12	hr^{-1}	5.01e-4
23	δ_A	Decay of anti-PD-1 antibody	hr^{-1}	1.74e-5

Table 5.3: PD-1 parameter fit: kinetic parameters, part 1, rounded to two decimal places.

#	Name	Parameter Description	Units	Value
24	q_1	Saturation constant for Tc differentiation by Th1	cell	843.43
25	$q_{IFN\text{-}1}$	Saturation constant for Th1 differentiation by IFN_γ	cell	2.02
26	$q_{IFN\text{-}PDL1}$	Saturation constant for PD-L1 upregulation on cancer cells by IFN_γ	pg/ml	1.27
27	q_{gIL4}	Saturation constant for Th2 growth by IL-4	pg/ml	7.15
28	q_{dIL4}	Saturation constant for Th2 differentiation by IL-4	pg/ml	6.88
29	q_{IL6}	Saturation constant for IL-4 production by IL-6	pg/ml	416.42
30	q_{dIL12}	Saturation constant for Th1 differentiation by IL-12	pg/ml	6.03e-1
31	q_{gIL12}	Saturation constant for Tc growth by IL-12	pg/ml	2.19
32	r_{IFN}	Constant for IFN_γ's inhbition of Th2 cell growth	pg/ml	1.37
33	r_{IL4}	Constant for IL-4's inhibition of IFN_γ production by Th1 cells	pg/ml	10.04
34	r_{IL6}	Constant for IL-6's inhibition of IFN_γ production by Th1 cells	pg/ml	217.83
35	ρ	Expression rate of PD-1 on all activated T cells	pg/(ml·cell)	1.33e-1
36	λ	Expression rate of PD-L1 on all activated T cells	pg/(ml·cell)	9.94
37	$\lambda_{Can\text{-}IFN}$	Expression rate of PD-L1 on cancer cells	pg/(ml·cell)	1.11e-3
38	β_+	Binding rate of free PD-1 to free PD-L1	$\text{mol}^{-1} \cdot \text{hr}^{-1}$	2.71e-4
39	β_-	Disassociation rate of PD-1:PD-L1	hr^{-1}	4.24e-2
40	α_-	Disassociation rate of A:PD-1	hr^{-1}	1.88e-6
41	s_1	Constant for inhibition of Th1 differentiation by PD-1:PD-L1	pg/ml	5
42	s_2	Constant for inhibition of Th2 differentiation by PD-1:PD-L1	pg/ml	5.82
43	s_C	Constant for inhibition of Tc differentiation by PD-1:PD-L1	pg/ml	11.13

Table 5.4: PD-1 parameter fit: kinetic parameters, part 2, rounded to two decimal places.

Name	Parameter Description	Units	Value
$p_{1\text{-}12}$	Production of IL-12 by CD4$^+$ Th1 cells	pg/(ml·cell·hr)	4.54e-7
$p_{2\text{-}6}$	Production of IL-6 by CD4$^+$ Th2 cells	pg/(ml·cell·hr)	4.19e-2
$p_{2\text{-}4}$	Production of IL-4 by CD4$^+$ Th2 cells	pg/(ml·cell·hr)	3.23e-4
$p_{C\text{-}IFN}$	Production of IFN$_\gamma$ by CD8$^+$ cytotoxic Tc cells	pg/(ml·cell·hr)	9.07e-7

Table 5.5: PD-1 parameter fit: calculated kinetic parameters, rounded to two decimal places.

5.3 Sensitivity analysis

5.3.1 Local sensitivity analysis

Given the nominal parameter fit of kinetic parameters and initial cytokine levels, local sensitivity analysis [41] of the cancer level post-treatment was completed to identify the key kinetic parameters and key initial conditions in producing successful treatment, which is defined as a reduction in the cancer level after treatment. The initial T-cell populations were set to the average of the *in vitro* control values. Each initial condition and each kinetic parameter was individually perturbed by 1%, and the resulting set of parameters was used to simulate the treatment sequence.

The kinetic parameters with the highest local sensitivity coefficients with respect to the post-treatment number of cancer cells were (from highest to lowest in absolute value) 14) killing of cancer cells by CD8$^+$ cytotoxic T cells, 5) net proliferation of cancer cells, 4) net proliferation of CD8$^+$ cytotoxic Tc cells, and 8) upregulation of CD8$^+$ cytotoxic Tc cell growth by IL-12. The initial condition with the highest local sensitivity coefficient with respect to the post-treatment number of cancer cells was the initial cancer fraction in the tumour microenvironment. This process is summarized in Figure 5.3, and these results can be seen in Figure 5.4.

5.3.2 Global sensitivity analysis

Global sensitivity analysis [40] was completed by Dr. Michelle Przedborski, but the interpretation of the completed analysis is done below.

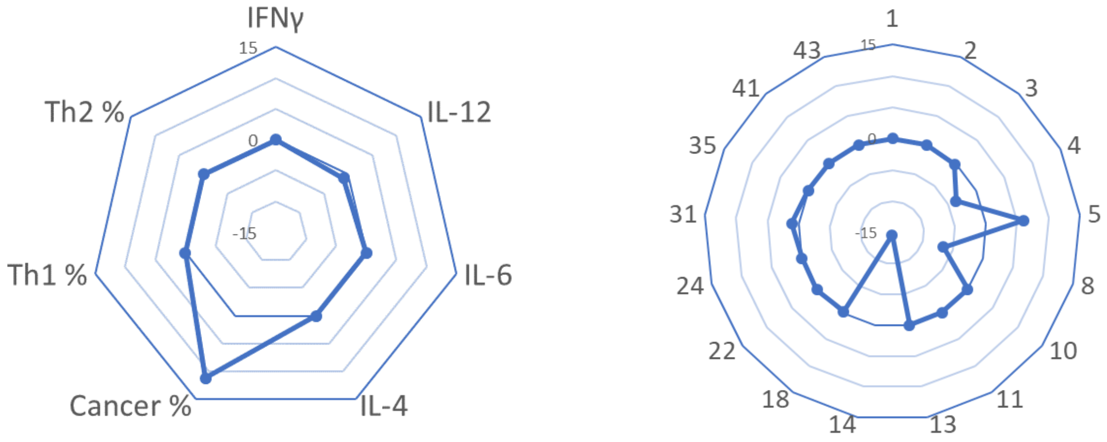
(a) Initial conditions

(b) Kinetic parameters

Figure 5.4: PD-1 local sensitivity analysis, with respect to the cancer level post-treatment (a) of the initial conditions and (b) of the most significant kinetic parameters. Each initial condition and each kinetic parameter was individually perturbed by 1%, and the resulting relative sensitivities are plotted on an axis ranging from -15 to 15. The kinetic parameters with the greatest local sensitivity coefficients (from highest to lowest in absolute value) are parameters 14, 5, 4, and 8. The initial condition with the highest local sensitivity coefficient was the initial cancer fraction.

Variability in the patient data was captured by allowing the initial cytokine levels and relative T-cell populations to vary within the range of control measurements in the *in vitro* data and by allowing the kinetic parameters to vary within large biological ranges. By allowing the initial cytokine levels and relative T-cell populations to vary within a range of input values, we can expect the resulting immune responses to exhibit the inter-patient variability that we would expect in *ex vivo* experiments or in clinical trials.

Multi-parametric sensitivity analysis [106] with Latin hypercube sampling was used to efficiently sample the parameter space and calculate the global sensitivities for the kinetic parameters and for the initial conditions in the simulation of treatment administration.

The results identified the same key kinetic parameters as the local sensitivity analysis. For the initial conditions, the initial fraction of CD8$^+$ T cells (naive and activated) and the initial fraction of cancer cells were the key initial conditions. In addition, parameters controlling the size of the Th1 and Th2 cell populations were also significant. In particular, the initial CD4$^+$ Th2 levels, the initial IL-12 levels, the initial CD4$^+$ Th1 levels, and the initial IL-6 levels were identified as important factors in treatment efficacy. This process is summarized in Figure 5.3, and these results can be seen in Figure 5.5.

5.4 Discussion

In this chapter, we construct a systems biology model to investigate the response of the immune system to anti-PD-1 cancer treatment. Using sensitivity analysis, we identified potential biomarkers for a positive response to anti-PD-1 immunotherapy, and these biomarkers could be investigated further in *in vitro* experiments. We identified the most important variables (kinetic parameters and initial conditions) to be those related to cytotoxic CD8$^+$ Tc cells and cancer cells, as expected. In addition to these expected sensitivities, the initial CD4$^+$ Th2 levels, the initial IL-12 levels, the initial CD4$^+$ Th1 levels, and the initial IL-6 levels were identified as important factors in treatment efficacy. These results reinforce the experimental observation that the variability in patient response is connected to the upregulation of Th1 levels.

Sensitivity analysis identified the interaction between cancer cells and CD8$^+$ cytotoxic T cells as an important factor with regards to anti-PD-1 immunotherapy response. Two of the significant parameters were related to the stage and invasiveness of the cancer cells (initial cancer fraction in the tumour microenvironment and net proliferation of cancer

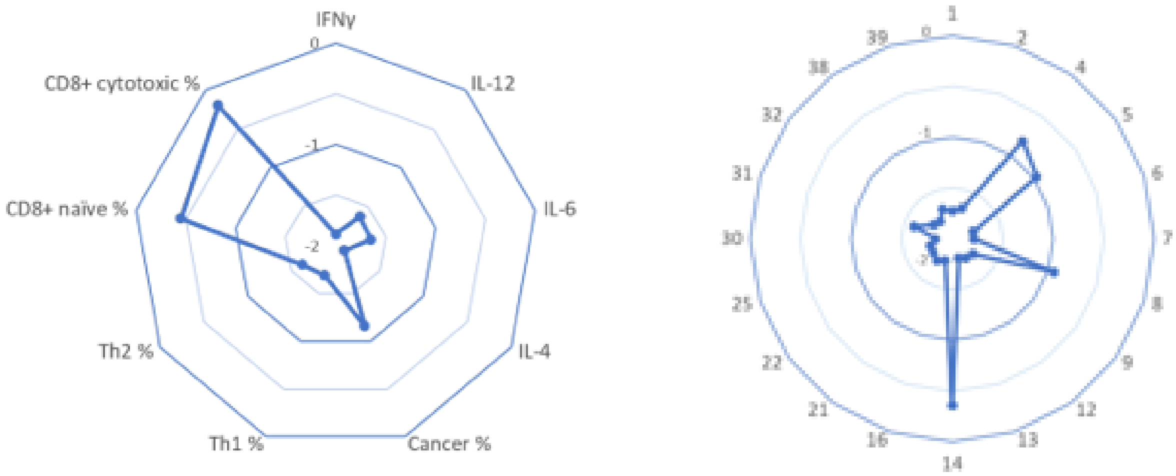

(a) Initial conditions

(b) Kinetic parameters

Figure 5.5: PD-1 global sensitivity analysis, (left) of the initial conditions and (right) of the most significant kinetic parameters. Initial cytokine levels and relative T-cell populations were varied within the range of *in vitro* control measurements and within large biological ranges, respectively. Multi-parametric sensitivity analysis [106] with Latin hypercube sampling was used to calculate the global sensitivities. The power (base 10) of the results are plotted on an axis ranging from -2 to 0 on a logarithmic scale. As in the local sensitivity analysis, the kinetic parameters with the greatest local sensitivity coefficients (from highest to lowest in absolute value) are parameters 14, 5, 4, and 8. For the initial conditions, the key initial conditions were the initial fraction of CD8$^+$ T cells (naive and activated) and the initial cancer fraction. These results were plotted by Dr. Michelle Przedborski.

cells respectively). The other three significant parameters were related to the efficacy of the patient's inherent CD$^+$ cytotoxic Tc cells (killing rate of cancer cells by CD8$^+$ cytotoxic Tc cells, net proliferation of CD8$^+$ cytotoxic Tc cells, upregulation of CD8$^+$ cytotoxic Tc cell growth by IL-12). This class of factors is largely outside the clinician's control since these characteristics are inherent to the cancer and the patient themselves.

The other significant network of interactions identified by sensitivity analysis were those between CD4$^+$ Th1 and Th2 helper cells [44]. The pre-treatment fraction of CD4$^+$ Th1 helper cells and CD4$^+$ Th2 helper cells as well as their dominant cytokines, IL-12 and IL-6 respectively, were identified as potential biomarkers of positive response to anti-PD-1 immunotherapy. This is a more useful result because these factors may be responsive to immunotherapy since these cells and cytokines have been studied and modified in other contexts, e.g. autoimmune diseases [45].

5.4.1 Future work

As in Chapter 4, there is further analysis that we can do with this model. These include model reduction [40], identifiability analysis [39], and uncertainty analysis [55].

Global sensitivity analysis is used to identify the most significant parameters across the entire parameter space, as opposed to local sensitivity analysis, which calculates sensitivities for a specific set of parameters, i.e. a specific point within the parameter space. Calculating global sensitivities would thus identify the most significant parameters independent of the particular fit or cell line that we're working with. Global sensitivities can also identify the most effective ways of traversing the parameter space, which can be very useful when trying to modify the phenotype or behaviour of a cell line, e.g. manipulating a cell line from a drug-resistant state to a drug-responsive state [40].

Along with sensitivity analysis, we could apply a model reduction to this PD-1 model by identifying the key reactions necessary to produce the desired output (a proper fit to *in vitro* data). This model reduction would reduce the number of parameters and make *in silico* experiments more cost-effective with regards to computational time [40].

Identifiability analysis is used to evaluate whether it is theoretically possible to identify the true values of a model. It is important that we check that our model is identifiable before assessing the accuracy of our parameters. Once a model has been identified as identifiable or once it has been modified to be identifiable, uncertainty analysis is used to evaluate our parameter estimates by calculating the confidence intervals for each parameter. Thus, we can evaluate the probability that our set of parameters is an accurate description of the observed phenomenon [39].

The model could also be extended with additional biological compartments. A straightforward extension would be to include regulatory T cells within the network [105]. The model could then validate or disprove the model assumption that regulatory T cells act equally on all T cell compartments.

The model could also be extended by considering other areas of the body. For instance, we could introduce additional compartments to represent the T cells within the circulating blood stream [107], the thymus [108], and the blood marrow [109]. This would make our model more relevant to an *in vivo* setting. Thus, this model could potentially predict patient response to treatment in a clinical setting.

We could also extend this model to include different types of therapy. Immunotherapy is not usually administered in isolation, so it would be more clinically relevant to include other forms of treatment such as surgery, chemotherapy, and radiation therapy [4, 5]. In particular, we could study a combination of drugs used to manipulate the Th1-Th2 balance in combination with anti-PD-1 immunotherapy to improve response to anti-PD-1 immunotherapy [45].

Chapter 6

Conclusion

In this thesis, we have shown how *in silico* experiments can be used with *in vitro* experiments to study treatment efficacy and inter-tumour and inter-patient heterogeneity.

In Chapter 2, we demonstrated a process in which experimental *in vitro* studies and computational *in silico* studies can be used together to characterize breast cancer cell lines based on their mammosphere formation dynamics. To our knowledge, this model is the first example of an agent-based model (of the hierarchy model) to study the early cancer stage of mammosphere formation [42].

We demonstrated how sensitivity analysis can be used on the resulting *in silico* model to identify the key cellular behaviours during early cancer development of any cell line. This information is valuable in characterizing a patient's tumour and in designing a suitable treatment regime. In our demonstration using MCF-7 breast cancer cells, we produced a mathematical description of the growth dynamics of MCF-7 mammosphere formation. With the resulting model, we presented evidence that progenitor cells are the driving force behind mammosphere formation in MCF-7. Although cancer stem cells play a key role, these sensitivity analysis results indicate that progenitor cells should be our primary focus for early stages of MCF-7 growth.

Finally, the resulting *in silico* model can be used as a substitute for *in vitro* experiments. *In silico* experiments are more cost-effective and efficient than their *in vitro* counterparts, so it is valuable to have an *in silico* model as an alternative, especially in the early stages of hypothesis generation and testing.

Another important result of Chapter 2 is that we justified the use of a spatial framework when studying mammosphere growth. Migration refers to a cell's ability to either migrate outwards or push cells further away to promote further growth. In the absence of this movement or pushing outwards, we find that tumour development is limited due to self-inhibition. In this study, we gave evidence that migration was a necessary assumption in order to properly recreate the observed *in vitro* mammosphere formation dynamics. Biologically, this may be explained as the cancer's lack of adhesion inhibition, in which normal cells stop growing when they are in contact with other cells [53]. Alternatively, epithelial-mesenchymal transition may allow tumour cells to physically disperse from the inner core of the tumour, allowing for accelerated growth [24, 25]. These cancer characteristics are thus key phenomena in capturing early cancer development dynamics.

In Chapter 3, we modified the model from Chapter 2 to characterize the effect of pressure and drug on mammosphere formation. Although other microenvironmentmicroenvironmental factors have been studied, this is the first time that an experimental-mathematical study has been used to characterize the effect of pressure (with and without drug) on mammosphere formation. The study gave evidence that pressure conditions may induce increased plasticity in cell phenotype, which can lead to improved response to chemotherapy as observed in the *in vitro* experiments. Thus, pressure is an important microenvironmental factor to consider when studying tumour heterogeneity.

Another interesting result of this work is that high pressure does not affect the uptake of drug into the cells. This implies that interstitial fluid pressure prevents drug from entering the tumour microenvironment as opposed to changing the cells' ability to take in the drug.

In Chapter 4, we identified the Hsp90 protein network as a means by which we can overcome drug resistance in drug-tolerant cancer cells. An *in silico* model was used to show that radicicol can overcome the development of drug resistance in drug-tolerant cancer cells from docetaxel if the treatment sequence took advantage of the synergy between the two drugs. To our knowledge, this is the first model to analyze the Hsp90 protein network in a drug-tolerant cancer cell and design a treatment schedule to overcome its drug resistance.

Additionally, we gave evidence that a nanoparticle formulation took better advantage of the synergy between docetaxel and radicicol compared to the simultaneous release of free drug into the tumour microenvironment. Due to the slower release of radicicol in the nanoparticle formulation, cells had more time to develop resistance to docetaxel before radicicol effected the reversal of resistance in those drug-tolerant cancer cells, resulting in a greater increase of cell death.

Finally, we used the model to identify key mechanisms or factors that would be most effective in increasing cell death with the docetaxel-radicicol treatment sequence. All the significant parameters were related to Hsp90 activity, confirming the importance of this drug in effecting cell death in a drug-tolerant cancer cell. We also identified the drug intake rate and the decay rate of radicicol as drug formulation properties that could potentially improve the effect of the docetaxel-radicicol treatment sequence.

In Chapter 5, we constructed a systems biology model to investigate the response of the immune system to anti-PD-1 cancer treatment. Using sensitivity analysis, we identified two important interaction networks with regards to response to anti-PD-1 immunotherapy: 1) the interaction between cancer cells and CD8$^+$ cytotoxic Tc cells, and 2) the balance between CD4$^+$ Th1 and Th2 helper cells. These results reinforce the experimental observation that the variability in patient response is connected to the upregulation of Th1 levels.

The first network of interactions was between cancer cells and CD8$^+$ cytotoxic T cells. Some of the significant parameters were related to the stage and invasiveness of the cancer cells, and some of the significant parameters were related to the efficacy of the patient's inherent CD$^+$ cytotoxic Tc cells. These parameters are largely outside the clinician's control since these characteristics are inherent to the cancer and the patient themselves.

The other significant network of interactions identified by sensitivity analysis were those between CD4$^+$ Th1 and Th2 helper cells [44]. The pre-treatment fraction of CD4$^+$ Th1 helper cells and CD4$^+$ Th2 helper cells as well as their dominant cytokines, IL-12 and IL-6 respectively, were identified as potential biomarkers of positive response to anti-PD-1 immunotherapy. This is a more useful result because these factors may be responsive to immunotherapy since these cells and cytokines have been studied and modified in other contexts, e.g. autoimmune diseases [45].

In each of the chapters, we investigate heterogeneity at a different level: cellular heterogeneity, variability in protein expression, and variability in immune system response. We also consider the effect of the microenvironment on cellular dynamics. By developing an *in silico* model to describe the biological phenomena, we can identify the underlying mechanisms at work and provide potential biomarkers and potential improvements that could be tested further.

References

[1] Graham Carpenter and Stanley Cohen. Epidermal growth factor. *Journal of Biological Chemistry*, 265(14):7709–7712, 1990.

[2] Sreenath V Sharma, Daphne W Bell, Jeffrey Settleman, and Daniel A Haber. Epidermal growth factor receptor mutations in lung cancer. *Nature Reviews Cancer*, 7(3):169, 2007.

[3] Douglas Hanahan and Robert A Weinberg. Hallmarks of cancer: the next generation. *cell*, 144(5):646–674, 2011.

[4] AB Miller, BFAU Hoogstraten, MFAU Staquet, and A Winkler. Reporting results of cancer treatment. *cancer*, 47(1):207–214, 1981.

[5] P Lissoni, F Brivio, L Fumagalli, G Messina, S Meregalli, G Porro, F Rovelli, L Vigore, E Tisi, and G D'AMICO. Effects of the conventional antitumor therapies surgery, chemotherapy, radiotherapy and immunotherapy on regulatory t lymphocytes in cancer patients. *Anticancer research*, 29(5):1847–1852, 2009.

[6] Yasumasa Kato, Shigeyuki Ozawa, Chihiro Miyamoto, Yojiro Maehata, Atsuko Suzuki, Toyonobu Maeda, and Yuh Baba. Acidic extracellular microenvironment and cancer. *Cancer cell international*, 13(1):89, 2013.

[7] John M Heddleston, Zhizhong Li, Roger E McLendon, Anita B Hjelmeland, and Jeremy N Rich. The hypoxic microenvironment maintains glioblastoma stem cells and promotes reprogramming towards a cancer stem cell phenotype. *Cell cycle*, 8(20):3274–3284, 2009.

[8] Nemanja D Marjanovic, Robert A Weinberg, and Christine L Chaffer. Cell plasticity and heterogeneity in cancer. *Clinical chemistry*, 59(1):168–179, 2013.

[9] Malcolm Rowland and Thomas N Tozer. *Clinical pharmacokinetics: concepts and applications*, volume 148. Williams & Wilkins Baltimore, 1995.

[10] Dmitry I Gabrilovich, Jadranco Corak, Ilja F Ciernik, Denise Kavanaugh, and David P Carbone. Decreased antigen presentation by dendritic cells in patients with breast cancer. *Clinical Cancer Research*, 3(3):483–490, 1997.

[11] John Paul Ridge, Francesca Di Rosa, and Polly Matzinger. A conditioned dendritic cell can be a temporal bridge between a cd4+ t-helper and a t-killer cell. *Nature*, 393(6684):474, 1998.

[12] Peter C Nowell. The clonal evolution of tumor cell populations. *Science*, 194(4260):23–28, 1976.

[13] Tannishtha Reya, Sean J Morrison, Michael F Clarke, and Irving L Weissman. Stem cells, cancer, and cancer stem cells. *nature*, 414(6859):105, 2001.

[14] Sascha Seidel, Boyan K Garvalov, Valtteri Wirta, Louise von Stechow, Anne Schänzer, Konstantinos Meletis, Marietta Wolter, Daniel Sommerlad, Anne-Theres Henze, Monica Nister, et al. A hypoxic niche regulates glioblastoma stem cells through hypoxia inducible factor 2α. *Brain*, 133(4):983–995, 2010.

[15] Brenton Thomas Tan, Christopher Yongchul Park, Laurie Elizabeth Ailles, and Irving L Weissman. The cancer stem cell hypothesis: a work in progress. *Laboratory investigation*, 86(12):1203, 2006.

[16] Gentao Liu, Xiangpeng Yuan, Zhaohui Zeng, Patrizia Tunici, Hiushan Ng, Iman R Abdulkadir, Lizhi Lu, Dwain Irvin, Keith L Black, and S Yu John. Analysis of gene expression and chemoresistance of cd133+ cancer stem cells in glioblastoma. *Molecular cancer*, 5(1):1, 2006.

[17] Jane E Visvader and Geoffrey J Lindeman. Cancer stem cells in solid tumours: accumulating evidence and unresolved questions. *Nature reviews cancer*, 8(10):755, 2008.

[18] Chris Folkins, Yuval Shaked, Shan Man, Terence Tang, Christina R Lee, Zhenping Zhu, Robert M Hoffman, and Robert S Kerbel. Glioma tumor stem-like cells promote tumor angiogenesis and vasculogenesis via vascular endothelial growth factor and stromal-derived factor 1. *Cancer research*, 69(18):7243–7251, 2009.

[19] Sheila K Singh, Cynthia Hawkins, Ian D Clarke, Jeremy A Squire, Jane Bayani, Takuichiro Hide, R Mark Henkelman, Michael D Cusimano, and Peter B Dirks. Identification of human brain tumour initiating cells. *nature*, 432(7015):396, 2004.

[20] Dominique Bonnet and John E Dick. Human acute myeloid leukemia is organized as a hierarchy that originates from a primitive hematopoietic cell. *Nature medicine*, 3(7):730, 1997.

[21] Muhammad Al-Hajj, Max S Wicha, Adalberto Benito-Hernandez, Sean J Morrison, and Michael F Clarke. Prospective identification of tumorigenic breast cancer cells. *Proceedings of the National Academy of Sciences*, 100(7):3983–3988, 2003.

[22] Sheila K Singh, Ian D Clarke, Takuichiro Hide, and Peter B Dirks. Cancer stem cells in nervous system tumors. *Oncogene*, 23(43):7267, 2004.

[23] Mariko Shimokawa, Yuki Ohta, Shingo Nishikori, Mami Matano, Ai Takano, Masayuki Fujii, Shoichi Date, Shinya Sugimoto, Takanori Kanai, and Toshiro Sato. Visualization and targeting of lgr5+ human colon cancer stem cells. *Nature*, 545(7653):187, 2017.

[24] Raghu Kalluri and Robert A Weinberg. The basics of epithelial-mesenchymal transition. *The Journal of clinical investigation*, 119(6):1420–1428, 2009.

[25] Sendurai A Mani, Wenjun Guo, Mai-Jing Liao, Elinor Ng Eaton, Ayyakkannu Ayyanan, Alicia Y Zhou, Mary Brooks, Ferenc Reinhard, Cheng Cheng Zhang, Michail Shipitsin, et al. The epithelial-mesenchymal transition generates cells with properties of stem cells. *Cell*, 133(4):704–715, 2008.

[26] Dongya Jia, Mohit Kumar Jolly, Satyendra C Tripathi, Petra Den Hollander, Bin Huang, Mingyang Lu, Muge Celiktas, Esmeralda Ramirez-Peña, Eshel Ben-Jacob, José N Onuchic, et al. Distinguishing mechanisms underlying emt tristability. *Cancer convergence*, 1(1):2, 2017.

[27] Corbin E Meacham and Sean J Morrison. Tumour heterogeneity and cancer cell plasticity. *Nature*, 501(7467):328, 2013.

[28] Brian Keith and M Celeste Simon. Hypoxia-inducible factors, stem cells, and cancer. *Cell*, 129(3):465–472, 2007.

[29] Zhizhong Li, Shideng Bao, Qiulian Wu, Hui Wang, Christine Eyler, Sith Sathornsumetee, Qing Shi, Yiting Cao, Justin Lathia, Roger E McLendon, et al. Hypoxia-inducible factors regulate tumorigenic capacity of glioma stem cells. *Cancer cell*, 15(6):501–513, 2009.

[30] Shideng Bao, Qiulian Wu, Sith Sathornsumetee, Yueling Hao, Zhizhong Li, Anita B Hjelmeland, Qing Shi, Roger E McLendon, Darell D Bigner, and Jeremy N Rich. Stem cell–like glioma cells promote tumor angiogenesis through vascular endothelial growth factor. *Cancer research*, 66(16):7843–7848, 2006.

[31] Richard J Gilbertson and Jeremy N Rich. Making a tumour's bed: glioblastoma stem cells and the vascular niche. *Nature Reviews Cancer*, 7(10):733–736, 2007.

[32] Carl-Henrik Heldin, Kristofer Rubin, Kristian Pietras, and Arne Östman. High interstitial fluid pressurean obstacle in cancer therapy. *Nature Reviews Cancer*, 4(10):806, 2004.

[33] C Turner and M Kohandel. Investigating the link between epithelial–mesenchymal transition and the cancer stem cell phenotype: a mathematical approach. *Journal of theoretical biology*, 265(3):329–335, 2010.

[34] Seyed Ali Madani Tonekaboni, Andrew Dhawan, and Mohammad Kohandel. Mathematical modelling of plasticity and phenotype switching in cancer cell populations. *Mathematical biosciences*, 283:30–37, 2017.

[35] Piyush B Gupta, Christine M Fillmore, Guozhi Jiang, Sagi D Shapira, Kai Tao, Charlotte Kuperwasser, and Eric S Lander. Stochastic state transitions give rise to phenotypic equilibrium in populations of cancer cells. *Cell*, 146(4):633–644, 2011.

[36] Le Zhang, Zhihui Wang, Jonathan A Sagotsky, and Thomas S Deisboeck. Multi-scale agent-based cancer modeling. *Journal of mathematical biology*, 58(4-5):545–559, 2009.

[37] Jan Poleszczuk and Heiko Enderling. A high-performance cellular automaton model of tumor growth with dynamically growing domains. *Applied mathematics*, 5(1):144, 2014.

[38] Brian P Ingalls. *Mathematical modeling in systems biology: an introduction.* MIT press, 2013.

[39] Maksat Ashyraliyev, Yves Fomekong-Nanfack, Jaap A Kaandorp, and Joke G Blom. Systems biology: parameter estimation for biochemical models. *The FEBS journal*, 276(4):886–902, 2009.

[40] Andrea Saltelli, Marco Ratto, Terry Andres, Francesca Campolongo, Jessica Cariboni, Debora Gatelli, Michaela Saisana, and Stefano Tarantola. *Global sensitivity analysis: the primer*. John Wiley & Sons, 2008.

[41] Arvind Varma, Massimo Morbidelli, and Hua Wu. *Parametric sensitivity in chemical systems*. Cambridge University Press, 2005.

[42] Moriah Pellowe, Ting Luo, and Mohammad Kohandel. An agent-based framework of tumour heterogeneity. *Dynamics of Continuous, Discrete, and Impulsive Systems*, 25:277–292, 2018.

[43] Mario Sznol and Lieping Chen. Antagonist antibodies to pd-1 and b7-h1 (pd-l1) in the treatment of advanced human cancer, 2013.

[44] Sergio Romagnani. The th1/th2 paradigm. *Immunology today*, 18(6):263–266, 1997.

[45] Vijay K Kuchroo, Mercy Prabhu Das, Julia A Brown, Ann M Ranger, Scott S Zamvil, Raymond A Sobel, Howard L Weiner, Nasrin Nabavi, and Laurie H Glimcher. B7-1 and b7-2 costimulatory molecules activate differentially the th1/th2 developmental pathways: application to autoimmune disease therapy. *Cell*, 80(5):707–718, 1995.

[46] Michael D Abràmoff, Paulo J Magalhães, and Sunanda J Ram. Image processing with imagej. *Biophotonics international*, 11(7):36–42, 2004.

[47] Jan Poleszczuk, Paul Macklin, and Heiko Enderling. Agent-based modeling of cancer stem cell driven solid tumor growth. In *Stem Cell Heterogeneity*, pages 335–346. Springer, 2016.

[48] Robert L Sutherland, Rosemary E Hall, and Ian W Taylor. Cell proliferation kinetics of mcf-7 human mammary carcinoma cells in culture and effects of tamoxifen on exponentially growing and plateau-phase cells. *Cancer research*, 43(9):3998–4006, 1983.

[49] German collection of microorganisms and cell cultures gmbh: Details. `https://www.dsmz.de/collection/catalogue/details/culture/ACC-115`. Accessed: 2019-12-10.

[50] Ylenia Lombardo, Alexander de Giorgio, Charles R Coombes, Justin Stebbing, and Leandro Castellano. Mammosphere formation assay from human breast cancer tissues and cell lines. *JoVE (Journal of Visualized Experiments)*, page e52671, 2015.

[51] Aaron Goldman, Biswanath Majumder, Andrew Dhawan, Sudharshan Ravi, David Goldman, Mohammad Kohandel, Pradip K Majumder, and Shiladitya Sengupta. Temporally sequenced anticancer drugs overcome adaptive resistance by targeting a vulnerable chemotherapy-induced phenotypic transition. *Nature communications*, 6:6139, 2015.

[52] Michael G Ormerod and Patrick R Imrie. Flow cytometry. In *Animal Cell Culture*, pages 543–558. Springer, 1990.

[53] Setsuo Hirohashi and Yae Kanai. Cell adhesion system and human cancer morphogenesis. *Cancer science*, 94(7):575–581, 2003.

[54] Serge Gangloff, Guillaume Achaz, Stefania Francesconi, Adrien Villain, Samia Miled, Claire Denis, and Benoit Arcangioli. Quiescence unveils a novel mutational force in fission yeast. *eLife*, 6:e27469, 2017.

[55] Akshay Malwade, Angel Nguyen, Peivand Sadat-Mousavi, and Brian P Ingalls. Predictive modeling of a batch filter mating process. *Frontiers in microbiology*, 8:461, 2017.

[56] Jessica A Bertout, Shetal A Patel, and M Celeste Simon. The impact of o2 availability on human cancer. *Nature Reviews Cancer*, 8(12):967–975, 2008.

[57] Stanley Borowicz, Michelle Van Scoyk, Sreedevi Avasarala, Manoj Kumar Karuppusamy Rathinam, Jordi Tauler, Rama Bikkavilli, and Robert A Winn. The soft agar colony formation assay. *Journal of Visualized Experiments*, 1, 2014.

[58] Caroline A Schneider, Wayne S Rasband, and Kevin W Eliceiri. Nih image to imagej: 25 years of image analysis. *Nature methods*, 9(7):671, 2012.

[59] Carlo Riccardi and Ildo Nicoletti. Analysis of apoptosis by propidium iodide staining and flow cytometry. *Nature protocols*, 1(3):1458, 2006.

[60] Praveena Mohan and Natalya Rapoport. Doxorubicin as a molecular nanotheranostic agent: effect of doxorubicin encapsulation in micelles or nanoemulsions on the ultrasound-mediated intracellular delivery and nuclear trafficking. *Molecular pharmaceutics*, 7(6):1959–1973, 2010.

[61] Shideng Bao, Qiulian Wu, Roger E McLendon, Yueling Hao, Qing Shi, Anita B Hjelmeland, Mark W Dewhirst, Darell D Bigner, and Jeremy N Rich. Glioma stem cells promote radioresistance by preferential activation of the dna damage response. *Nature*, 444(7120):756, 2006.

[62] Andrew Dhawan, Seyed Ali Madani Tonekaboni, Joseph H Taube, Stephen Hu, Nathalie Sphyris, Sendurai A Mani, and Mohammad Kohandel. Mathematical modelling of phenotypic plasticity and conversion to a stem-cell state under hypoxia. *Scientific reports*, 6:18074, 2016.

[63] Docetaxel — c43h53no14 - pubchem. `https://pubchem.ncbi.nlm.nih.gov/compound/Docetaxel`. Accessed: 2019-12-10.

[64] Muhammad Farhan Sohail, Mubashar Rehman, Hafiz Shoaib Sarwar, Sara Naveed, Omer Salman, Nadeem Irfan Bukhari, Irshad Hussain, Thomas J Webster, and Gul Shahnaz. Advancements in the oral delivery of docetaxel: Challenges, current state-of-the-art and future trends. *International journal of nanomedicine*, 13:3145, 2018.

[65] Wan-Jiun Chen, Chao-Chi Ho, Yih-Leong Chang, Hsuan-Yu Chen, Chih-An Lin, Thai-Yen Ling, Sung-Liang Yu, Shin-Sheng Yuan, Yu-Ju Louisa Chen, Chien-Yu Lin, et al. Cancer-associated fibroblasts regulate the plasticity of lung cancer stemness via paracrine signalling. *Nature communications*, 5:3472, 2014.

[66] M Kohandel, M Kardar, M Milosevic, and S Sivaloganathan. Dynamics of tumor growth and combination of anti-angiogenic and cytotoxic therapies. *Physics in medicine and biology*, 52(13):3665, 2007.

[67] Anna Rodina, Tai Wang, Pengrong Yan, Erica DaGama Gomes, Mark PS Dunphy, Nagavarakishore Pillarsetty, John Koren, John F Gerecitano, Tony Taldone, Hongliang Zong, et al. The epichaperome is an integrated chaperome network that facilitates tumour survival. *Nature*, 538(7625):397, 2016.

[68] Fei Dou, Liu-Di YUAN, and Jing-Jing ZHU. Heat shock protein 90 indirectly regulates erk activity by affecting raf protein metabolism. *Acta biochimica et biophysica Sinica*, 37(7):501–505, 2005.

[69] Paul Workman and Marissa V Powers. Chaperoning cell death: a critical dual role for hsp90 in small-cell lung cancer. *Nature chemical biology*, 3(8):455, 2007.

[70] Anna Rodina, Maria Vilenchik, Kamalika Moulick, Julia Aguirre, Joungnam Kim, Anne Chiang, Julie Litz, Cristina C Clement, Yanlong Kang, Yuhong She, et al.

Selective compounds define hsp90 as a major inhibitor of apoptosis in small-cell lung cancer. *Nature chemical biology*, 3(8):498, 2007.

[71] Robert Roskoski Jr. Src kinase regulation by phosphorylation and dephosphorylation. *Biochemical and biophysical research communications*, 331(1):1–14, 2005.

[72] Louis J Lombardo, Francis Y Lee, Ping Chen, Derek Norris, Joel C Barrish, Kamelia Behnia, Stephen Castaneda, Lyndon AM Cornelius, Jagabandhu Das, Arthur M Doweyko, et al. Discovery of n-(2-chloro-6-methyl-phenyl)-2-(6-(4-(2-hydroxyethyl)-piperazin-1-yl)-2-methylpyrimidin-4-ylamino) thiazole-5-carboxamide (bms-354825), a dual src/abl kinase inhibitor with potent antitumor activity in preclinical assays. *Journal of medicinal chemistry*, 47(27):6658–6661, 2004.

[73] Adly Yacoub, Song Iy Han, Ruben Caron, Donna Gilfor, Susan L Mooberry, Steven Grant, and Paul Dent. Sequence dependent exposure of mammary carcinoma cells to taxotere® and the mek1/2 inhibitor u0126 causes enhanced cell killing in vitro. *Cancer biology & therapy*, 2(6):670–676, 2003.

[74] Earl Prinsloo, Adam H Kramer, Adrienne L Edkins, and Gregory L Blatch. Stat3 interacts directly with hsp90. *IUBMB life*, 64(3):266–273, 2012.

[75] Qinghua Wu, Xu Wang, Dan Wan, Juan Li, and Zonghui Yuan. Crosstalk of jnk1-stat3 is critical for raw264. 7 cell survival. *Cellular signalling*, 26(12):2951–2960, 2014.

[76] Han C Dan, Aaron Ebbs, Manolis Pasparakis, Terry Van Dyke, Daniela S Basseres, and Albert S Baldwin. Akt-dependent activation of mtorc1 complex involves phosphorylation of mtor (mammalian target of rapamycin) by iκb kinase α (ikkα). *Journal of Biological Chemistry*, 289(36):25227–25240, 2014.

[77] Cheng-Wei Wu and Kenneth B Storey. Regulation of the mtor signaling network in hibernating thirteen-lined ground squirrels. *Journal of Experimental Biology*, 215(10):1720–1727, 2012.

[78] Michelle C Mendoza, E Emrah Er, and John Blenis. The ras-erk and pi3k-mtor pathways: cross-talk and compensation. *Trends in biochemical sciences*, 36(6):320–328, 2011.

[79] Yang Xu and Susan Lindquist. Heat-shock protein hsp90 governs the activity of pp60v-src kinase. *Proceedings of the National Academy of Sciences*, 90(15):7074–7078, 1993.

[80] Richard A Klinghoffer, Christoph Sachsenmaier, Jonathan A Cooper, and Philippe Soriano. Src family kinases are required for integrin but not pdgfr signal transduction. *The EMBO journal*, 18(9):2459–2471, 1999.

[81] Prahlad T Ram and Ravi Iyengar. G protein coupled receptor signaling through the src and stat3 pathway: role in proliferation and transformation. *Oncogene*, 20(13):1601, 2001.

[82] Xinmin Cao, Agnes Tay, Graeme R Guy, and YH Tan. Activation and association of stat3 with src in v-src-transformed cell lines. *Molecular and cellular biology*, 16(4):1595–1603, 1996.

[83] Sandeep Singh, Jose Trevino, Namrata Bora-Singhal, Domenico Coppola, Eric Haura, Soner Altiok, and Srikumar P Chellappan. Egfr/src/akt signaling modulates sox2 expression and self-renewal of stem-like side-population cells in non-small cell lung cancer. *Molecular cancer*, 11(1):73, 2012.

[84] Jennifer Van Grol, Cecilia Subauste, Rosa M Andrade, Koh Fujinaga, Julie Nelson, and Carlos S Subauste. Hiv-1 inhibits autophagy in bystander macrophage/monocytic cells through src-akt and stat3. *PloS one*, 5(7):e11733, 2010.

[85] Kai Wu, Qingshan Chang, Yongju Lu, Ping Qiu, Bailing Chen, Chitra Thakur, Jiaying Sun, Lingzhi Li, Anjaneyulu Kowluru, and Fei Chen. Gefitinib resistance resulted from stat3-mediated akt activation in lung cancer cells. *Oncotarget*, 4(12):2430, 2013.

[86] Amere Subbarao Sreedhar, Éva Kalmár, Péter Csermely, and Yu-Fei Shen. Hsp90 isoforms: functions, expression and clinical importance. *FEBS letters*, 562(1-3):11–15, 2004.

[87] Carole J Proctor and Ian AJ Lorimer. Modelling the role of the hsp70/hsp90 system in the maintenance of protein homeostasis. *PloS one*, 6(7):e22038, 2011.

[88] Carole Peyssonnaux and Alain Eychène. The raf/mek/erk pathway: new concepts of activation. *Biology of the Cell*, 93(1-2):53–62, 2001.

[89] Juan Ángel Fresno Vara, Enrique Casado, Javier de Castro, Paloma Cejas, Cristóbal Belda-Iniesta, and Manuel González-Barón. Pi3k/akt signalling pathway and cancer. *Cancer treatment reviews*, 30(2):193–204, 2004.

[90] Michael J Lee, S Ye Albert, Alexandra K Gardino, Anne Margriet Heijink, Peter K Sorger, Gavin MacBeath, and Michael B Yaffe. Sequential application of anticancer

drugs enhances cell death by rewiring apoptotic signaling networks. *Cell*, 149(4):780–794, 2012.

[91] Alejandra Tomas, Clare E Futter, and Emily R Eden. Egf receptor trafficking: consequences for signaling and cancer. *Trends in cell biology*, 24(1):26–34, 2014.

[92] Peter J Delves and Ivan M Roitt. The immune system. *New England journal of medicine*, 343(1):37–49, 2000.

[93] Dario AA Vignali, Lauren W Collison, and Creg J Workman. How regulatory t cells work. *Nature Reviews Immunology*, 8(7):523, 2008.

[94] Joseph A Trapani and Mark J Smyth. Functional significance of the perforin/granzyme cell death pathway. *Nature Reviews Immunology*, 2(10):735, 2002.

[95] Sean Diehl and Mercedes Rincón. The two faces of il-6 on th1/th2 differentiation. *Molecular immunology*, 39(9):531–536, 2002.

[96] Gordon J Freeman, E John Wherry, Rafi Ahmed, and Arlene H Sharpe. Reinvigorating exhausted hiv-specific t cells via pd-1–pd-1 ligand blockade. *Journal of Experimental Medicine*, 203(10):2223–2227, 2006.

[97] Andrew Yates, Claudia Bergmann, J Leo Van Hemmen, Jaroslav Stark, and Robin Callard. Cytokine-modulated regulation of helper t cell populations. *Journal of theoretical biology*, 206(4):539–560, 2000.

[98] Mercedes Rincón, Juan Anguita, Tetsuo Nakamura, Erol Fikrig, and Richard A Flavell. Interleukin (il)-6 directs the differentiation of il-4–producing cd4+ t cells. *Journal of Experimental Medicine*, 185(3):461–470, 1997.

[99] Thomas F Gajewski and Frank W Fitch. Anti-proliferative effect of ifn-gamma in immune regulation. i. ifn-gamma inhibits the proliferation of th2 but not th1 murine helper t lymphocyte clones. *The Journal of Immunology*, 140(12):4245–4252, 1988.

[100] Caroline Robert, Jacob Schachter, Georgina V Long, Ana Arance, Jean Jacques Grob, Laurent Mortier, Adil Daud, Matteo S Carlino, Catriona McNeil, Michal Lotem, et al. Pembrolizumab versus ipilimumab in advanced melanoma. *New England Journal of Medicine*, 372(26):2521–2532, 2015.

[101] Taku Okazaki and Tasuku Honjo. The pd-1–pd-l pathway in immunological tolerance. *Trends in immunology*, 27(4):195–201, 2006.

[102] Michael A Fishman and Alan S Perelson. Th1/th2 differentiation and cross-regulation. *Bulletin of mathematical biology*, 61(3):403–436, 1999.

[103] Steven E Macatonia, Nancy A Hosken, Mark Litton, Paulo Vieira, Chyi-Song Hsieh, Janice A Culpepper, Maria Wysocka, Giorgio Trinchieri, Kenneth M Murphy, and Anne O'Garra. Dendritic cells produce il-12 and direct the development of th1 cells from naive cd4+ t cells. *The Journal of Immunology*, 154(10):5071–5079, 1995.

[104] Joel Fleury Djoba Siawaya, Teri Roberts, Chantal Babb, Gillian Black, Hawa Jande Golakai, Kim Stanley, Nchinya Bennedict Bapela, Eileen Hoal, Shreemanta Parida, Paul Van Helden, et al. An evaluation of commercial fluorescent bead-based luminex cytokine assays. *PloS one*, 3(7):e2535, 2008.

[105] Shimon Sakaguchi. Regulatory t cells: key controllers of immunologic self-tolerance. *Cell*, 101(5):455–458, 2000.

[106] Kwang-Hyun Cho, Sung-Young Shin, Walter Kolch, and Olaf Wolkenhauer. Experimental design in systems biology, based on parameter sensitivity analysis using a monte carlo method: A case study for the tnfα-mediated nf-κ b signal transduction pathway. *Simulation*, 79(12):726–739, 2003.

[107] Bruce Alberts, Alexander Johnson, Julian Lewis, Martin Raff, Keith Roberts, and Peter Walter. Lymphocytes and the cellular basis of adaptive immunity. In *Molecular Biology of the Cell. 4th edition*. Garland Science, 2002.

[108] Hiroyuki Takaba and Hiroshi Takayanagi. The mechanisms of t cell selection in the thymus. *Trends in immunology*, 38(11):805–816, 2017.

[109] Francesca Di Rosa and Reinhard Pabst. The bone marrow: a nest for migratory memory t cells. *Trends in immunology*, 26(7):360–366, 2005.

APPENDICES

Appendix A

Additional flow cytometry data

The following images show flow cytometry results for two other cell lines studied in the Mathematical Medicine Laboratory: MDA-MB-231 (shown in Figure A.1) and SKBR3 (shown in Figure A.2).

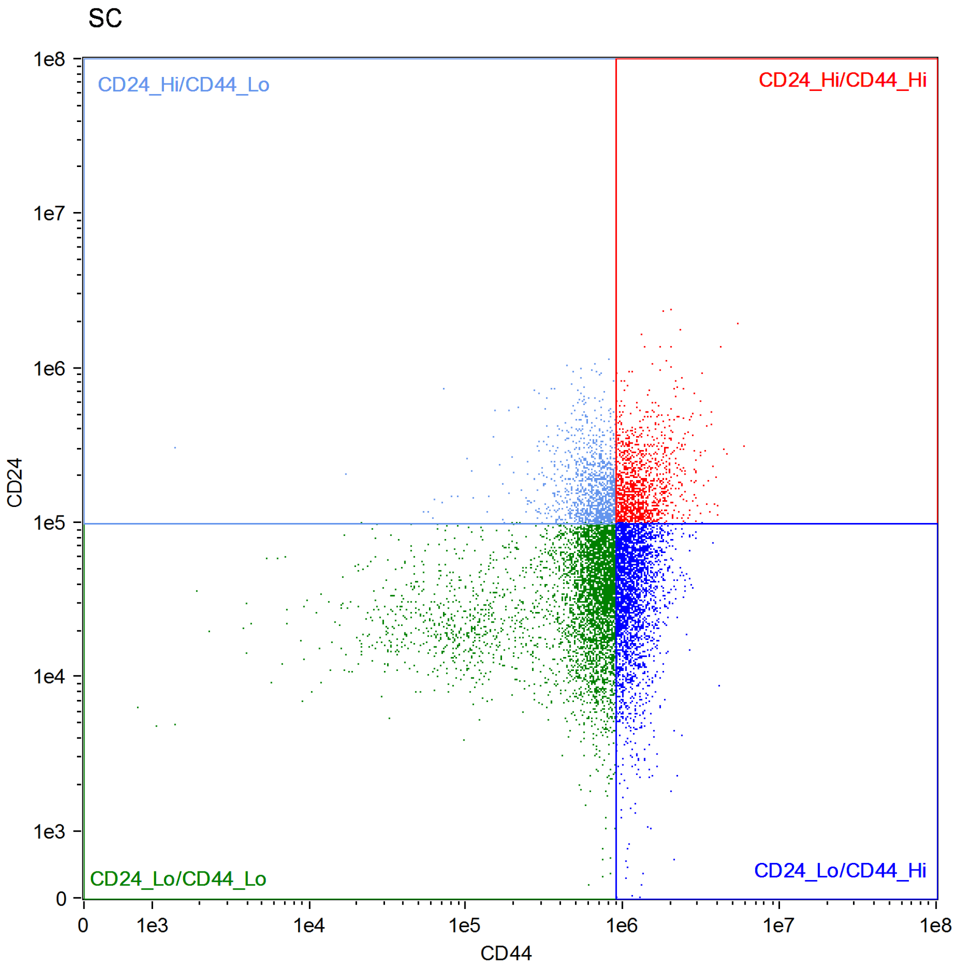

CD44, CD24

Population	Count	%Gated
SC	9945	100
CD24_Lo/CD44_Lo & SC	4606	46.3
CD24_Hi/CD44_Lo & SC	1235	12.4
CD24_Hi/CD44_Hi & SC	1252	12.6
CD24_Lo/CD44_Hi & SC	2809	28.2

Figure A.1: Flow cytometry results for breast cancer cell line MDA-MB-231. The biomarkers CD24 (y-axis) and CD44 (x-axis) were used to identify the different cell subpopulations.

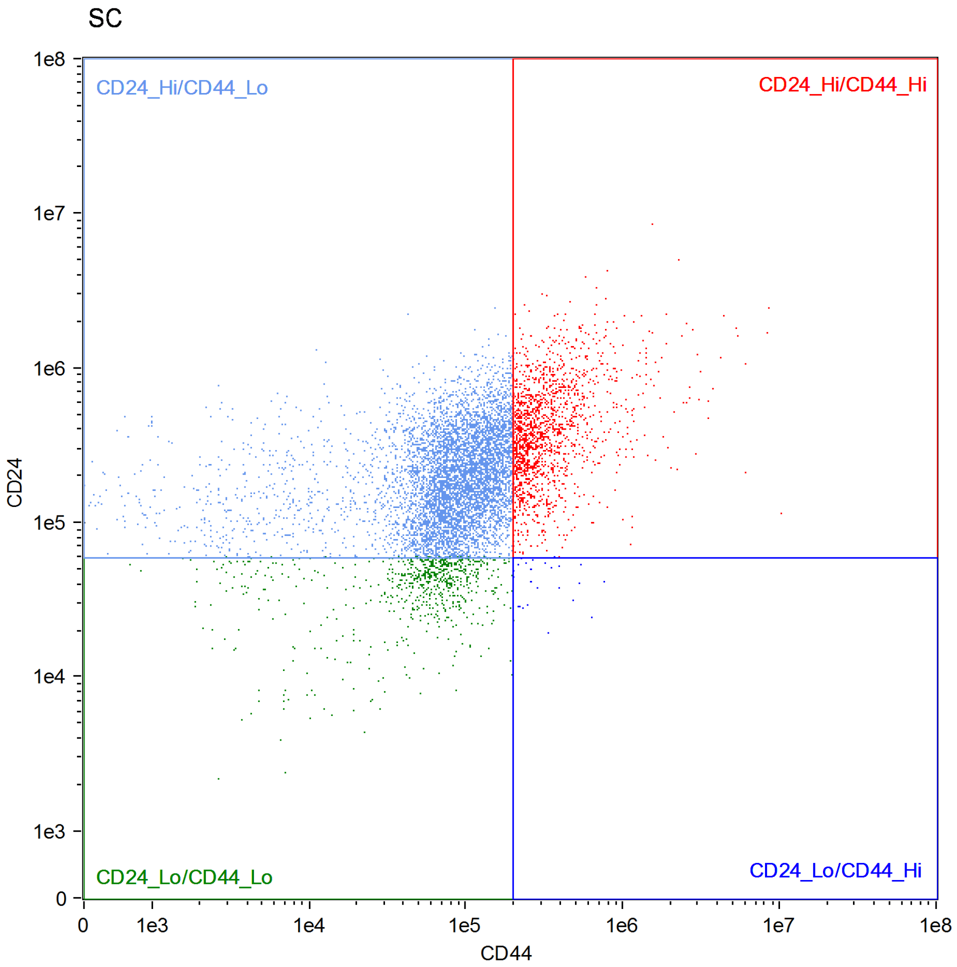

CD44, CD24

Population	Count	%Gated
SC	8430	100
CD24_Lo/CD44_Lo & SC	724	8.59
CD24_Hi/CD44_Lo & SC	5994	71.1
CD24_Hi/CD44_Hi & SC	1579	18.7
CD24_Lo/CD44_Hi & SC	24	0.28

Figure A.2: Flow cytometry results for breast cancer cell line SKBR3. The biomarkers CD24 (y-axis) and CD44 (x-axis) were used to identify the different cell subpopulations.

Glossary

AGF angiogenic growth factor 10

AMS average mammosphere size 26

angiogenesis The physiological process through which new blood vessels form from pre-existing vessels 2, 45

antibody A protein produced mainly by plasma cells that is used by the immune system to neutralize pathogens such as pathogenic bacteria and viruses 4, 89

antigen A toxin or other foreign substance which induces an immune response in the body, especially the production of antibodies 4, 88

apoptosis The death of cells which occurs as a normal and controlled part of an organism's growth or development 2, 46, 64, 88

ATCC American Type Culture Collection 26

AUC area under concentration 76

autocrine A form of cell signaling in which a cell secretes a hormone or chemical messenger (called the autocrine agent) that binds to autocrine receptors on that same cell, leading to changes in the cell 89

BCS biopharmaceutical classification system 60

biomarker A measurable substance in an organism whose presence is indicative of some phenomenon such as disease, infection, or environmental exposure 11, 26, 47, 87, 111

CA cellular automata 11

cancer stem cell Cancer cells that possess characteristics similar to normal stem cells, in particular, tumour-initiating potential 1, 27, 51, 109

caspases A family of protease enzymes playing essential roles in apoptosis and in inflammation 64

cell cycle arrest A regulatory process that halts progression through the cell cycle during one of the normal phases (G1, S, G2, M) 65

chaperone protein A protein that assists the covalent folding or unfolding and the assembly or disassembly of other macromolecular structures 64

chemotherapy The use of any drug to treat a disease 2, 46, 66, 108, 110

CSC cancer stem cell 8, 27, 60

cytokine Any of several substances, such as interferon, interleukin, and growth factors, which are secreted by certain cells of the immune system and which influence other cells 24, 65, 87, 111

cytoprotection A process by which chemical compounds provide protection to cells against harmful agents 64

cytotoxicity The quality of being toxic to cells 4, 55, 65, 88, 111

differentiate To make or become different in the process of growth or development 5, 27, 61, 64, 89

DMEM Dulbecco's Modified Eagle's Medium 26

DNA deoxyribonucleic acid 2, 48

DocRad-NP docetaxel-radicicol nanoparticle 81

DOX doxorubicin hydrochloride 48

DTC drug-tolerant cancer cell v, 13, 63

EGF epidermal growth factor 2, 86

EMT epithelial-mesenchymal transition 8, 60

eradication The complete destruction or elimination of something 32

FBS fetal bovine serum 26

flow cytometry A technique used to detect and measure physical and chemical characteristics of a population of cells or particles 35, 46, 87

fluorescence The emission of light by a substance that has absorbed light or other electromagnetic radiation 11, 35, 48

hemorrhage An escape of blood from a ruptured blood vessel, especially when profuse 10

heterogeneity The quality or state of being diverse in content 1, 44, 60, 109

homeostasis The ability of an organism or environment to maintain stability in spite of perturbations or disturbances in the organism or environment 2, 64

homogeneous Consisting of parts all of the same kind 58

hypoxia Deficiency in the amount of oxygen reaching the tissues 4, 45

IFP interstitial fluid pressure 10

immunotherapy The use of natural or artificial substances to boost the immune system's response to a disease 2, 87, 111

inflammation The inflammatory response, which occurs when tissues are injured, and damaged cells release chemicals in response 2

interstitial fluid A thin layer of fluid which surrounds the body's cells 1, 60, 110

ligand A substance that forms a complex with a biomolecule to serve a biological purpose 2, 87

mammosphere A collection or colony of breast cancer cells that have reached sufficient size to be detectable by diagnostic imaging 8, 25, 46, 109

metastasis The development of secondary malignant growths at a distance from a primary site of cancer 2, 62, 64

MFE mammosphere formation efficiency 26

microenvironment The immediate small-scale environment of an organism 1, 44, 46, 63, 89, 110

mitotic spindle The macromolecular machine that segregates chromosomes to two daughter cells during mitosis 64

multipotency The characteristic of having the capacity to self-renew by dividing and to develop into multiple specialized cell types present in a specific tissue or organ 9

necrosis The death of most or all of the cells in an organ or tissue due to disease, injury, or failure of the blood delivery 10

NP nanoparticle 81

NSERC Natural Sciences and Engineering Research Council vi

ODE ordinary differential equation 11

oncogenic Causing development of a tumor or tumors 64

PBS phosphate buffered saline 26

PDE partial differential equation 11

phenotype The set of observable characteristics of an individual resulting from the interaction of its genotype with the environment 1, 27, 46, 64, 107, 110

phosphorylation The chemical addition of a phosphoryl group (PO_3-) to an organic molecule 65

PI propidium iodide 48

plasma membrane The membrane found in all cells that separates the interior of the cell from the outside environment 65

plasticity The adaptability of an organism to changes in its environment 8, 27, 46, 110

protein kinase An enzyme that regulates the biological activity of proteins by phosphorylation of specific amino acids with ATP as the source of phosphate, thereby inducing a conformational change from an inactive to an active form of the protein 64

radiotherapy The use of radiation to treat a disease 2

RB retinoblastoma-associated 2

secretion The process by which a substance is made and released by a living thing 4, 89

signal transduction The transmission of molecular signals from a cell's exterior to its interior 64

stochasticity The state of being a randomly determined process 8, 27, 55

susceptibility The state or fact of being likely or liable to be influenced or harmed by a particular thing 58

telomere A region of repetitive nucleotide sequences at each end of a chromosome, which protects the end of the chromosome from deterioration or from fusion with neighboring chromosomes 8

transcription factor A protein that controls the rate of transcription of genetic information from DNA to messenger RNA, by binding to a specific DNA sequence 64

vasculature The blood vessels or arrangement of blood vessels in an organ or part 10